Search for the scissors resonance in ^{182}Ta

by

Christiaan Petrus Brits

Thesis presented in partial fulfilment of the requirements for the degree of Master of Science in the Faculty of Science at Stellenbosch University

Supervisor: Dr. Mathis Wiedeking

Co-supervisor: Dr. Bonginkosi Vincent Kheswa
Prof. Paul Papka

December 2016

Declaration

By submitting this thesis electronically, I declare that the entirety of the work contained therein is my own, original work, that I am the sole author thereof (save to the extent explicitly otherwise stated), that reproduction and publication thereof by Stellenbosch University will not infringe any third party rights and that I have not previously in its entirety or in part submitted it for obtaining any qualification.

Date: ..... December 2016

Abstract

Search for the scissors resonance in ^{182}Ta

C.P. Brits

Department of Physics,
University of Stellenbosch,
Private Bag X1, Matieland 7602, South Africa.

Thesis: M.Sc. Physics

December 2016

Relatively small changes to the overall shape of the photon strength function such as the scissors or pygmy resonances can have a significant impact on reaction rates. Reaction rates are important for modeling processes that take place in astrophysical environments and nuclear reactors. Recent results indicate the existence of a significant amount of scissors resonance strength in the photon strength function for nuclei in the actinide region. In order to investigate the extent and persistence of the scissors resonance strength towards lighter nuclei, an experiment was performed utilizing the NaI(Tl) gamma-ray detector array (CACTUS) and silicon particle telescopes (SiRi) at the cyclotron laboratory at the University of Oslo. Particle-gamma coincidences from the ^{181}Ta(d,p)^{182}Ta and ^{181}Ta(d,d')^{181}Ta reactions were used to measure the nuclear level density and photon strength function of the well-deformed ^{182}Ta and ^{181}Ta systems. From these data (n,γ) cross sections were calculated with the Talys reaction code.

While there are possible bumps in the photon strength function of ^{181}Ta that may be due to the scissors resonance, it appears to be absent for ^{182}Ta. These results are discussed in the context of nuclear structure and other work done in this and other mass regions.

Uittreksel

Soektog na die skêr resonansie in ^{182}Ta

("Search for the scissors resonance in ^{182}Ta")

C.P. Brits

Departement Fisika,
Universiteit van Stellenbosch,
Privaatsak X1, Matieland 7602, Suid Afrika.

Tesis: M.Sc. Fisika

Desember 2016

Relatief klein veranderinge aan die algehele vorm van die foton krag funksie soos die skêr of dwerg resonansies kan beduidende invloed op reaksiesnelhede hê. Reaksiesnelhede is belangrik vir die modellering van prosesse wat plaasvind in astrofisiese omgewings en kern reaktors. Onlangse resultate dui daarop dat daar 'n beduidende bedrag skêr resonansie krag in die foton krag funksie vir kerne in die aktinied streek is. Ten einde die omvang en volharding van die skêr resonansie krag teenoor ligter kerne te bepaal, is 'n eksperiment uitgevoer met behulp van die NaI(Tl) gammastraal-detektor matriks (CACTUS) en silikon deeltjie teleskoop (SiRi) by die siklotron laboratorium aan die Universiteit van Oslo. Deeltjie-gamma toevallighede van die ^{181}Ta(d,p)^{182}Ta en ^{181}Ta(d,d')^{181}Ta reaksies is gebruik om die kern vlak digtheid en foton krag funksie van die goed vervormde ^{182}Ta en ^{181}Ta stelsels te bepaal. Van hierdie data is (n,γ) dwarssnitte bereken met die Talys reaksie kode.

Hoewel daar moontlike bewyse vir die skêr resonansie in die foton krag funksie van ^{181}Ta is, is dit afwesig in ^{182}Ta. Hierdie resultate word bespreek in die konteks van kernstruktuur en ander werk wat in hierdie en ander massa streke gedoen is.

Acknowledgements

I would like to acknowledge my supervisors, Dr. M. Wiedeking, Prof. P. Papka and Dr. B. V. Kheswa, my colleagues K. L. Malatji and B. Zikhali for all the time they spent helping me and the Oslo nuclear physics group for the nice beam time and time spent on shifts. I would like to thank the University of Stellenbosch for their financial support, iThemba labs for the work space they provided and finally my family; for their unwavering trust that I will always succeed.

Contents

List of Figures

List of Tables

Nomenclature

Constants

c	299 792 458 $\frac{m}{s}$
π	3.142
$\hbar$	$1.0546 \times 10^{-34} \frac{m^2 kg}{s}$

Variables

$\rho(E_x)$	level density
$\mathrm{T}(E_\gamma)$	Gamma transmission coefficient
$\mathrm{f}(E_\gamma)$	photon strength function
Γ	radiative width
σ	spin cut-off parameter
E_x	Excitation energy
E_γ	γ-ray energy
S_n	neutron separation energy
D_0	neutron resonance spacing
a	level density parameter
μ_N	nuclear magneton

Vectors and Tensors

$\overrightarrow{v}$	Physical vector

Acronyms

PSF	Photon strength function
NLD	Nuclear level density
OCL	Oslo Cyclotron Laboratory
LO	Lorentzian
SLO	Standard Lorentzian
GLO	Generalized Lorentzian
EGLO	Enhanced Generalized Lorentzian

GEDR Giant Electric Dipole Resonance
GMDR Giant Magnetic Dipole Resonance
NRF Nuclear Resonance Fluorescence

Chapter 1

Introduction

When a nucleus is excited, a particle (neutron, proton or both) moves to a higher energy level. At low energy these levels are discrete and the energy of the γ-rays emitted, when the nucleus de-excites, can be measured individually. At higher energies the level density increases exponentially and the levels begin to overlap and they form a quasi-continuum. This is illustrated in figure 1.1. The different γ-rays emitted when a highly excited nucleus de-excites from the quasi continuum cannot be resolved with the present experimental resolution. With the levels overlapping, statistical properties become the relevant concepts, in particular two important statistical quantities are: the photon strength function (PSF) and the nuclear level density (NLD). The PSF is also known as the radiative strength function and γ-ray strength function in literature. The PSF characterises the average electromagnetic properties of excited nuclei. It is related to radioactive decay and photo-absorption processes. The level density is an indication of the amount of levels per unit of excitation energy. These statistical properties are closely related to their discrete counterparts, the transition strengths and number of discrete (countable) energy levels.

The PSF and NLD are used for many physical applications:

- They are used as input parameters for the calculation of reaction cross sections in reaction codes like Talys [1].
- The PSF and NLD are used in the design phase of nuclear power reactors. Simulations of the reactor depends on the evaluated data of all the various nuclear reactions involved [2].
- The PSF and NLD also play a central role in elemental formation during stellar nucleosynthesis and it is important to know and understand the PSF for all nuclides involved. Theoretical calculations have shown that small changes to the shape of the PSF, such as a pygmy or scissors

resonance, can effect the rate of elemental formation by up to an order of magnitude [3].

- The behaviour of the PSF and NLD can be used to make statements about the structure of the nucleus.

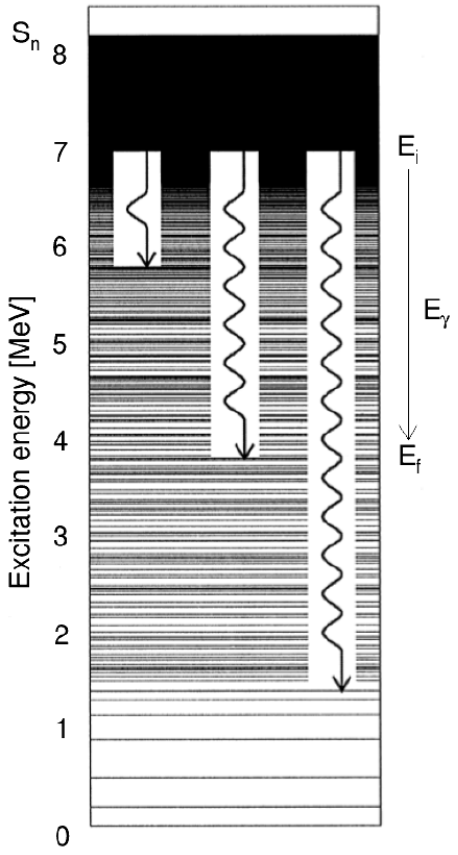

Figure 1.1: The level density as the excitation energy increases [4].

The breaking of nucleon cooper pairs or excitation modes such as the E1 pygmy resonance and the M1 scissors resonance can be observed as local deviations in the NLD and PSF, respectively.

The scissors resonance was first observed in an inelastic electron scattering experiment of ^{156}Gd [5] and it was later confirmed in ^{158}Gd as shown in figure 1.2. At a bombarding energy of 25 MeV the scissors resonance can be seen at $E_x = 3.074$ MeV for ^{156}Gd and at $E_x = 3.2$ MeV for ^{158}Gd. The scissors resonance has been observed in various nuclei using nuclear resonance fluorescence (NRF) experiments [6] and also through the Oslo method (e.g. [7]). The scissors resonance was first observed in well deformed nuclei, but it has since

been observed in vibrational, transitional and γ-soft nuclei. It has also been found that in some cases the scissors resonance of even-even nuclei have different properties to that of odd-even nuclei, which can have a large fragmented scissors strength distribution [8].

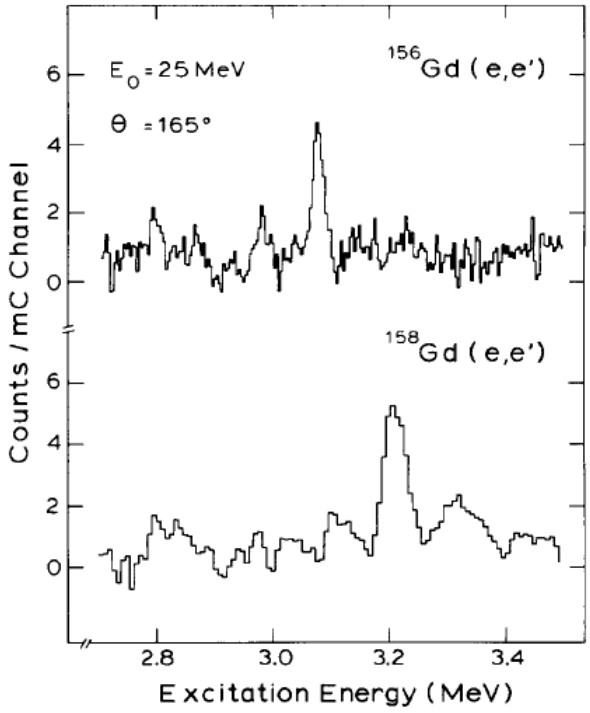

Figure 1.2: The first observed scissors resonance in the ^{156}Gd observed at E_x = 3.074 MeV compared with the scissors resonance of ^{158}Gd at E_x = 3.2 MeV, populated using (e,e') at 25 MeV [5].

Although much knowledge has been obtained about the scissors resonance over the years [9], its extent across the nuclear chart is still not well understood. In particular, the evolution of a well developed scissors resonance from one region of the nuclear chart to another, such as from the rare-earth to the actinide region has not been systematically investigated. To fully understand the interplay of the scissors resonance with other nuclear structure aspects (e.g. coupling to unpaired nucleons, dependence on nuclear shapes etc.) and its potential impact on astrophysical reaction rates, its extent and persistence have to be carefully measured.

The aim of this thesis is to investigate the scissors resonance in the well deformed ^{181}Ta and ^{182}Ta nuclei which lie in the transitional region from prolate to oblate shapes. It also lies between the rare-earth and actinide systems, both

of which exhibits large scissors resonance modes. The location of Ta in the β_2 deformation chart of nuclei is shown in figure 1.3.

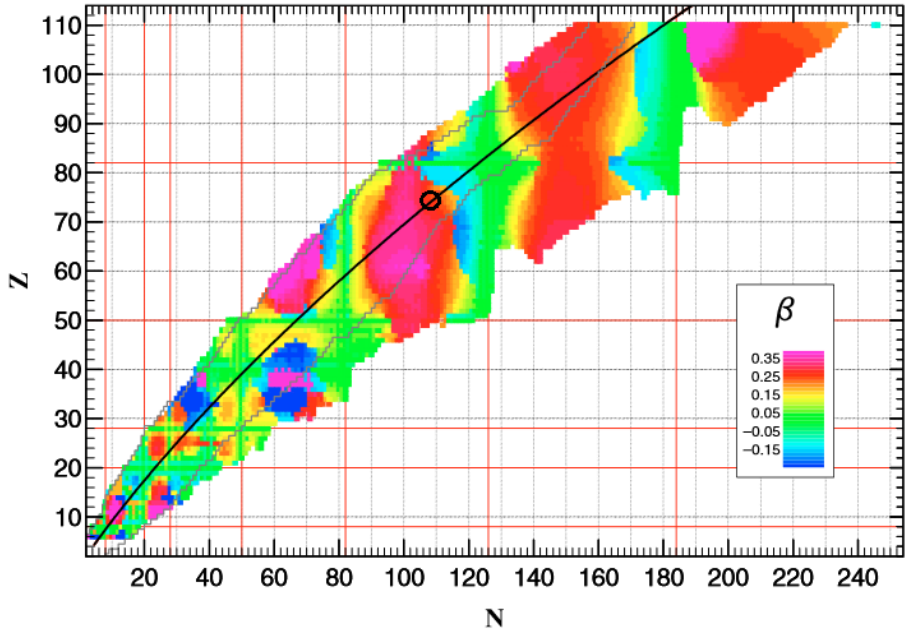

Figure 1.3: Chart of nuclei showing the Hartree-Fock-Bogoliubov calculated deformation parameters β_2 [10]. The region of Ta is shown by the black circle.

Chapter 2

Theory

2.1 Nuclear level density

The amount of available quasi-particles is the basis block that determines the nuclear level density (NLD). The density of available single-particle orbitals in the vicinity of the fermi-level is the other factor that plays a role in the NLD. It has been shown that neighboring isotopes can have 5-7 times more energy levels if one or more proton or neutron are unpaired [11]. The breaking of $J = 0$ nucleon cooper pairs creates additional states in a nucleus. The two free nucleons can be excited to available single-particle levels in the vicinity of the Fermi surface, thus increasing the NLD exponentially [12].

At low energies, excitation levels of the nucleus can be discriminated experimentally by measuring the energy of theγ-ray from gamma transitions originating from these levels. At high energies (above 2-4 MeV excitation energy, depending on nucleus mass) the levels are too dense to be discriminated. A model is then used to predict how many levels there are present at a given excitation energy, parity and spin. The method used to extract the level density will be discussed in Chapter 3. In this section a few nuclear level density models considered for this project will be presented.

The first description of NLD $\rho(E_x)$ was accomplished in 1936 by starting with an individual particle picture and using Fermi statistics to calculate $\rho(E_x)$ as [13]:

$$\rho(E_x) = \frac{1}{12}\sqrt{\frac{\pi}{a}}2^{\frac{1}{4}}E_x^{-\frac{5}{4}}\exp(\sqrt{2E_x}a) \tag{2.1}$$

where E_x is the excitation energy and a is the level-density parameter. This model predicted that the level density increases as the exponential of the square root of the energy times the level-density parameter. While this prediction

is correct to first order, the model had many limitations by not taking into account shell-effects, pairing correlations and collective phenomena.

2.1.1 Back-shifted Fermi Gas model

The model described in reference [14] includes pairing and the shell-correction energies. This model can also be used to calculate the level densities of nuclei for which no experimental information has been measured. The term "back-shifted" comes from the energy E_x being shifted by the proton, Δ_p, and neutron, Δ_n, pairing energy so that the model agrees better with experimental results. This shift turned out to be too big so it was "back-shifted" by a parameter C. The adopted level density formula at a given excitation energy E_x and angular momentum J (for both parities) is given by:

$$\rho(E_x, J) = \frac{(2J+1)\exp\left(-\frac{(J+\frac{1}{2})^2}{2\sigma^2}\right)}{2\sqrt{2\pi}\sigma^3} \frac{\sqrt{\pi}\exp\left(2\sqrt{aU}\right)}{12a^{\frac{1}{4}}U^{\frac{5}{4}}}. \tag{2.2}$$

Integrating over all possible J gives the the observable level density:

$$\rho(E_x) = \frac{\exp\left(2\sqrt{aU}\right)}{12a^{\frac{1}{4}}U^{\frac{5}{4}}\sqrt{2}\sigma}. \tag{2.3}$$

where $U = E_x - E_1$ is the back-shifted excitation energy, a is the level density parameter and σ^2 is the back-shifted spin cut-off parameter given by:

$$\sigma^2 = 0.08888A^{\frac{2}{3}}\sqrt{a(S_n - E_1)}. \tag{2.4}$$

The back-shifted parameter E_1 and level density parameter a can be obtained from reference [15] or calculated from shell corrections, S, and nuclear mass number, A, if there is no experimental information. For spherical nuclei, a can be calculated by: $\frac{a}{A} = 0.00917S + 0.142$ and for deformed nuclei the equation is $\frac{a}{A} = 0.00917S + 0.120$. These equations were obtained from first degree polynomial fits to experimental data and does not depend on deformation magnitude. The typical S value for ^{182}Ta is 6.69 and for ^{181}Ta it is 6.83, values for S can be found in reference [14].

A correction to this model was noted in reference [15] where it is shown that the spin cut-off parameter (as a function of A and E_x) can also be calculated by:

$$\sigma^2 = 0.319A^{0.675}(E_x - 0.5Pa')^{0.312} \tag{2.5}$$

where Pa' is the deuteron pairing energy.

2.1.2 Constant Temperature model

As stated in the previous section, the model used in [14] uses a constant temperature formula at energies lower than 10 MeV. This gives the level density for all angular momenta as:

$$\rho(E_x) = \frac{\exp(\frac{E_x - E_0}{T})}{T} \tag{2.6}$$

where T is the nuclear temperature and E_0 is the energy-shift parameter. Reference [15] gives these parameters as:

$$E_0 = -1.004 + 0.5Pa' \tag{2.7}$$

$$T = \frac{1}{A^{\frac{2}{3}}(0.0597 + 0.00198S')} \tag{2.8}$$

where the shifted shell correction is given by $S' = S + 0.5Pa'$. The values of the deuteron separation energy, Pa', and shell correction, S, can also be obtained from [15].

2.2 Photon strength function

The PSF $f_{XL}(E_\gamma)$ characterizes the average electromagnetic properties of excited nuclei. It is a distribution of average reduced widths for transitions of a certain multipole type XL between two different states of energies. The transition can occur either due to photo absorption processes or radiative decay. During photo absorption ($f_{XL}(E_\gamma \uparrow)$) a photon is absorbed and a transition occurs from a low energy state to a higher energy state. During radiative decay ($f_{XL}(E_\gamma \downarrow)$) a photon is emitted and a transition occurs from a high energy state to a low energy state.

The first PSF for radiative decay is introduced in [16] as:

$$f_{XL}(E_\gamma \downarrow) = \frac{< \Gamma_{\gamma l} >}{E_\gamma^{2L+1} D_l} \tag{2.9}$$

where X is the electromagnetic character, L is the multipolarity, E_γ is the γ-ray energy, D_l is the resonance spacing for l-wave resonances and $< \Gamma_{\gamma l} >$ is the average radiative width. The PSF for photo absorption is introduced in [16] as:

$$f_{XL}(E_\gamma \uparrow) = \frac{< \sigma_{XL}(E_\gamma) >}{(2L+1)(\pi\hbar c)^2 E_\gamma^{2L-1}} \tag{2.10}$$

where $< \sigma_{XL}(E_\gamma) >$ is the average photo-absorption cross section. According to Fermi's Golden rule [18] and detailed balance, $f_{XL}(E_\gamma \downarrow)$ and $f_{XL}(E_\gamma \uparrow)$

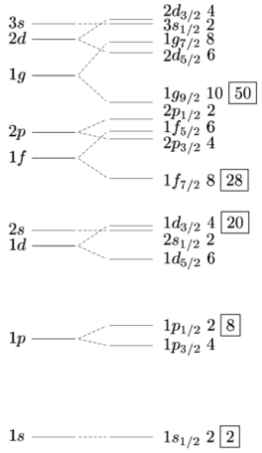

Figure 2.1: A diagram of the shell model with spin-orbit interaction [17].

correspond to each other, provided that the same states are populated. This project focuses on $f_{XL}(E_\gamma \downarrow)$ so the $\downarrow$ will be omitted for the rest of the thesis. The photon strength function can also be written in terms of the γ-ray transmission coefficient:

$$T_{XL}(E_\gamma) = 2\pi \frac{< \Gamma_{\gamma l} >}{D_l}. \tag{2.11}$$

The derivation of this equation will be explained in Chapter 3. Various models, called resonance models, are used to describe photon strength functions. They will be discussed briefly in section 2.4.

2.3 Nuclear models

The basic model to describe nuclear structure is the shell model, where the nucleons are placed within levels that form shells. Excitation and de-excitation correspond to nucleons moving up or down in levels. The unpaired nucleons, then determine the properties of the nucleus. The shell model has also been expanded to include the spin-orbit interaction to properly reproduce sub shells and thereby the magic numbers observed experimentally. The shell model with the spin-orbit interaction included is shown in figure 2.1.

The shell model with spin-orbit interaction however only works if the nuclear potential is spherical. The energy levels in a deformed potential depend on the spatial orientation of the orbit. Ω is the quantum number used to describe the projection of the total angular momentum onto the symmetry axis [18], as shown in figure 2.2. The early model that took deformation into account is the Nilsson model, an example of resulting energy levels of s-d nuclei is shown

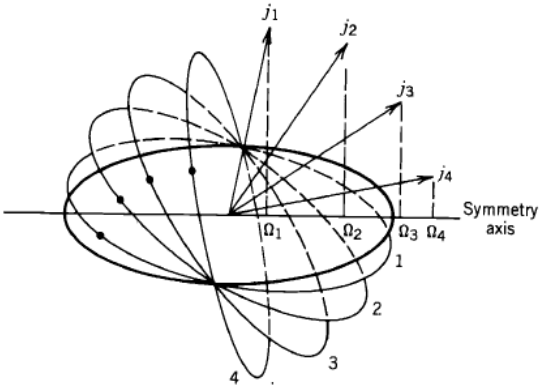

Figure 2.2: The projection of the total angular momentum on the symmetry axis forms the quantum number Ω [18].

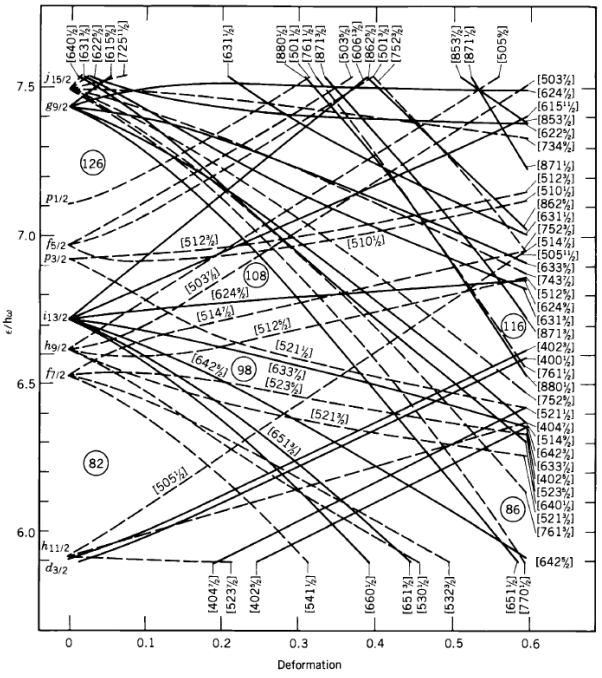

Figure 2.3: The Nilsson diagram of nuclei between the 82 and 126 shell gaps [18].

in figure 2.3.

It has also been noted that collective motion of all the nucleons give rise to collective nuclear properties. The shell model treatment of collective motion has to take into account all valence nucleons outside the core and not just the unpaired nucleons. The spin-flip transition is an example of single nucleon transitions that is used to clarify the single particle properties of the nuclear wave function. The pygmy and scissors resonances are examples of collective motion and give information on the collective properties of the nucleus [19].

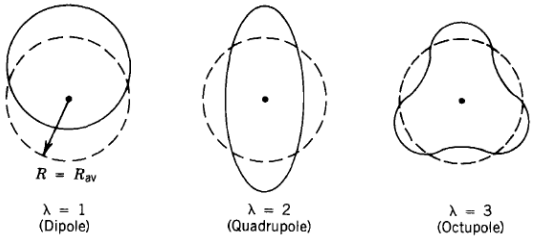

Figure 2.4: Different modes of nuclear vibrations [18].

These resonances will be explain in detail in section 2.4.

Other examples of collective motion is vibration and rotation. To envision nuclear vibration, a liquid drop vibrating at a high frequency can be considered. The liquid drop will have an average spherical shape, but its instantaneous shape will be deformed. Nuclear vibration is seen as dynamic deformations and the shape of the nucleus changes over time. Different modes of vibration is given by λ, where $\lambda = 1$ corresponds to a dipole vibration and $\lambda = 2$ corresponds to a quadrupole vibration, as shown in figure 2.4. The quantized unit of vibration energy is called a phonon. Each mode of vibration also carries a similar angular momentum value, for example in the $\lambda = 2$ mode, the phonon carries 2 units of angular momentum.

A common deformation parameter is β, which represents the eccentricity of ellipsoid deformation [18]. Static deformed nuclei with $\beta > 0$ have a prolate ellipsoid shape and nuclei with $\beta < 0$ have an oblate ellipsoid shape as shown in figure 2.5. Static deformed nuclei are commonly found in atomic mass ranges $150 < A < 190$ (rare-earth region) and $A > 220$ (actinide region). The nuclei in these mass ranges have nucleons far from filled proton and neutron shells.

Vibrations in deformed nuclei can occur along either the β or the γ axis. β vibrations correspond to a vibrating deformation parameter β while the nucleus keeps it cylindrical shape. γ vibrations on the other hand violate the cylindrical shape. This can be visualized with a rugby ball, γ vibrations correspond to the push and pull on the sides and β vibration is the push and pull on the ends of the rugby ball.

Rotations are only observable in deformed nuclei, because rotation can only take place if one axis is longer or shorter than the other. The nucleus needs an axis to rotate about. Rotational energy can be expressed by [18]:

$$E = \frac{\hbar^2}{2\Theta} I(I+1) \tag{2.12}$$

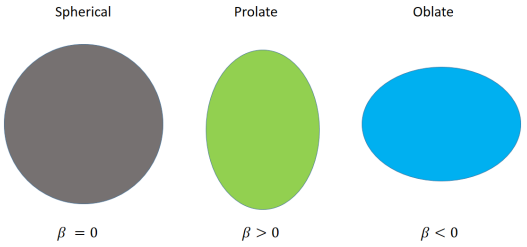

Figure 2.5: Static deformations of the nucleus: spherical (left), prolate (middle)and oblate (right).

where Θ is the moment of inertia and I is the angular momentum. By adding units of angular momentum to the energy, results in the creation of rotational bands in the nuclear excitation states. These nuclear models are used to describe nuclear structure effects and can be used to explain the origin of collective phenomena.

2.4 Resonance models

2.4.1 Giant resonances

Giant resonances are characterized using three quantum numbers: angular momentum J, spin S and isospin T. L indicates the multipole order:

- monopoles have $L = 0$
- dipoles have $L = 1$
- quadrupoles have $L = 2$
- octupoles have $L = 3$

Spin can have a value of 0 or 1. $S = 0$ refers to electric resonances and $S = 1$ refers to magnetic resonances. An electric resonance is seen as a purely spatial oscillation of the nuclear mass, while a magnetic resonance is seen as spin oscillation.

Isospin is a quantum number related to the strong interaction. Particles that are affected by the strong force equally but have different charges, such as protons and neutrons, can be treated as being in different states with isospin values related to the number of charges. There are two types of isospin: isoscalar ($T = 0$) and isovector ($T = 1$). For isocalar resonances the neutrons and protons oscillate in phase and for isovector resonances the neutrons and protons

oscillate out of phase.

The isoscalar electric monopole resonance is also known as the breathing mode, because the nucleus has purely radial oscillations, similar to the expanding and contracting of lungs. The energy of this resonance is important when calculating the nuclear compressiblity [20].

The giant electric dipole resonance (GEDR) is induced by the absorption or emission of a γ-ray. The movement of the nucleus in the GEDR is shown in Figure 2.6 and for giant magnetic dipole resonance (GMDR) in Figure 2.7.

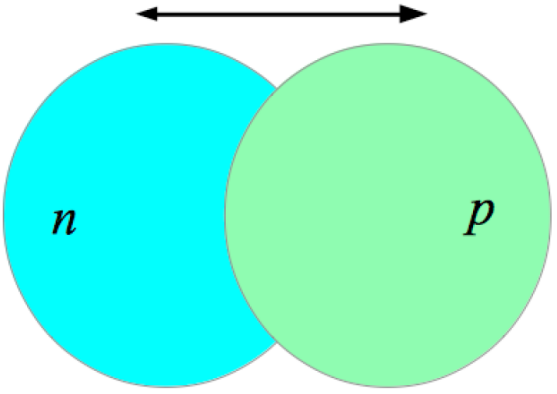

Figure 2.6: The motion of the neutron and proton distributions in the giant electric dipole resonance [21].

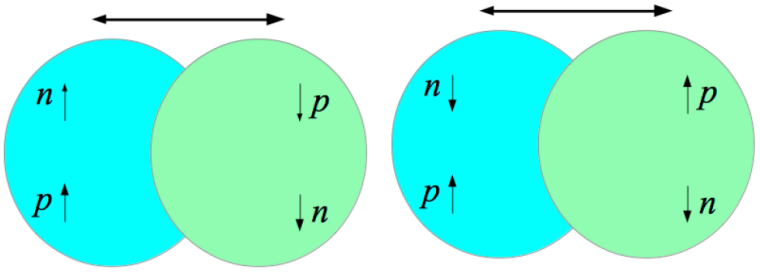

(a) Isoscalar GMDR (b) Isovector GMDR

Figure 2.7: Illustration of the motion of the neutron and proton distributions during a giant magnetic dipole resonance [21]. For isoscalar GMDR (a) the protons and neutrons oscillate in phase and for isovector GMDR (b) the protons and neutrons oscillate out of phase.

2.4.2 Pygmy resonances

The pygmy resonance can be explained on a macroscopic level by the proton and neutron core oscillating against the neutron skin, as illustrated in figure 2.8. On a microscopic level there is still some debate, with some (e.g. [22]) interpreting the pygmy resonance as a collective excitation, where the characteristic calculated levels are coherent superpositions of particle-hole or quasiparticle-hole states. Others (e.g. [23]) characterize the pygmy resonance as a collective state with two-quasiparticle states. It has been accepted, however, that the pygmy resonance decays by emitting E1 type γ-rays [24].

The strength of the pygmy resonance is usually a small part of the energy weighted sum rule, e.g. for ^{208}Pb the pygmy resonance strength takes $3-6\%$ of the sum rule energy [25]. However the pygmy resonance has a very large effect on the radiative neutron capture cross section. For example with the inclusion of this resonance the abundance of A $\approx$ 130 elements is calculated to increase by an order of magnitude compared to a simulation where the pygmy resonance is not included [3]. There are many microscopic approaches to describe the pygmy resonance, the quasiparticle-phonon model, the generalized theory of finite Fermi systems, the QRPA plus coupling to phonons model and the relativistic quasi-particle time-blocking approximation, see [26] and references therein for information on these models.

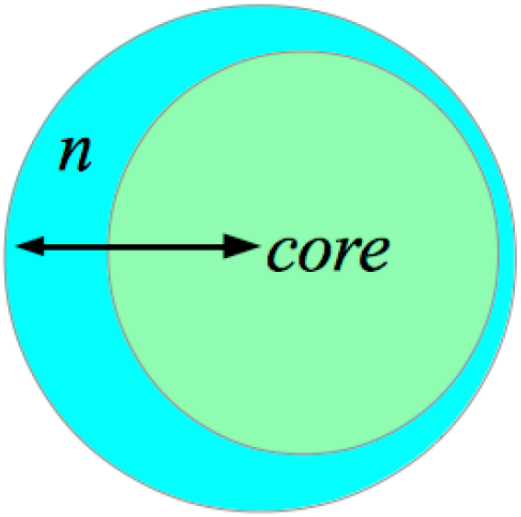

Figure 2.8: Oscillation of the neutron proton core against the neutron skin resulting in the pygmy resonance [21].

2.4.3 M1 resonance modes

Using an algebraic collective model the interacting fermion system (protons and neutrons) can be treated as bosons. This interacting boson system (IBM) has been studied in detail in references [27, 28] so only the results relevant to the current work will be discussed here. For protons and neutrons the magnetic dipole operator is [9]:

$$\hat{T}(M_1) = \sqrt{\frac{3}{4\pi}} \sum_i \{g_l(i)\hat{l}_i + g_s(i)\hat{s}_i\}\mu_N \tag{2.13}$$

where g_l and g_s are the orbital and spin factors for the protons and neutrons in a fermion system, $\hat{l}_i$ and $\hat{s}_i$ are the angular momentum and spin operators and μ_N is the nuclear magneton. $T(M1)$ can be split into an isoscalar and isovector term [9]:

$$\hat{T}(M_1) = \sqrt{\frac{3}{4\pi}}(g_J\hat{J} + g_S\hat{S})\mu_N + \hat{T}(M_1, IV) \tag{2.14}$$

where $\hat{J}$ and $\hat{S}$ is the total angular momentum and spin operators. The $\hat{J}$ part of the isoscalar term does no induce any M1 transitions and the $\hat{S}$ part contributes very little to the M1 transitions. The isovector part can be given by [9]:

$$\hat{T}(M_1, IV) = \sqrt{\frac{3}{4\pi}} \left\{ \frac{1}{2}(\hat{L}_\pi - \hat{L}_\nu) + \frac{1}{2}(g_s^\pi - g_s^\nu)(\hat{S}_\pi - \hat{S}_\nu) \right\} \mu_N \tag{2.15}$$

where g_s^π and g_s^ν are the spin boson factors and $\hat{L}$ and $\hat{S}$ are the orbital angular momentum and spin operators of the boson system respectively. The first part describes the scissors motion and the second part describes the spin-flip motion.

2.4.3.1 Deformation and pairing

The correlation between deformation and pairing is not straight forward at first. In a quadrupole deformed potential, the M1 strength between Nilsson orbitals distinguished by Ω, can be approximately expressed by [9]:

$$B(M1) = \frac{3}{4\pi}(u_1 v_2 - u_2 v_1)^2 | < \Omega_1 | g_l \hat{l}_+ + g_s \hat{s}_+ | \Omega_2 > |^2 \tag{2.16}$$

where v_i (with $u_i = 1 - v_i$) is the occupation probability of the Nilsson orbits Ω. Here the first term represents the pairing factor and the second term the

transition matrix element between the Ω orbits. The effect of deformation on the Ω orbits are shown in figure 2.9. For small deformations the pairing factor smothers the M1 strength and it vanishes for zero deformation. As the deformation increases, the Nilsson single-particle orbits originating from a single j shell-model orbit, become dispersed and the occupation probabilities change giving larger pairing factors. Assuming that the Nilsson orbitals differ linearly with the deformation (for not to big deformations), the pairing factor becomes proportional to the deformation parameter δ^2.

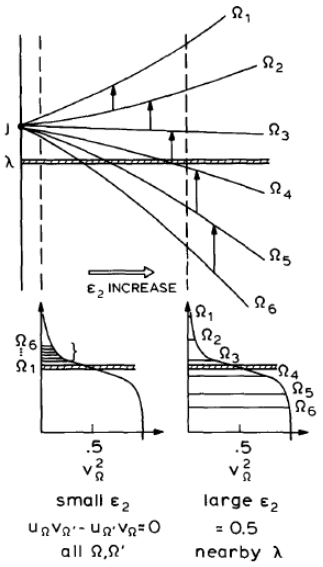

Figure 2.9: Representation of the deformation effect on the M1 scissors transitions [29].

2.4.3.2 Scissors resonance

The first evidence of a low-lying M1 mode, the scissors resonance, was reported in reference [5]. Many models have been applied since to describe and explain this resonance, the two-rotor model [30], the interactive Boson model (IBM) [31] and microscopic models [32].

The two-rotor model describes the scissors resonance as a distribution of protons and neutrons oscillating against each other like the blades of a scissor. This is illustrated in figure 2.10. The IBM describes it as the lowest 1^+ member of a group with wave functions that are not symmetrical under the exchange of proton and neutron bosons. The microscopic models try to describe the nuclear structure of the nuclei involved and the fragmentation of the mode.

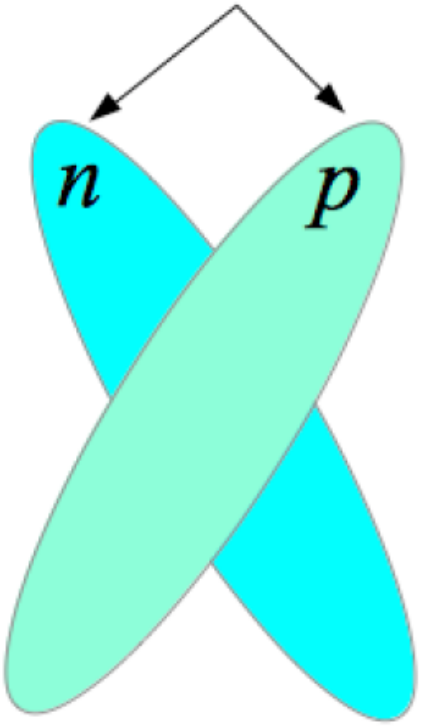

Figure 2.10: The oscillation of the neutron and proton distributions form the scissors resonance [21].

The scissors resonance is a collective excitation mode dominated by single-particle events. The scissors resonance results from transitions between magnetic substates differing by one unit of angular momentum. On a Nilsson scheme the transitions will correspond to $\Omega \pm 1$ transitions with similar spherical j components, see figure 2.11. The centroid of the scissors resonance can be found at an excitation energy of [32]:

$$E_x \simeq 66\delta A^{-1/3} MeV \tag{2.17}$$

where δ is the deformation parameter. Axially symmetric Hartree-Fock-Bogoliubov (HFB) calculations using Cogny effective nucleon-nucleon interaction can be used to calculate the axial deformation parameter β_2 [10], which is related to δ up to first order by [33]:

$$\beta_2 = \sqrt{\frac{\pi}{5}}\frac{4}{3}\delta. \tag{2.18}$$

The $B(M1)$ strength is given by a set of resonance parameters [34]:

$$B = \frac{\hbar 9c}{32\pi^2}\left(\frac{\sigma\Gamma}{\omega}\right) \tag{2.19}$$

where σ is the cross section, ω is the average centroid energy and Γ is the radiative width of the scissors resonance. A sum-rule approach can be used to calculate the scissors resonance strength and energy centroid. The linearly and inverse energy-weighted sum rules are given by [35]:

$$S_{+1} = \frac{3}{2\pi}\Theta_{rigid}\delta^2\omega_D^2\left(\frac{Z}{A}\right)^2\xi[\mu_N^2]\text{MeV} \tag{2.20}$$

$$S_{-1} = \frac{3}{16\pi}\Theta_{rigid}\left(\frac{2Z}{A}\right)^2[\mu_N^2]\text{MeV} \tag{2.21}$$

where Θ_{rigid} is the rigid moment of inertia given by [35]:

$$\Theta_{rigid} = \frac{2}{5}m_N r_0^2 A^{\frac{5}{3}}(1+0.31\delta) \tag{2.22}$$

and m_N is the mass of the nucleon and ξ is the reduction factor given by [35]:

$$\xi = \frac{\omega_Q^2}{\omega_Q^2 + 2\omega_D^2} \tag{2.23}$$

where ω_Q and ω_D are the isovector giant dipole resonance and isoscalar giant quadrupole resonance frequency [35]:

$$\omega_D \approx (31.2A^{\frac{-1}{3}} + 20.6A^{\frac{-1}{6}})(1-0.61\delta)\text{MeV} \tag{2.24}$$

$$\omega_Q \approx 64.7A^{\frac{-1}{3}}(1-0.3\delta)\text{MeV}. \tag{2.25}$$

These two sum rules can be used to calculate the energy centriod ω_{SR} and resonance strength B_{SR} [35]:

$$\omega_{SR} = \sqrt{\frac{S_{+1}}{S_{-1}}} = |\delta|\omega_D\sqrt{2\xi} \tag{2.26}$$

$$B_{SR} = \sqrt{S_{+1}S_{-1}} = \frac{3}{4\pi}(\frac{Z}{A})^2\Theta_{rigid}\omega_{SR} \tag{2.27}$$

The scissors resonance was identified in the rare-earth region and several actinides and it is believed that it can be found in all deformed nuclei [7]. The scissors resonance has also been observed in less deformed transitional nuclei:

- γ-soft nuclei ^{196}Pt [36] and ^{134}Ba [37].

- transitional osmium nuclei [38].
- vibrational tellurium isotopic nuclei [39, 40].

In the transitional nuclei, the decay properties are different from those in the well-deformed nuclei due to the loss of axial symmetry. The M1 strength distribution is greatly reduced for γ-soft nuclei for example in ^{196}Pt [36]. In odd-even nuclei the odd-particle (-hole) coupling to the 1^+ modes creates a big fragmentation in the M1 strength distribution for some nuclei, such as ^{167}Er. In some other nuclei like ^{161}Dy the M1 strength is localized, but has reduced strength. It has been pointed out in reference [8] that the scissors resonance strength for odd-even nuclei may be comparable to that in the even-even nuclei, but due to the fragmentation of the the scissors resonance, a large part of it lies below the experimental detection threshold. The findings of reference [41] supports this.

2.4.3.3 Spin-flip resonances

Neutron and proton single-particle transitions of the kind $(J = l-1/2) \rightarrow (J = l+1/2)$ between levels, separated due to the spin-orbit interaction, form what is known as the spin-flip resonance. Various theoretical descriptions have been developed to study the spin-flip resonance: a single-particle model to study the strength and centroid energy [42], QRPA and QTDA models to study the strength distribution [43, 44, 42].

The residual particle-hole interaction on the spin-isospin channel moves the spin-flip resonance to higher energies and also acts as a doorway into the fragmentation of the M1 strength. The particle-hole interaction however has a very small effect on the scissors resonance (orbital part of the M1 strength) and it remains at lower energies 2-4 MeV [44]. The scissors and spin-flip resonances are shown in figure 2.12 for nuclei in the medium-heavy (^{56}Fe), heavy (^{156}Gd) and very heavy (^{238}U) regions [45]. While the scissors resonance remains between 2-4 MeV excitation energy, the spin-flip resonance's centroid varies over many MeV. It can also be seen that the spin-flip resonance contributes most to the M1 strength.

Possible spin-flip and scissors transitions are shown in the Nilsson diagram, for the transition $1\mathrm{h}\frac{9}{2}- > 1\mathrm{h}\frac{11}{2}$, in figure 2.11. The spin-flip is a single-particle transition between levels separated by the spin-orbit interaction, hence the spin-flip strength will be localized at the energy of the spin-orbit gap in closed shells for spherical nuclei. Deformed nuclei have a splitting of the Nilsson energy levels causing the spin-flip strength to be spread apart around the spherical energy centroid. The spin-flip resonance centroid is usually found at

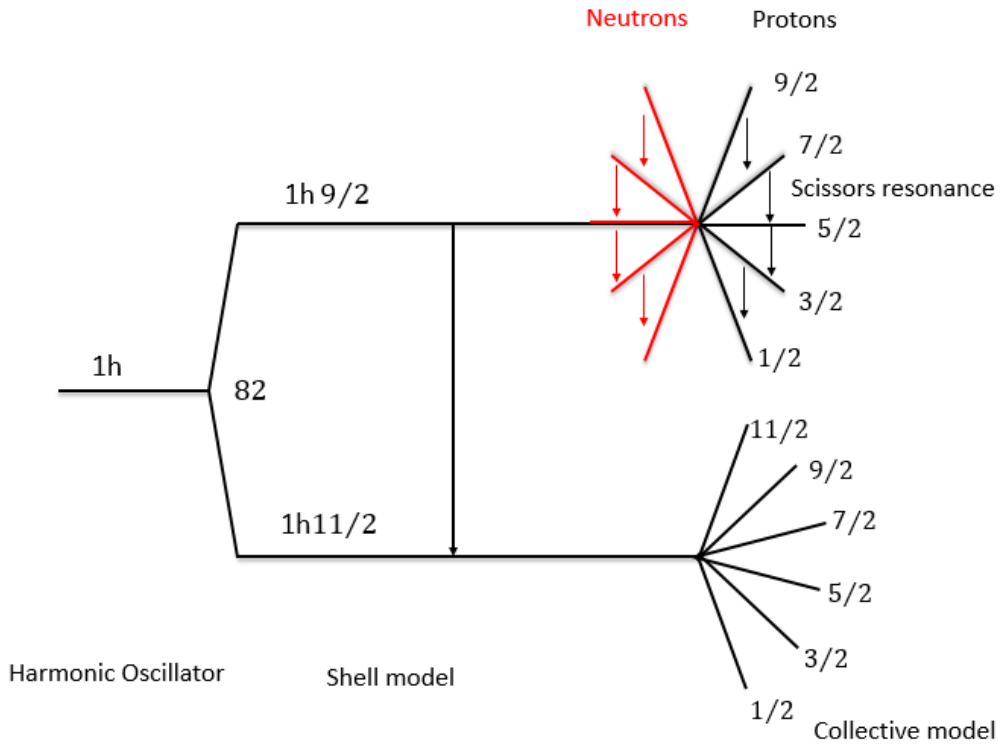

Figure 2.11: Illustration of the spin-flip and scissors resonance with the example of the $1h\frac{9}{2} - > 1h\frac{11}{2}$ transition.

a typical excitation energy [46]:

$$E_x \simeq 41A^{-1/3}MeV. \tag{2.28}$$

Studies (in the rare-earth region) using a schematic model and QRPA have shown that when the spin-spin proton-neutron coupling is not too strong, the M1 strength is separated into a pure proton and neutron collective spin-flip state [47, 48]. With increasing strength an isovector and isoscalar mode can be identified separately. The isovector part is normally at higher energies than the isoscalar part. This is illustrated in figure 2.13 where the splitting of the spin-flip strength in ^{238}U, ^{208}Pb and ^{154}Sm can be clearly seen.

2.4.4 Lorentzian functions

Lorentzian functions are used to describe the resonances. The GEDR was first described through a standard Lorentzian (SLO) with an energy and temperature independent width [49]:

$$f_{E1}^{SLO} = 8.68 \times 10^{-8} \frac{\sigma_0 E_\gamma \Gamma_0^2}{(E_\gamma^2 - E_0^2)^2 + E_\gamma^2 \Gamma_0^2} \tag{2.29}$$

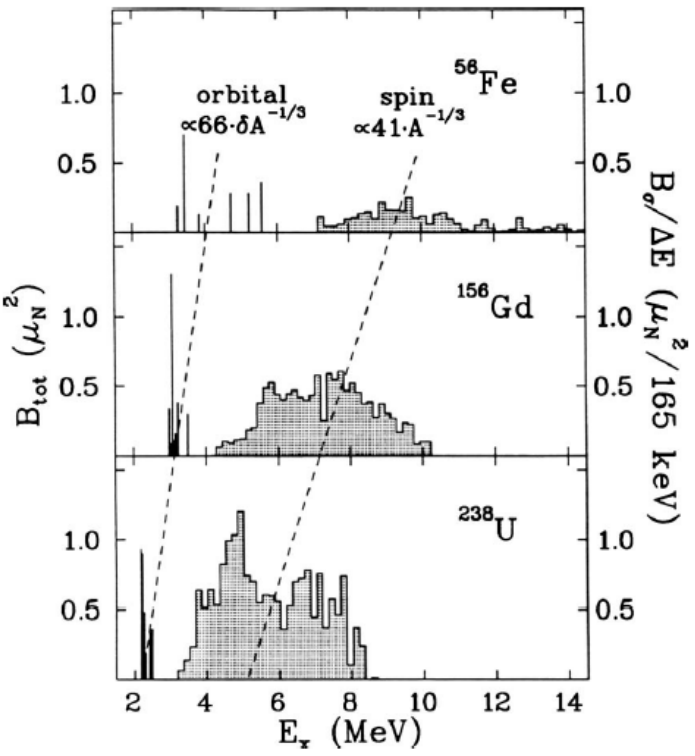

Figure 2.12: The spin-flip and scissors resonance for nuclei in the medium-heavy (^{56}Fe), heavy (^{156}Gd) and very heavy (^{238}U) regions [45].

where σ_0, Γ_0^2 and E_0^2 are the peak cross-section, GEDR width and peak centroid respectively. It was found that this function overestimates the strength at and below the neutron separation energy. The Lorentzian function was then used with an energy dependent width $\Gamma(E_\gamma)$ [49]:

$$f_{E1}^{LO} = 8.68 \times 10^{-8} \frac{\sigma_0 E_\gamma \Gamma_0 \Gamma(E_\gamma)}{(E_\gamma^2 - E_0^2)^2 + E_\gamma^2 \Gamma_0^2}. \tag{2.30}$$

The width was also improved to be temperature and energy dependent. The width is then given by [49]:

$$\Gamma(E_\gamma, T) = \Gamma_0 \frac{E_\gamma^2 + 4\pi^2 T^2}{E_0^2} \tag{2.31}$$

where S_n, a and T is the neutron separation energy, BSFG level density parameter and temperature $T = \sqrt{\frac{S_n - E_\gamma}{a}}$ respectively. The short coming of this description is that it fails to describe the electric operator in the limit of zero E_γ. The LO function was then improved to the generalized Lorentzian (GLO) function [50]:

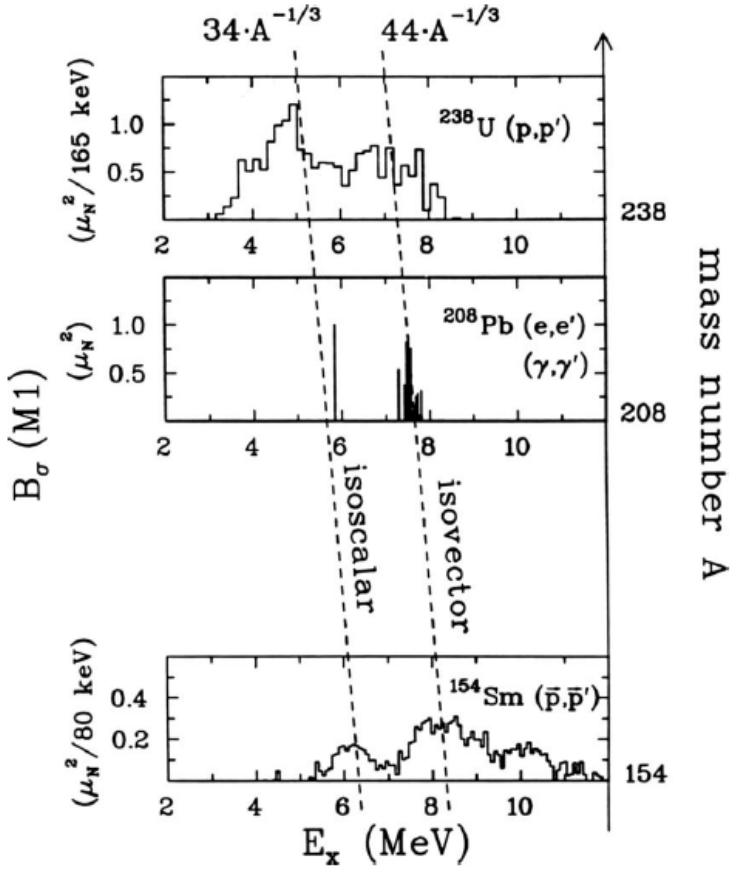

Figure 2.13: The spin-flip strength distribution for ^{238}U, ^{208}Pb and ^{154}Sm showing the split spin-flip resonance [32].

$$f_{E1}^{GLO} = 8.68 \times 10^{-8} \sigma_0 \Gamma_0 \left[\frac{E_\gamma \Gamma(E_\gamma, T)}{(E_\gamma^2 - E_0^2)^2 + E_\gamma^2 \Gamma_0^2} + 0.7 \frac{\Gamma(E_\gamma = 0, T)}{E_0^3} \right]. \quad (2.32)$$

This description was found to work in the mass region $A \approx 55 - 150$ and $A \approx 175 - 197$. For the mass region $A \approx 150 - 175$ this description underestimates the $f(E_\gamma)$ for strongly deformed nuclei. For the mass region $A \approx 150 - 175$ an adapted width is used [50]:

$$\Gamma(E_\gamma, T) = k_0 + (1 - k_0) \left(\frac{E_\gamma - \epsilon_0}{E_0 - \epsilon_0} \right) \frac{\Gamma_0 (E_\gamma^2 + 4\pi^2 T^2)}{E_0^2} \quad (2.33)$$

where k_0 is an empirical expression depending on the mass of the nucleus. Using this width with the Lorentzian function is known as the enhanced generalized Lorentzian (EGLO) function. For M1 resonances the SLO is commonly used, but any of the Lorentzian function can be used depending on the nucleus mass and the reproduction of experimental values.

2.5 Astro-physical implications

The program Talys [1] uses the statistical emission model Hauser-Feshbach (HF) to calculate astrophysical reaction rates, such as (n,γ). It simulates nuclear reactions which involve γ-rays, neutrons, protons, deuterons, tritons, ^{3}He and α-particles. The NLD and PSF are needed as input parameters for the HF model.

Photon strength functions play an important role in nuclear reactions occurring in nature. The rate of electron capture reactions depends on the properties of the giant Gamow-Teller resonance. Electron capture reactions are important because they cool the core of stars involved in explosions and accelerate the stars gravitational collapse. High energy neutrinos traveling outward from the star may heat nuclei in the mantle, exciting various giant resonances in the process. It is believed that certain elements can only be formed by giant resonance decay products in these reactions [20].

Resonances on the low-energy part of the GEDR such as the E1 pygmy resonance have an impact on the r-process nucleosynthesis [3]. The blue curve in figure 2.14 shows the r-abundance calculated using the GEDR and pygmy resonances. This produces nuclei in the mass region of A $\approx$ 130 with more accuracy. The green curve is the r-abundance calculated using only the GEDR, this calculation produces nuclei in the mass region of A $\approx$ 90-110 with more accuracy. The inclusion of the pygmy resonance clearly has a large impact on the result of the calculation. The red curve shows the solar r-abundance distribution.

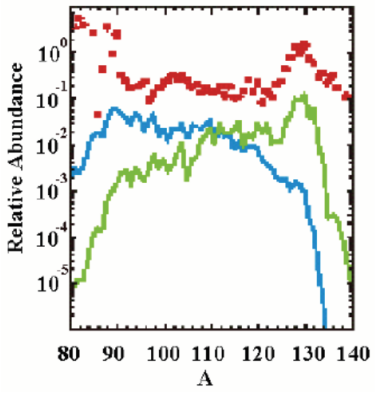

Figure 2.14: The red curve is the solar r-abundance distribution, the blue curve is the r-abundance excluding the pygmy resonance, and the green curve is the r-abundance including the pygmy resonance [3].

The magnetic dipole responses of nuclei are important for supernova modeling. It is used in calculating the inelastic neutrino-nucleus scattering cross section used in supernova dynamics [51]. To be able to describe inelastic scattering processes, information is needed on the $T_0 \rightarrow T_0$ isospin component of Gamow-Teller (GT) strengths, where T_0 is the ground-state isospin. Since a large amount of nuclei is typically involved in supernova reactions, it will take a lot of time and resources to measure each GT strength individually and the use of models are preferred. Figure 2.15 shows the neutrino inelastic scattering cross section of ^{52}Cr. The solid histograms are neutrino cross sections obtained from M1 strengths and the dashed histogram is cross sections obtained from shell-model calculations [52].

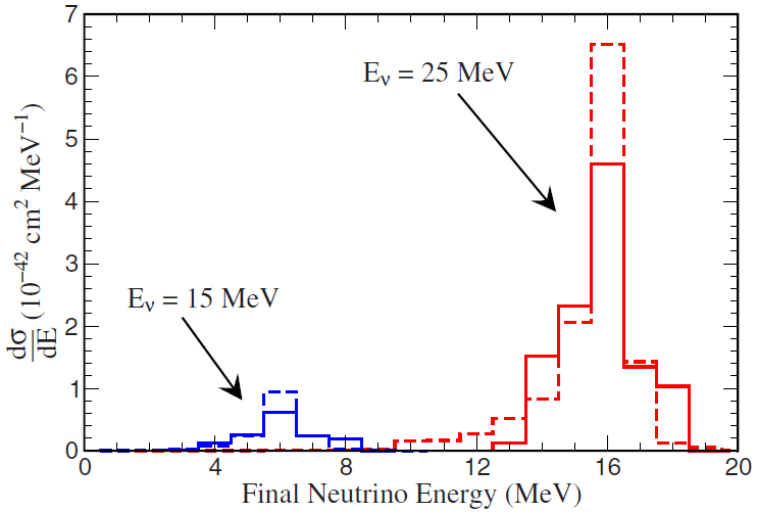

Figure 2.15: Neutrino differential inelastic scattering cross section of ^{52}Cr for two typical neutrino scattering energies E_ν =15 (blue) and 25 MeV (red). The solid histogram is cross sections obtained from M1 strengths and the dashed histogram is data obtained from shell-model calculations [52].

Chapter 3

The Oslo Method

By using various analytical techniques the NLD and PSF can be simultaneously extracted from particle-γ data. The combination of these techniques are called the Oslo method. The main steps in this method are:

1. Calculate and remove Compton background, single and double escape peaks and effects from pair production. This leaves only full-energy deposit events.
2. Extract the first generation γ-rays using the first generation method.
3. Simultaneous extraction of the NLD and PSF.
4. Normalization of the NLD and PSF.

The Oslo method is described in detail in various articles so only a brief overview of the methods will be given. For more details consult references [4, 53].

3.1 Full energy deposit events

Nuclei at excitation energies above 2-4 MeV (depending on the nucleus mass) have a high density of levels. γ-transitions in this high density region cannot be distinguished, since the spacing between levels are to small. This results in a statistical γ-spectrum with no identifiable discrete γ-ray energies. To extract useful information the statistical spectra have to be corrected by removing the Compton scattering, photo-electric and pair production events that do not result in a full energy deposit. Only full γ-ray energy deposit events are considered.

A γ-ray can enter the detector, deposit some energy and then escape before depositing all its energy. Such an event will form part of the Compton background scattering. If pair production occurs an annihilation event can produce

two annihilation photons with 511 keV energy each. If this annihilation process is close to the edge of the detector, one photon may escape resulting in a single escape peak at $E_\gamma - 511$ keV. If both annihilation photons escape a double escape peak is formed at $E_\gamma - 1022$ keV. All these events need to be removed. Many unfolding methods were developed over the years that can do this: The inverse matrix method [54, 55], stripping method [56], neural network method [57] and the folding iteration method [58]. According to reference [59] the inverse matrix method and the folding iteration method give the unfolded spectra a realistic shape, however large oscillations from channel to channel may introduce a wrong overall shape due to systematical errors for the stripping method.

The Oslo method uses a folding iteration method to estimate the shape of a spectrum that includes single and double escape peaks and the Compton background. The photoelectric effect is the dominant transfer mechanism for energies below ≈ 100 keV. The threshold of the experiment is usually set higher and the possible photoelectric effects are ignored. The spectrum is then smoothed and normalized to minimize oscillation from channel to channel. The smoothed and normalized spectrum is then subtracted from the experimental spectrum in the Compton subtraction method that utilizes the response function. The result is a matrix that contains only the full energy deposit events called the unfolded matrix [59].

3.1.1 Response function

The detector response function (used in the folding iteration method) is given by $R(E, E_\gamma)$ where E is the energy deposited into the detector and E_γ is the energy of the incoming γ-ray. Ideally this should be measured for every E_γ, however this is not possible. Instead, the response function is measured for a few mono-energetic γ-rays and the spectra is interpolated to obtain the response function for all E_γ. The mono-energetic γ-rays that were measured with the NaI(Tl) CACTUS-array (see chapter 4) are [59]: 122, 245, 344, 662, 1173, 1333, 1836, 4439, 6130 and 15110 keV. From these spectra the single and double escape, the full energy and annihilation peaks are removed. The parts remaining are the Compton, back scattering and pile-up events. The reason for removing these peaks are:

- to simplify the interpolation between different response functions because the positions and intensities have different energy dependencies.
- to easily create a new response function if the energy resolution of the current response function differs from the experimental energy resolution.
- to smooth parts of the spectrum with different energy resolutions as is needed in the Compton subtraction method (see section 3.1.3).

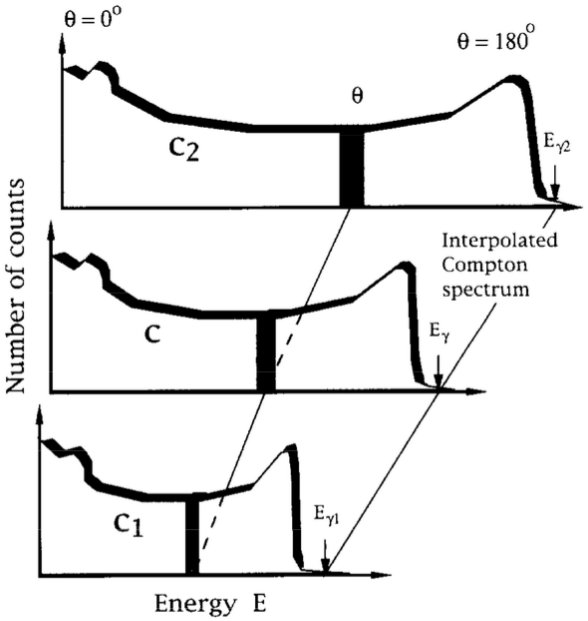

Figure 3.1: The Compton interpolation between channels with the same scattering angle θ [59].

The single and double escape, the full energy and annihilation peaks can be interpolated by a Gaussian distribution. The length of the Compton background differs due to their respective full energy values. This means the Compton background must be interpolated between channels that correspond to the same γ-ray scattering angle θ. This is illustrated in figure 3.1. As γ-rays scatter off electrons in the detector material they transfer energy E given by:

$$E = E_\gamma - \frac{E_\gamma}{1 + \frac{E_\gamma}{m_e c^2}(1 - cos\theta)}. \tag{3.1}$$

Below 200 keV the spectrum is dominated by backscattering and background events and interpolation can happen between the same channel numbers. The energy deposited into the detector below 200 keV is given by:

$$E_{backscatter} = E_\gamma I \left(1 + \frac{2E_\gamma}{m_e c^2}\right). \tag{3.2}$$

Above the Compton edge, interpolation is done between channels with the same channel number. To calculate the counts in the interpolated spectrum the following equation is used [59]:

$$c(E) = \left(\frac{dE}{d\theta}\right)^{-1}_{E_\gamma} \left[c_1(E_1) \left(\frac{dE}{d\theta}\right)_{E_{\gamma 1}} + \frac{E_\gamma - E_{\gamma 1}}{E_{\gamma 2} - E_{\gamma 1}} \times \left(c_2(E_2) \left(\frac{dE}{d\theta}\right)_{E_{\gamma 2}} - c_1(E_1) \left(\frac{dE}{d\theta}\right)_{E_{\gamma 1}} \right) \right] \tag{3.3}$$

where E_γ, $E_{\gamma 1}$ and $E_{\gamma 2}$ are the centroids for the full energy deposit peaks of the interpolated and reference spectra. E, E_1 and E_2 are the energies deposited into the detector by the γ-ray. $\left(\frac{dE}{d\theta}\right)_{E_{\gamma 1}}$ and $\left(\frac{dE}{d\theta}\right)_{E_{\gamma 2}}$ is due to the scattering angle on the energy deposited by the γ-ray [59].

3.1.2 The folding iteration method

The response matrix R_{ij} is defined as the response in channel i from a γ-ray of energy corresponding to channel j. Folding can then be expressed as:

$$f = \mathbf{R}u$$

where f is the folded spectra, u is the unfolded spectra and $\mathbf{R}$ is the measured spectra. There are two ways of operating the folding iteration method: the ratio approach which calculates the next trial function by:[1]

$$u_{i+1} = u_i(\frac{r}{f_i}).$$

where r is the measured spectrum. The second way of operating the folding iteration method is the difference approach which calculates the next trial function by:

$$u_{i+1} = u_i + (r - f_i).$$

According to reference [59] the ratio approach gives problems when $f = 0$, since it divides by f. The Oslo method utilizes the difference approach. The method is as follows [59]:

1. Let $u_0 = r$
2. Then $f_0 = \mathbf{R}u_0$
3. Using the difference approach u_1 is calculated by: $u_1 = u_0 + (r - f_0)$
4. Repeat step 2 and 3 until $f_i \approx r$. Normally it takes 10 to 30 iterations:

[1] The $_i$ indexes here refer to the number of iterations.

$$f_1 = \mathbf{R}u_1$$
$$u_2 = u_1 + (r - f_1)$$
$$\vdots$$
$$f_{i+1} = \mathbf{R}u_{i+1}$$
$$u_{i+1} = u_i + (r - f_i).$$

Figure 3.2 shows the results from continuous foldings. After each folding the observed spectra is reproduced better. It has been observed that there are undershoots next to pronounced peaks in the unfolded spectrum [59]. To account for this let $FWHM_{response} = 0.5FWHM_{experiment}$. The iteration method gives an unfolded spectrum that can be used as a starting point for the Compton subtraction method.

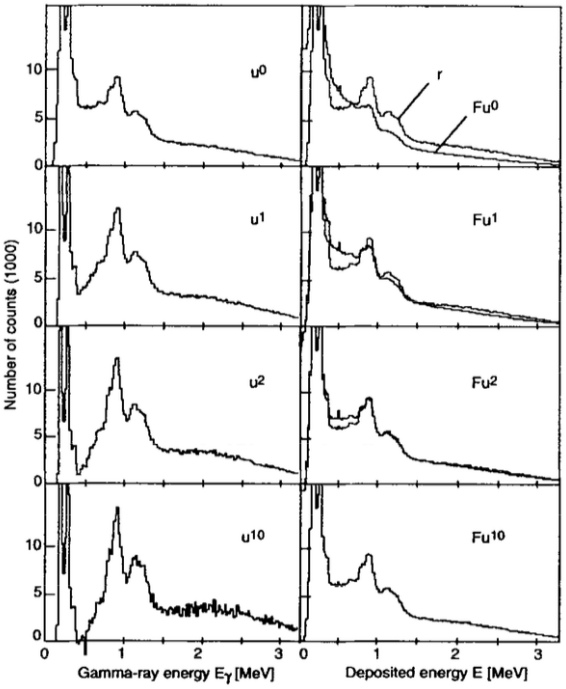

Figure 3.2: The results from continuous unfolding on a spectrum of ^{162}Dy. r is the observed spectrum, u is the unfolded spectrum and Fu is the folded spectrum [59].

3.1.3 The Compton subtraction method

The Compton subtraction method begins once you have the unfolded spectrum u. Subtract the Compton contribution from the observed spectrum by: [2]

[2]The (i) indexes here refer to the channel number of the spectra.

$$v(i) = p_f(i)u_0(i) + w(i) \tag{3.4}$$

where

$$\begin{aligned} w(i) &= u_s(i) + u_d(i) + u_a(i) \\ u_s(i - i_{511}) &= p_s(i)u_0(i) \\ u_d(i - i_{1022}) &= p_d(i)u_0(i) \\ u_a(i_{511}) &= \sum_i p_a(i)u_0(i) \end{aligned}$$

$p_f(i)u_0(i)$ is the full energy peak, $p_s(i)u(i)$ is the single escape peak, $p_d(i)u(i)$ is the double escape peak, $\sum_i p_a(i)u(i)$ is the contribution from annihilation, i_{511} and i_{1022} are the channels corresponding to energy 511 keV and 1022 keV. The probabilities for a single, p_s, and double, p_d, escape peak, full energy deposit, p_f, and annihilation event, p_a, are taken from [59].

$\vec{u}_a$ has all its counts in one channel so it should be smoothed by 1 FWHM so that it can have the same energy resolution as the observed spectrum. The energy resolution of the spectra $p_f u_0$, u_d, u_s, is determined by the response matrix and observed spectrum's energy resolution: $\sqrt{1^2 - 0.5^2} = 0.87$ FWHM. These spectra should be smoothed by 0.5 FWHM to have the same energy resolution as the observed spectrum. The Compton background spectrum can then be extracted by:

$$c(i) = r(i) - v(i). \tag{3.5}$$

This spectrum can then be further smoothed by 1 FWHM to obtain a smoothed Compton background that is a slow changing function of energy. The smoothed Compton background and peak structures w are then subtracted from the observed spectrum r and corrected for the full energy probability p_f:

$$u(i) = \frac{r(i) - c(i) - w(i)}{p_f(i)} \tag{3.6}$$

$u(i)$ is then the spectrum without the single and double escape peak, Compton background and annihilation contributions. The observed spectrum r, the Compton background c and the resulting spectrum after unfolding and Compton background subtraction u of ^{152}Eu and ^{162}Dy [59] are shown in figure 3.3. This spectrum can still be corrected for the detector efficiency ϵ, taken from reference [59]. ϵ is also multiplied by the efficiency of the discriminator level of the experimental setup i.e. the ADC thresholds and timing should also be taken into account. This then gives:

$$U(i) = \frac{u(i)}{\epsilon(i)} \tag{3.7}$$

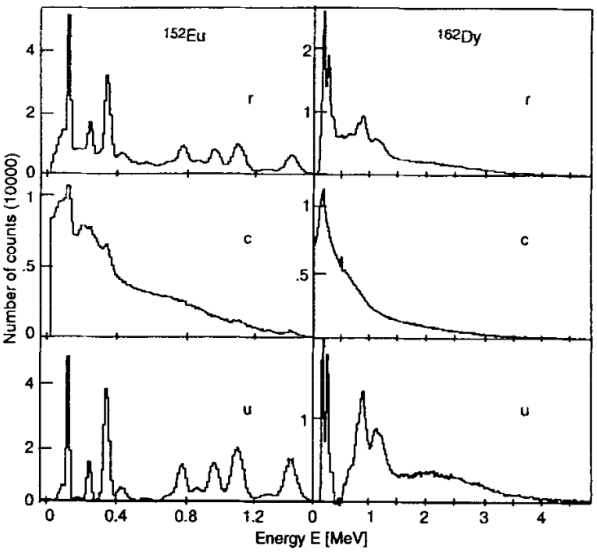

Figure 3.3: The observed spectrum r, the Compton background c and the resulting spectrum after unfolding and Compton background subtraction u of ^{152}Eu and ^{162}Dy [59].

3.2 First generation matrix

The distribution of the primary γ-rays contains the relevant information that is needed to calculate the nuclear level density and photon strength function. Highly excited nuclei will primarily decay through a cascade of γ-rays. The technique to sort through and obtain the primary γ-rays is called the first generation method. This method assumes that a state populated by a γ decay has the same properties as when that state is populated directly through the reaction. This assumption is true for high level densities where the nucleus is in a compound state prior to γ-emission [60].

Beginning at the highest excitation region (bin) of the unfolded and Compton subtracted spectrum, a γ-ray spectrum, f_i, is produced from the particle-γ coincidences [3]. The first generation γ-ray spectrum for the highest excitation region is found by:

$$h_i = f_i - g_i \tag{3.8}$$

where h_i is the first generation spectrum and $g_i = \sum_j n_{ij} w_{ij} f_j$ is the weighted sum of all the γ-ray spectra where $i < j$. w_{ij} is the probability of a decay of states in bin i to states in bin j where $\sum_j w_{ij} = 1$. w_{ij} can be seen as the branching ratio for primary γ-rays depopulating level i. Each level i and j have different populating cross sections and n_{ij} is the correcting factor that

[3] The $_i$ indexes here refer to the subsequent bin number.

accounts for this. It is calculated so that the area of each γ-ray spectrum f_{ij} multiplied by the correcting factor n_{ij} has the same number of cascades [61].

The distribution of w_{ij} is the same as h_i, so they can be simultaneously determined through a fast converging iterative method [62]:

1. Apply a trial function w_{ij}, for example a constant function or an unfolded spectrum f_i
2. Calculate h_i using equation 3.8
3. Let h_i have the same energy calibration as w_{ij} and normalise the area of h_i to 1
4. if $w_{ij} \approx w_{i-1,j-1}$ the method has converged. If this is not true repeat from step 2. Normally this takes 10-30 iterations.

n_{ij} can be calculated in two ways:

Singles normalisation: The cross section, as determined from single particle events, is equivalent to the density of populated states and therefore to the number of cascades [62]. The normalisation factor is given by:

$$n_i = \frac{S_j}{S_i} \tag{3.9}$$

where S_j and S_i are the cross-sections for bins j and i, respectively.

Multiplicity normalisation: Assume a N-fold population of a level E_x. The outcome of decays from this level will be N γ-rays cascading with the i^{th} cascade containing M_i γ-rays. The average γ-ray energy given by, $\langle E_\gamma \rangle$, will be equal to the total energy of the emitted γ-rays divided by the total number of γ-rays emitted [63]:

$$\langle E_\gamma \rangle = \frac{E_x N}{\sum_{i=1}^{N} M_i} = \frac{E_x}{\langle M \rangle}. \tag{3.10}$$

The multiplicity is then given by:

$$\langle M_i \rangle = \frac{E_x^i}{\langle E_\gamma \rangle} \tag{3.11}$$

where E_x^i is the excitation energy of bin i. The single particle cross-section is then given by $S_i = \frac{A(f_i)}{\langle M_i \rangle}$ where $A(f_i)$ denotes the area of the spectrum f_i. Substituting this into equation 3.9 returns a normalization factor of:

$$n_i = \frac{\langle M_i \rangle A(f_j)}{\langle M_j \rangle A(f_i)}. \tag{3.12}$$

If the multiplicity is considered to be well defined an area consistency check can be used on equation 3.8. Introduce a correction by setting $g = \alpha g$ where α is close to unity. The area of the first generation γ-ray matrix is then given by:

$$A(h) = A(f_i) - \alpha A(g) \tag{3.13}$$

This correlates to a γ-ray multiplicity of one. It can also be expressed by:

$$A(h) = \frac{A(f_i)}{\langle M_i \rangle} \tag{3.14}$$

By combining equations 3.13 and 3.14 we get a new expression for the correction factor α:

$$\alpha = \frac{(1 - \frac{1}{\langle M_i \rangle})A(f_i)}{A(g)}. \tag{3.15}$$

The correction is always useful in case an improper weighting function w_{ij} is used [62].

3.3 Extracting nuclear level density and photon strength function

Fermi's Golden Rule about decay rates states:

$$\lambda_{if} = \frac{2\pi}{\hbar} | < f|\hat{H}_{int}|i > |^2 \rho(E_f) \tag{3.16}$$

where λ_{if} is the decay rate from the first state i to the final state f, $\rho(E_f)$ is the level density at the final energy and $< f|\hat{H}_{int}|i >$ is the transition matrix element [64].

The decay of a γ-ray to a specific final energy is independent of the reaction that formed the nucleus. The probability for a γ-ray to decay from excitation energy E_x to E_f, with energy $E_f = E_x - E_\gamma$, is proportional to the level density at the final energy $\rho(E_f)$ and the γ transmission coefficient $T_{if}(E_\gamma)$. The first generation matrix is proportional to the decay probability and therefore it can be factorized as [53, 4]:

$$P(E_x, E_\gamma) \propto \rho(E_f) T_{if} \tag{3.17}$$

where $\rho(E_f)$ is the level density at the final energy and T_{if} is the gamma transmission coefficient. Brink's hypothesis states that the collective giant dipole mode built on an excited state has the same properties as if it was built on the ground state [65]. This hypothesis implies that the gamma transmission coefficient does not depend on the initial and final states, but only the γ-ray energy:

$$P(E_x, E_\gamma) \propto \rho(E_f)T(E_\gamma). \tag{3.18}$$

Equation 3.16 is comparable to 3.18, with the only difference being that equation 3.16 depends on the initial and final states, while equation 3.18 depends only on the γ-ray energy. As long as the experimental first generation matrix has been correctly normalized for every excitation energy bin E_f through either the singles or multiplicity normalization described above, the total probability $P(E_f, E_\gamma)$ for γ-decay is unity [4]:

$$\sum_{E_\gamma=E_\gamma^{min}}^{E_x} P(E_x, E_\gamma) = 1. \tag{3.19}$$

A theoretical approximation for the normalized first generation matrix can now be found by:

$$P_{th}(E_x, E_\gamma) = \frac{T(E_\gamma)\rho(E_x - E_\gamma)}{\sum_{E_\gamma=E_\gamma^{min}}^{E_x} T(E_\gamma)\rho(E_x - E_\gamma)}. \tag{3.20}$$

Equation 3.20 fulfills the condition set by 3.19. The Zeroth-order estimate of T can be found by choosing $\rho^{(0)} = 1$, this gives [4]:

$$T^{(0)}(E_\gamma) = \sum_{E_x=max(E_i^{min},E_\gamma)}^{E_i^{max}} P(E_x, E_\gamma). \tag{3.21}$$

In order to find the higher order estimates of ρ and T a χ^2 least squares method is used to fit the $P(E_x, E_\gamma)$ deduced from measurements to the theoretical $P_{th}(E_x, E_\gamma)$:

$$\chi^2 = \frac{1}{N_{free}} \sum_{E_x=E_i^{min}}^{E_i^{max}} \sum_{E_\gamma=E_\gamma^{min}}^{E^x} \left(\frac{P_{th}(E_x, E_\gamma) - P(E_x, E_\gamma)}{\delta P(E_x, E_\gamma)} \right)^2 \tag{3.22}$$

where N_{free} is the number of degrees of freedom and $\delta P(E_x, E_\gamma)$ is the uncertainty in the first generation matrix. Through minimizing the χ^2 all possible solutions are constructed:

$$\tilde{\rho}(E_x - E_\gamma) = \rho(E_x - E_\gamma)A\exp(\alpha(E_x - E_\gamma)) \tag{3.23}$$

$$\tilde{T}(E_\gamma) = T(E_\gamma)B\exp(\alpha E_\gamma) \tag{3.24}$$

where α is the slope and A and B are the normalization constants which will be discussed in the section 3.4. A and α are the free parameters in the χ^2 minimization. There is an infinite number of solutions that can be calculated

using equations 3.23 and 3.24.

Normally this method converges well, however in some cases where there are few data points, e.g. at high energies, the method needs to be enhanced. By restricting the maximum change of data points in ρ and T within one iteration to a certain percentage N, the method can be generalized. In other words, the data points calculated in the new iteration is checked if it lies within an interval determined by the old iteration:

$$\frac{old}{1+\frac{N}{100}} \leq new \leq (1+\frac{N}{100}) \times old. \tag{3.25}$$

The possible errors made during the unfolding and extraction procedure is calculated through a simulation in order to simplify the process. It is described in detail in reference [4]. The errors in $\rho(E_f)$ and $T(E_f)$ are calculated 100 times and then averaged for reasonable statistics by:

$$\delta\rho(E_f) = \frac{1}{\sqrt{100}}\sqrt{\sum_{i=1}^{100}[\rho_i^{(s)}(E_f) - \rho(E_f)]^2} \tag{3.26}$$

$$\delta T(E_f) = \frac{1}{\sqrt{100}}\sqrt{\sum_{i=1}^{100}[T_i^{(s)}(E_f) - T(E_f)]^2}. \tag{3.27}$$

3.4 Normalisation

Since there exists an infinite amount of solutions for $\rho(E_f)$ and $T(E_\gamma)$, their normalization to experimental data needs to be performed. This finds the correct solution, in other words, the correct values for A, B and α are found. At low excitation energies (below 2 MeV) the level density normalization can be accomplished using experimentally measured level densities by just counting observed levels. At the neutron separation energy normalization is achieved from level densities calculated from neutron resonance spacing data [4]. The starting point is equations 2.2 and 2.3. The average neutron resonance spacing $D_{l=0}$ can now be written as:

$$\frac{1}{D_0} = \frac{1}{2}(\rho(S_n, J = I + \frac{1}{2}) + \rho(S_n, J = I - \frac{1}{2})) \tag{3.28}$$

where I is the spin of the target nucleus as determined from neutron resonance experiments. It is assumed that both spin $+\frac{1}{2}$ and $-\frac{1}{2}$ contribute equally to the level density at the neutron binding energy S_n. The total NLD at the neutron separation energy can be found by combining equations 2.2,2.3 and 3.28. This gives:

$$\rho(S_n) = \frac{2\sigma^2}{D_0} \times \frac{1}{(I+1)\exp(-\frac{(I+1)^2}{2\sigma^2}) + I\exp(-\frac{I^2}{2\sigma^2})} \tag{3.29}$$

where σ^2 is calculated by equation 2.4. The calculated level density cannot be compared directly at the neutron separation energy since the ρ function is extracted up to $E_{max} - E_{\gamma\,min}$. E_{max} is the maximum E_x cut and $E_{\gamma\,min}$ is the minimum γ-ray energy cut on the first generation matrix. This problem is solved by extrapolating the extracted ρ function with a constant temperature level density.

The parameters A and α of the transformation 3.23 are adjusted until the data fit the level density equation in an excitation energy interval between for example 0-1 MeV and 4-5 MeV. The energy interval may change depending on experimental data.

The parameter B is calculated from the experimental average total radiative width $< \Gamma_\gamma(S_n, J_T \pm \frac{1}{2}, \pi_T) >$ according to [53]:

$$< \Gamma_\gamma(S_n, J_T \pm \frac{1}{2}, \pi_T) >= \frac{D_0}{4\pi} \int_0^{S_n} dE_\gamma T(E_\gamma)\rho(S_n - E_\gamma)\times \sum_{J=-1}^{1} g(S_n - E_\gamma, J_T \pm \frac{1}{2} + J) \tag{3.30}$$

where J_T, π_T are the spin and parity of the target nucleus, $\rho(S_n - E_\gamma)$ is the experimental level density and g is the spin distribution of the level density given by [14]:

$$g(E, J) \simeq \frac{2J+1}{2\sigma^2} \exp[-(J + \frac{1}{2})^2/2\sigma^2]. \tag{3.31}$$

The spin distribution is normalized to $\sum_J g(E, J) \approx 1$. D_0 and Γ_γ values can be obtained from literature, for e.g. [66] or if no information is known, like in the case of short lived targets, then D_0 and Γ_γ can be calculated using Talys [1]. Assuming the decay is dominated by dipole radiation ($L = 1$) we get:

$$BT(E_\gamma) = B(T_{E1}(E_\gamma) + T_{M1}(E_\gamma)). \tag{3.32}$$

The relation between the photon strength function and γ transmission coefficient is given by

$$T_{X,L=1}(E_\gamma) = 2\pi E_\gamma^3 f_{X1}(E_\gamma). \tag{3.33}$$

The photon strength function can then be easily calculated by:

$$f(E_\gamma) = \frac{1}{2\pi E_\gamma^3} BT(E_\gamma). \tag{3.34}$$

Assuming the γ transitions are of dipole nature, the PSF can be written in terms of the (γ, n) cross section $\sigma(E_\gamma)$ by [67]:

$$f(E_\gamma) = \frac{\sigma(E_\gamma)}{3E_\gamma(\pi\hbar c)^2}. \tag{3.35}$$

By using this equation $\sigma(E_\gamma)$ can be converted to PSF and vice versa. The converted PSF can then be used to compare results.

3.5 Accuracy and possible shortcomings of the Oslo Method

A brief summary of the assumptions and systematic errors of the Oslo method will be given in this section. In the following the findings of reference [53] are briefly outlined.

3.5.1 The unfolding method

The unfolding method has been extensively tested and found to be accurate. A possible shortcoming of this method is that the γ-ray spectra have to be corrected for the total absorption efficiency of the NaI(Tl) crystals, used in the CACTUS array, for a given γ-ray energy. The influence of the absorption efficiency was tested in reference [53] by reducing it by 20% for γ-ray energies above 1 MeV. The level density extracted with this absorption efficiency was impervious to the total absorption efficiency, but the slope of the γ-ray strength function was increased due to the low efficiency at high γ-ray energy. However, the overall shape off the PSF remained unchanged.

3.5.2 The first generation method

The first generation method assumes that it does not matter how a nucleus is excited to an energy level with regards to γ-ray decay. In other words, it should not make a difference whether the energy level is populated by a decay from a higher energy level or directly by the nuclear reaction. This was tested in reference [53] by looking at the same compound nucleus created with different reactions, (^{3}He,α) and (^{3}He,^{3}He). ^{96,97}Mo [68], ^{161,162}Dy [69] and ^{171,172}Yb [70] were investigated using both reactions and the nuclear level densities and photon strength functions were similar, except at very low excitation energies.

Another assumption is that the nucleus is in a compound state before γ-ray emission. The characteristic time for compound nucleus formation is $\approx 10^{-18}$s and the life time of states in the quasi-continuum is $\approx 10^{-15}$s. The nucleus thermalizes before γ-ray emission. Calculations have supported this by showing that both, ^{160}Dy(^{3}He, $\alpha\gamma$) [71] with a 45 MeV ^{3}He beam and ^{46}Ti($p, p'\gamma$)

with a 15 MeV proton beam have small pre-equilibrium contributions for energies below 10 MeV. With excitation energies above 10 MeV this assumption is questionable, however the experiments analyzed using the Oslo method deal only with energies below 10 MeV.

Nuclei with large gaps between energy levels at low energies may lead to excitation energy regions called "empty valleys". These need to be excluded otherwise over or under subtraction may result that changes the low-energy part of the photon strength function. Mistakes in determining the weighting functions, such as the finite or mismatch of the detector resolution of the particle telescopes and CACTUS array (see section 5.2) have only minor influence on the results.

3.5.3 Extraction of level density and photon strength function

The extraction of the level density and PSF assume the validity of the Brink hypothesis. With high temperatures and/or spins in nuclear reactions, the Brink hypothesis may not be valid anymore. If the Brink hypothesis is not valid then equation 3.17 cannot be simplified to equation 3.18 which complicates the extraction method. Simulations [72] have shown that if the strength function is temperature dependent, the overall shape of the PSF remains similar, but the low γ-ray energy region is changed. Two sets of decay intensities and level schemes (nuclear realizations) were used, the results from these simulations are shown in figure 3.4. The temperature dependence of the PSF has been investigated experimentally several times in references [73, 74, 68, 75] and there has been no experimental evidence of any temperature dependence for excitation energies below 10 MeV, supporting the validity of the Brink hypothesis for the regions studied with the Oslo method. It should also be noted that the Oslo method does not take the uncertainties of D_0 and Γ_γ into account, however steps can be taken to include these uncertainties. These steps will be discussed in section 6.4

3.5.4 Parity and spin distribution

The positive and negative-parity distribution is assumed to be equal, an assumption which may break down for very light nuclei (but not for heavy nuclei). A large parity asymmetry will change the normalization point $\rho(S_n)$ up to a factor of 2 [53]. The change in normalization point $\rho(S_n)$ will change the slope of the NLD and PSF. Experiments suggest that the parity asymmetry is small for light nuclei so the change of $\rho(S_n)$ is small. The error of $\rho(S_n)$ and the absolute normalization of the PSF will not exceed 50% [53].

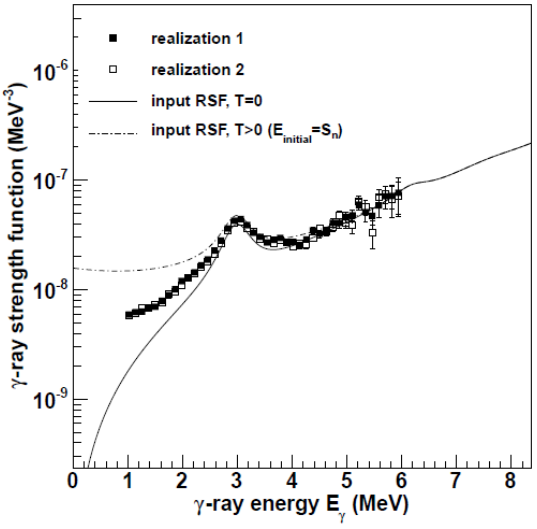

Figure 3.4: Simulated spectra of ^{163}Dy. The black and white squares are PSF for two different realizations of the nucleus. The solid line is the input PSF using a constant temperature model and the dashed line is the input PSF using a temperature= $\sqrt{S_n - E_\gamma}$ [53].

One of the largest uncertainties is the spin distribution of the reaction, since the intensity of the populated spin at the neutron separation energy is used in determining the slope of the NLD and PSF. Simulations [72] show that higher spins on initial levels of light nuclei lead to an enhanced PSF at low γ-ray energies. Different spin ranges, $\frac{1}{2} \leq J \leq \frac{7}{2}$, $\frac{1}{2} \leq J \leq \frac{13}{2}$ and $\frac{7}{2} \leq J \leq \frac{13}{2}$, were used and the effect on the NLD and PSF of ^{57}Fe were investigated using simulated data, as shown in figure 3.5. The NLD remained reasonably unchanged, but the PSF has increased strength at low E_γ.

Spin cutoff parameters are usually taken from, but are not limited to references [76] or [14] and a bell like spin distribution is assumed according to reference [14]. Different spin distributions, as shown in figure 3.6, can lead to a $\rho(S_n)$ value that is $10 - 50\%$ different. Typical reactions at the Oslo Cyclotron Laboratory (OCL) reach spins in the range 0-8$\hbar$ which is a relatively narrow spin range. This can be counterbalance by normalizing the NLD at the neutron separation energy. Calculations show that the main structures in level densities are present for a rather narrow spin range, and as such the narrow spin range has a small effect on the results.

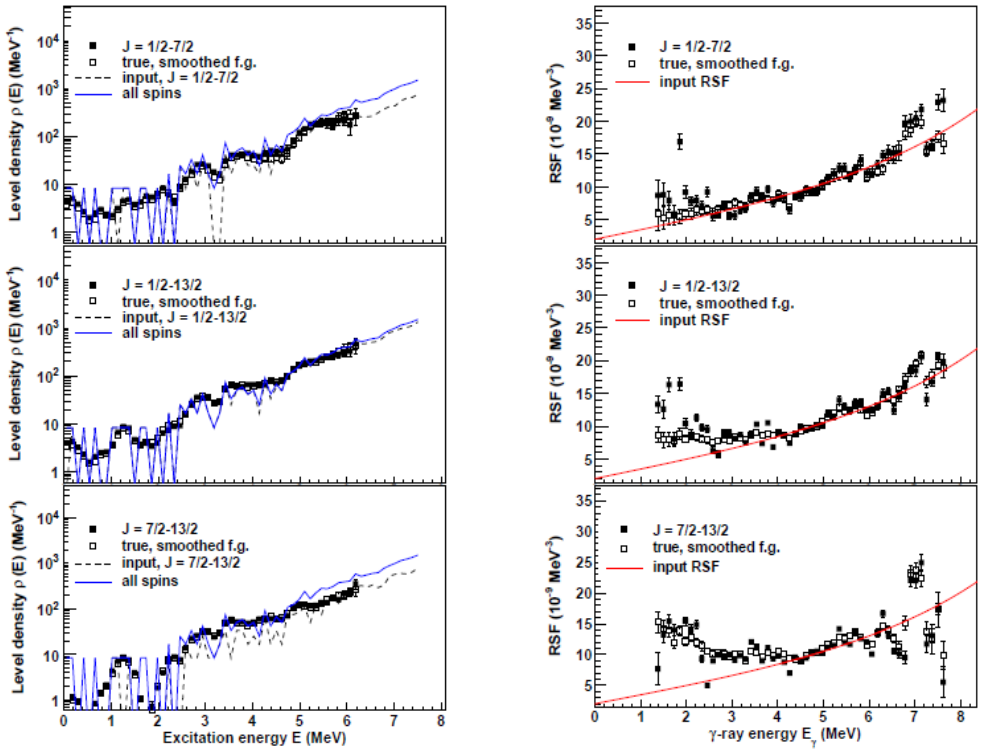

Figure 3.5: Different initial spin ranges and its effect on the level density and PSF for ^{57}Fe [53].

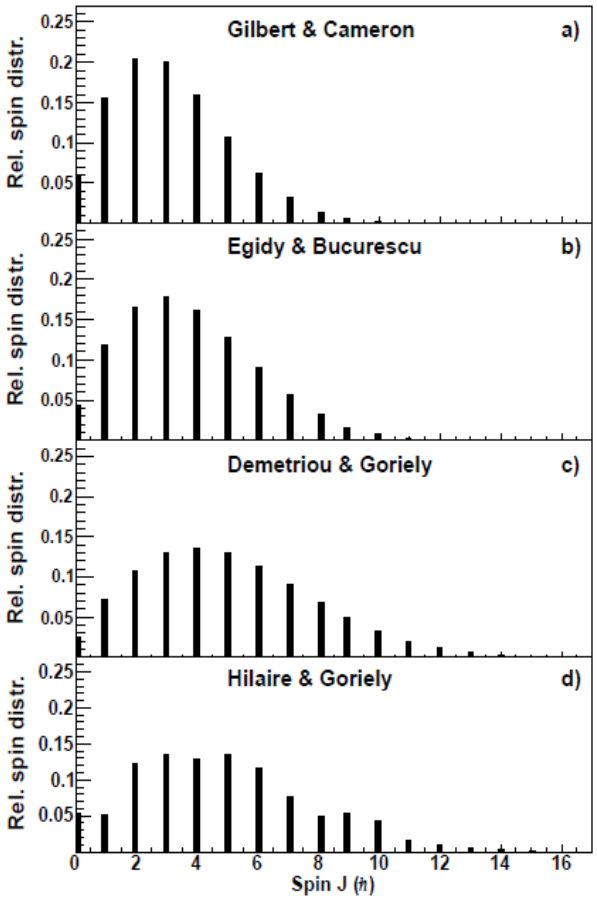

Figure 3.6: Various spin distributions of ^{44}Sc at $E = 8$ MeV that can be used in calculating $\rho(S_n)$ [53].

Chapter 4

Experimental Setup

The experiment was performed in Norway at the Cyclotron Laboratory of the University of Oslo (OCL). Using a MC-35 Scanditronix cyclotron a 12.5 MeV deuterium beam impinged on a self-supporting ^{181}Ta target of thickness 0.8 $\frac{mg}{cm^2}$. The beam is collimated using slit D1 and focused using quadrapole magnet Q1. The analyzing magnet bends the beam 90° towards the target chamber. Further collimation and focusing is done by slits D2, D3 and D4 and by quadrapole magnets Q2 and Q3. A diagram of the setup at the OCL is shown in figure 4.1. The beam reaching the target chamber typically has a diameter of 1-2 mm. The investigated reactions are $^{181}\mathrm{Ta}(d,p)^{182}\mathrm{Ta}$ ($Q = 3838.4$ keV) and $^{181}\mathrm{Ta}(d,d')^{181}\mathrm{Ta}$. The beam intensity was ≈ 2 particle nA. The SiRi particle telescope and CACTUS array detector systems, located in the target chamber, where used in this project. The CACTUS array is used to detect γ-rays and the SiRi particle telescopes detect charged particles.

4.1 Detector systems

4.1.1 SiRi particle telescope

The SiRi particle telescope, shown in Figure 4.2 consists of 8 thin silicon detectors (ΔE) segmented into 8 slices with thicknesses 130 μm positioned in front of the telescopes. The segmentation of the ΔE detectors are illustrated in figure 4.3. The SiRi particle telescopes also has 8 thick silicon detectors (E) positioned in the back of the telescope with thicknesses 1550 μm [78]. The detectors are positioned in a circle around the target. This gives a total of 64 detectors that are used to measure energy deposition used to identify particles produced in the nuclear reactions.

Each particle telescope covers a scattering angle between $\theta_{lab} = 126° - 140°$ in steps of 2°. A 10.5 μm aluminum foil is placed in front of the particle

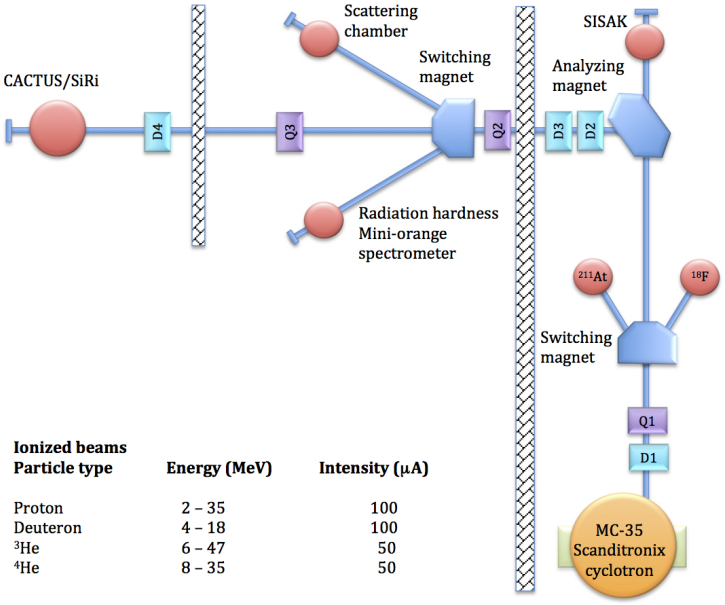

Figure 4.1: Diagram of the setup at the Oslo Cyclotron Laboratory [77].

telescopes to shield them from δ electrons that are produced in the reaction. The resolution for this work was 124 keV as obtained from the deuteron elastic peak. The SiRi particle telescope (figure 4.2) was placed at $\theta_{lab} = 133°$ with respect to the beam axis, this is illustrated in figure 4.4.

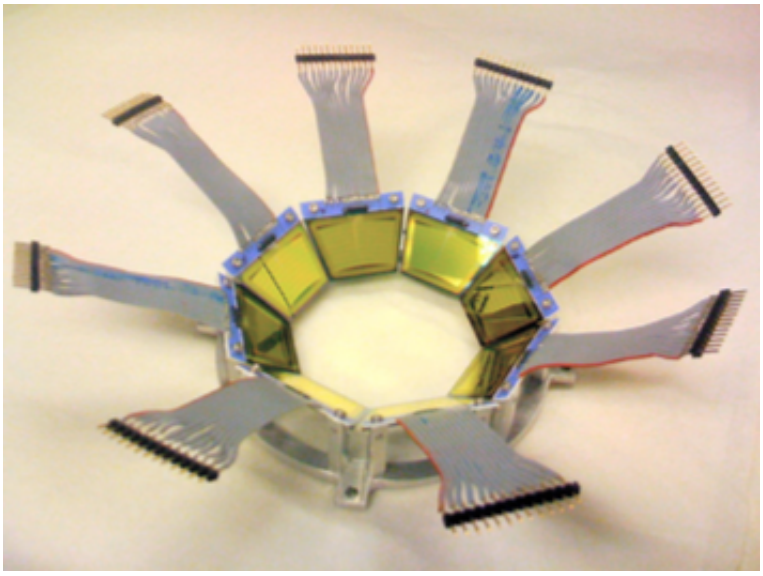

Figure 4.2: The SiRi particle telescope [79].

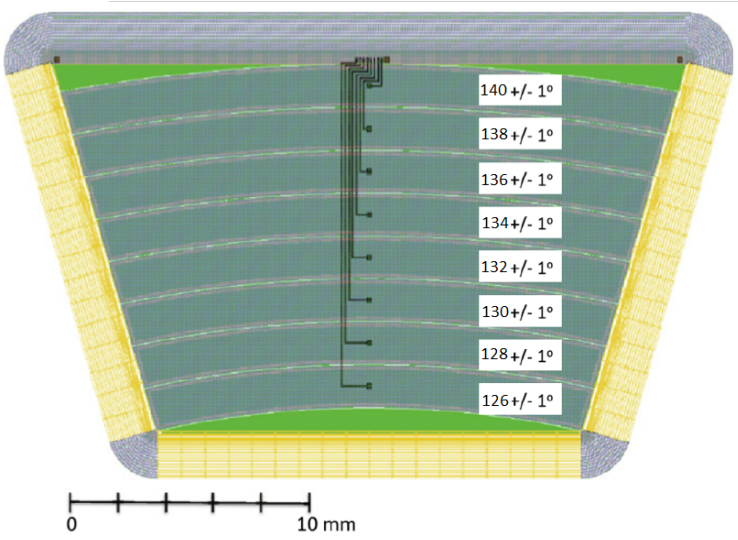

Figure 4.3: Layout of the front ΔE detector [79].

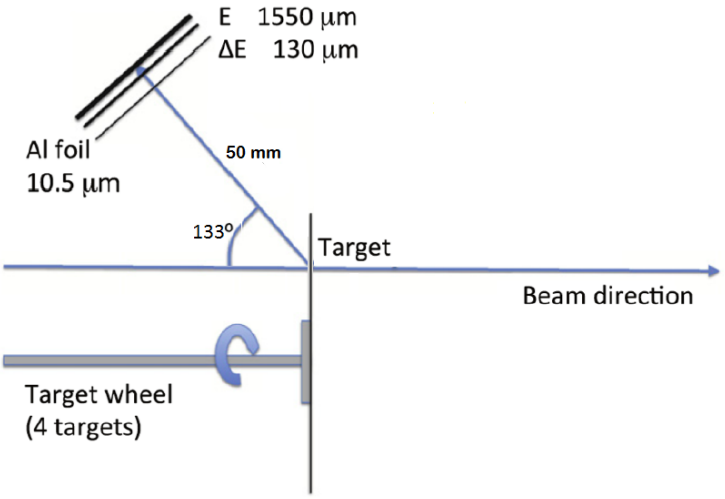

Figure 4.4: The SiRi particle telescope position relative to the beam line axis [79].

4.1.2 CACTUS array

The CACTUS array consists of 26 NaI(Tl) detectors positioned spherically around the target to detect the γ-rays coming from the reactions. The CACTUS array is shown in Figure 4.5. Each NaI(Tl) detector has a crystal with dimension 5" $\times$ 5" and is positioned 22 cm away from the target [80] covering a total of 17% of 4π sr. Each crystal has a 10 cm thick lead collimator of 7 cm internal diameter. The CACTUS array has a total efficiency of 14.1% and energy resolution of 7% FWHM for a 1332 keV transition. 2 mm copper plates are used as X-ray suppressors at the front of each crystal and 3 mm thick lead

shields are used between the NaI(Tl) detectors to avoid cross talk.

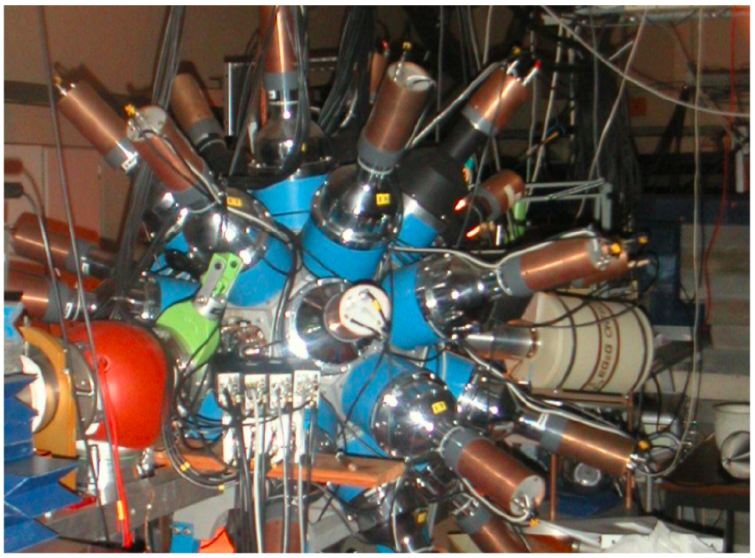

Figure 4.5: CACTUS multi-detecor setup [61].

4.2 Electronics

A Caen SY2527 Universal Multichannel Power Supply System is used to power the photo-multiplier tubes of the NaI(Tl) detectors. This system includes a CPU and front panel section to monitor and change the high voltage of each detector remotely. The photo-multiplier tubes of the NaI(Tl) detectors are biased with a high voltage between 700-800 V. Mesytec MHV-4 modules were used to bias the silicon detectors, this module can also be monitored and voltage adjusted remotely. The ΔE detectors where biased to 30 V and to 350 V for the E detectors.

A schematic of the electronic setup is shown in 4.6. Signals from the E and ΔE detectors are split into two parts. One part (black) is connected to a spectroscopy amplifier and Analog to Digital Converter (ADC) awaiting the trigger signal to record energy information. The other part (red) is sent through time filter amplification (TFA) and leading edge discriminator (LED) modules to a coincidence module where a 200 ns wide window is used to determine if the signal identifies a true charged particle event as long as the E and ΔE signals overlap. The charged particle signal (green) is sent to another coincidence module to determine particle-γ coincidences.

Signals from the NaI(Tl) detectors are also split into two parts. One part (black) connects to a spectroscopy amplifier and ADC awaiting the trigger signal to record energy information. The other part is sent through TFA and LED modules where it is split again. One signal goes to a Time to Digital Converter (TDC) (black) awaiting the trigger signal to record time information, the other signal is connected to a coincidence module (green).

To ensure overlap of γ-rays with charged particle, the signal from the NaI(Tl) detectors are delayed. This enables the charged particle signal to be used as the start signal (black) in the TDC module and the NaI(Tl) signal to provide the stop signal. The charged particle and the NaI(Tl)(green) signals are sent to the coincidence module to determine particle-γ coincidences. Particle-γ events are then used as trigger signals (purple) for the ADC's and TDC's.

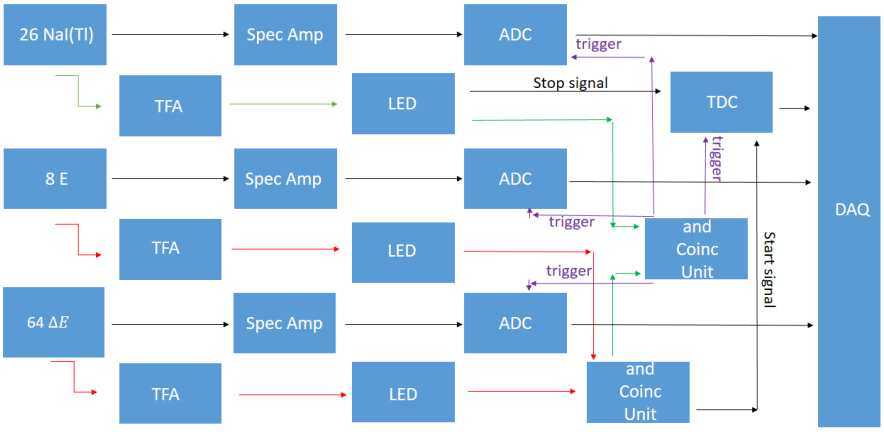

Figure 4.6: Schematic overview of the electronics used at Oslo Cyclotron laboratory [77].

Chapter 5

Calibration

5.1 SiRi array

The events recorded during the experiment need to be calibrated. The SiRi array is calibrated by fitting experimentally measured elastic peaks to calculated elastic peaks. The SiRi kinematic calculator [81] is used to compute the energies deposited by the charged particles. The calculator uses the Bethe-Bloch formula [82], which includes energy loss calculations that the charged particles may experience in the aluminum foil and target. Figure 5.1 shows the calculated energy deposition matrix that expected for the first strip of a detector with a scattering angle of $\theta_{lab} = 126^{\circ}$ and a deuteron beam energy of 12.5 MeV [81]. The vertical axis corresponds to the energy deposited in the thin front ΔE detector and the horizontal axis corresponds to the residual energy deposited in the back E detector. A similar plot has been generated for every strip.

Each line in figure 5.1 corresponds to energy deposited by the same type of charged particles. From top to bottom the corresponding charged particles are: ^{4}He, tritons, deuterons and protons. Each charged particle has a different mass and amount of protons, which makes the energy deposited while traveling though the ΔE and E detectors different.

By measuring two or more experimental elastic peaks that are several MeV apart from each other along the E and ΔE axis and fitting these values to the corresponding computed elastic peak we can calibrate the experimental data. For calibration purposes a 3.5 $\frac{mg}{cm^2}$ thick ^{28}Si target was also exposed to the deuteron beam. The ^{181}Ta(d,d')^{181}Ta elastic peak and ^{28}Si(d,p)^{29}Si ground state peak was used to calibrate the Ta data and the ^{28}Si(d,d')^{28}Si elastic peaks, the ^{28}Si(d,d')^{28}Si excited state and the ^{28}Si(d,p)^{29}Si ground state peak was used for the Si data calibration. This was repeated for every strip of the SiRi array. The ^{181}Ta(d,d')^{181}Ta and ^{28}Si(d,p)^{29}Si calibrated ΔE-E matrices

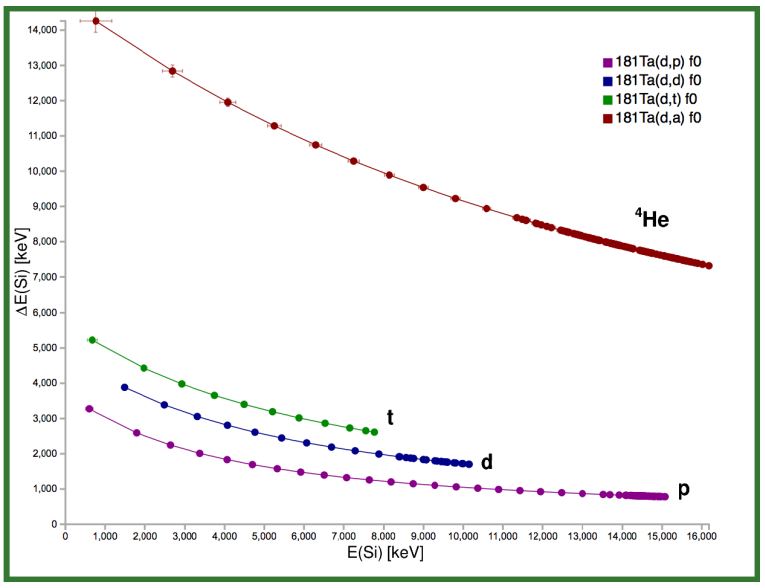

Figure 5.1: The calculated ΔE−E plot obtained with the calculator SiRi.

are shown in figure 5.2 and figure 5.3 respectively.

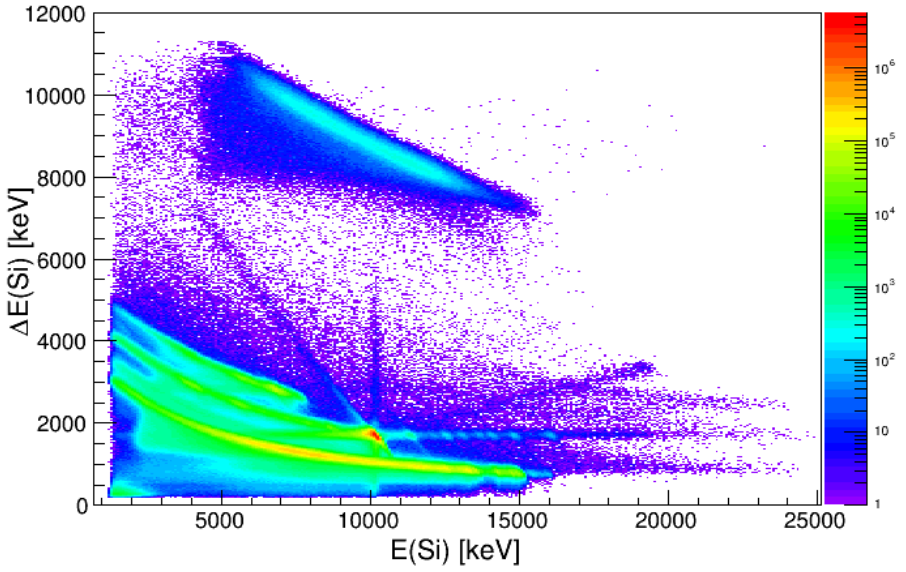

Figure 5.2: Experimentally measured ΔE−E matrix of ^{181}Ta(d,x)^{181}Ta without a time gate.

In Figure 5.2 some suspected random and pile up events (most notably the diagonal and straight lines) can be seen. The random events will be removed

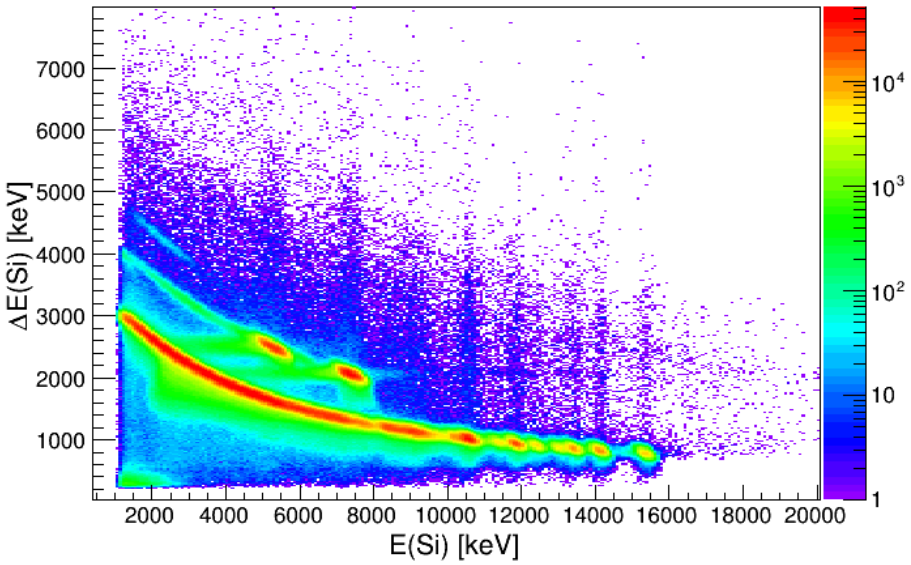

Figure 5.3: The E-ΔE matrix of ^{28}Si(d,x)^{29}Si that was used to calibrate the SiRi telescopes.

through the use of placing a time gate on the prompt peak, this is discussed in section 5.3. The four different hyperbolas corresponding to the different types of charged particles that were clearly visible in the calculated figure 5.1, namely p, d, t, ^{4}He, are visible in the experimental figure 5.2.

5.2 CACTUS array

After calibration of the silicon detectors, the excitation energy spectrum can be obtained. The measured energies of the protons where converted into excitation energy using kinematics and Q-values of the reactions. To keep only the ^{182}Ta events a banana gate is set on the ^{181}Ta(d,p)^{182}Ta reaction. Putting a gate on the ^{181}Ta(d,d')^{181}Ta reaction will only keep the ^{181}Ta events. The effect of the banana gate on the ^{181}Ta(d,p)^{182}Ta reaction is shown in figure 5.4. Figure 5.5 shows the excitation energy spectrum of ^{182}Ta and figure 5.6 shows the excitation energy spectrum of ^{29}Si.

By putting a gate on individual particle peaks in the excitation energy spectrum the γ-rays can be calibrated. The excitation energy spectrum of ^{29}Si was used for the γ-ray calibration. The states that were gated on is shown in table 5.1, for example by gating on the 3067 keV state the 1273 and 1793 keV γ-rays decaying from this state can be seen in the γ-ray spectrum.

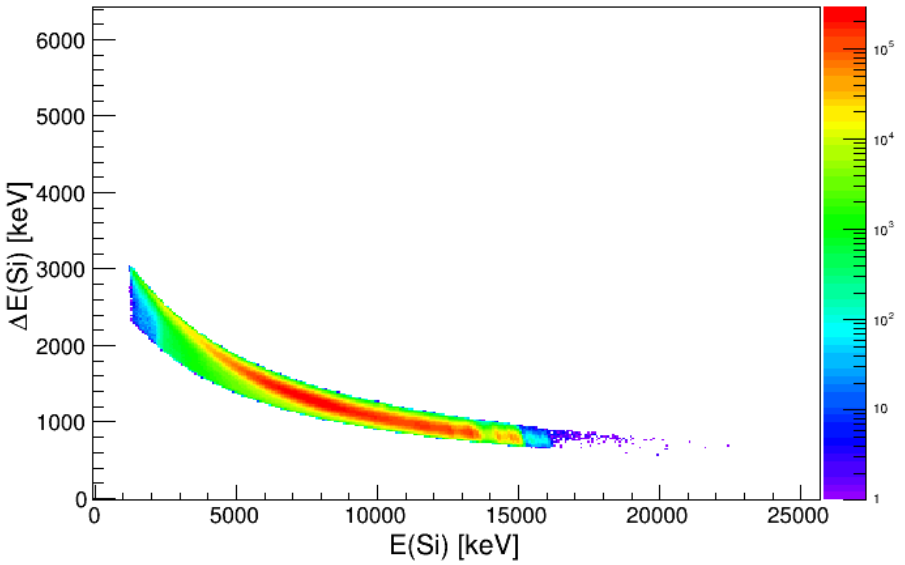

Figure 5.4: Gating on the ^{181}Ta(d,p)^{182}Ta reaction.

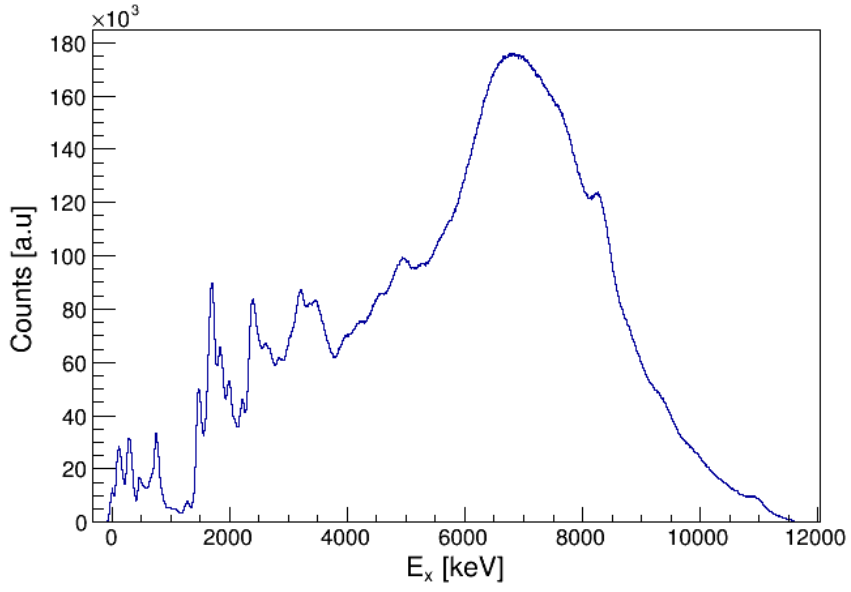

Figure 5.5: The excitation energy spectrum of ^{182}Ta.

The experimental values of the γ-ray photo peaks are fitted to the evaluated database values obtained from the national nuclear data center (NNDC) [83] to calibrate the γ-ray energies. In Figure 5.7 the calibrated γ-ray spectrum of ^{29}Si is shown. The centroids agree with NNDC within a standard deviation of $\approx$ 20 keV.

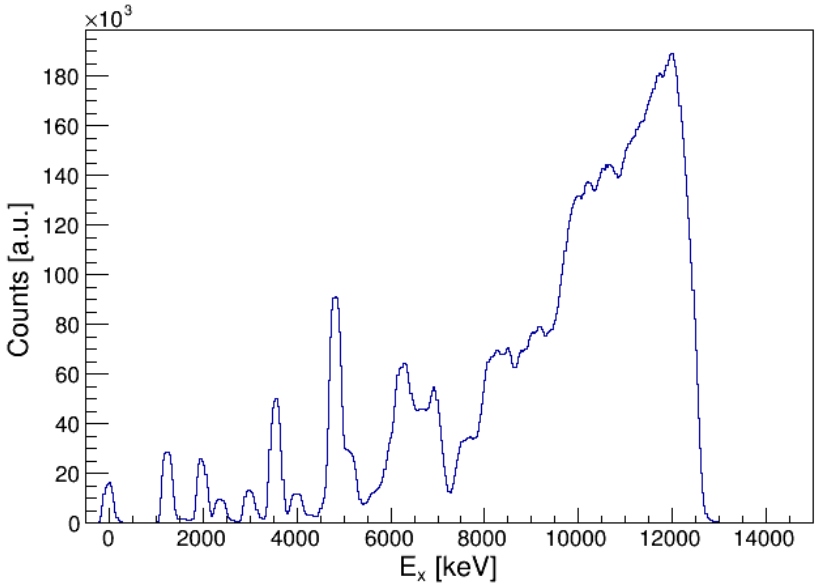

Figure 5.6: The calibrated excitation energy spectrum of ^{29}Si.

Table 5.1: The states that were gated on and the corresponding γ-ray photo peaks that was used to calibrate the CACTUS detector array.

State (keV)	γ-ray photo peaks (keV)
1273	1273
2028	2028
3067	1273, 1793
3623	1595, 2028
4079	1273, 2806
4895, 4933	1273, 3621, 4933

5.3 Time calibration

For the time calibration, the centroid of the prompt peaks are arbitrarily set to channel 200. This defines the time for the NaI(Tl) detectors. The calibrated time-energy matrix is shown in figure 5.8 with time on the vertical axis and energy deposited into the NaI(Tl) detectors on the horizontal axis. At low energies a "tail" can be seen in the prompt time peak. This "tail" is known as the walk effect.

The low energy γ-rays have a shorter rise time compared to higher energy γ-rays. Since the leading edge discrimination (LED) threshold is constant,

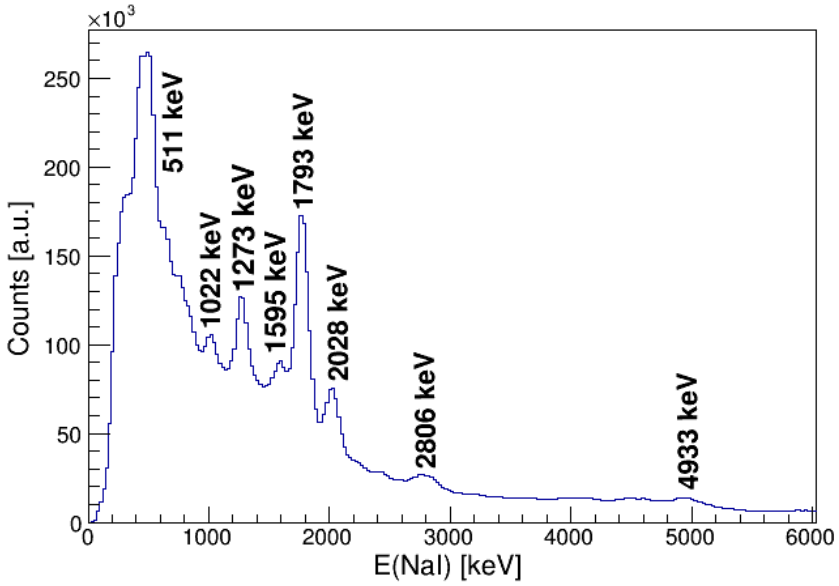

Figure 5.7: The calibrated γ-ray spectrum of ^{29}Si showing the 1273, 1595, 1793, 2028 and 4933 keV γ-rays transitions.

the lower energy γ-rays are recorded later than the high energy γ-rays. This produces a tail in the time distribution. It was corrected by using a fitting function of the form shown in equation 5.1.

$$t(x) = a + \frac{b}{x + c} + dx + 200 \tag{5.1}$$

where $t(x)$ are channels corresponding to corrected time and x are channels corresponding to γ-ray energy. The fitting parameters a, b, c and d are then used to align the time peak at channel 200. After correcting for the walk effect, the time-energy matrix has a straight prompt peak corresponding to the correlated events, this is shown in figure 5.9. The structures in the matrix are due to the other beam particle pulses due to the cyclotron frequency. These lines can be seen as oscillations in the projection of figure 5.10 where the time between events are shown.

Figure 5.10 shows the projection of the time between events following walk correction. The peak around channel 200 shows the correlated events. A correlated time gate is placed at channels $185 - 215$ to exclude most uncorrelated events. The random and background events that fall inside channels $185 - 215$ still need to be removed. To do this, a background gate is placed at channels $270 - 300$. The events in the background gate is subtracted from the events in the correlated time gate, effectively removing the background from the correlated events. This means that only the correlated events that fall in

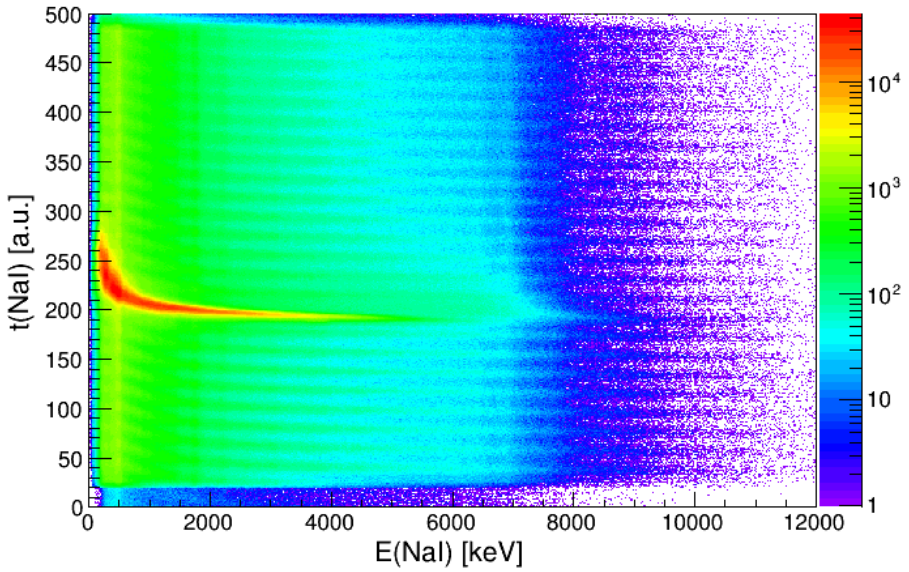

Figure 5.8: Time-energy matrix without walk correction. Time is on the y-axis and energy deposited into the NaI(Tl) detectors is on the x-axis.

the correlated time gate will be analyzed. Using these gates to remove the random and background events of Figure 5.2 a new E-ΔE matrix is created, this matrix is shown in Figure 5.11.

Comparing figure 5.2 with figure 5.11, most of the random events were eliminated. The remaining events could be due to particles going through the ΔE detector and undergoing nuclear reactions in the E detector, therefore the residual energy is missing the Q-value and γ-rays emanating thereof. This concludes the calibration procedures, the NLD and PSF can now be extracted from the calibrated data.

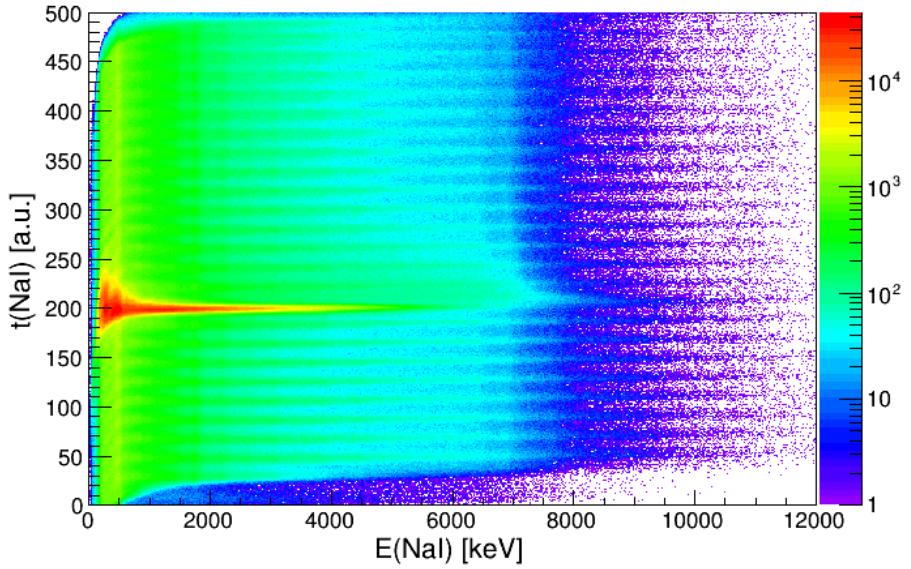

Figure 5.9: Time-energy matrix with walk correction. Time is on the y-axis and energy deposited into the NaI(Tl) detectors is on the x-axis.

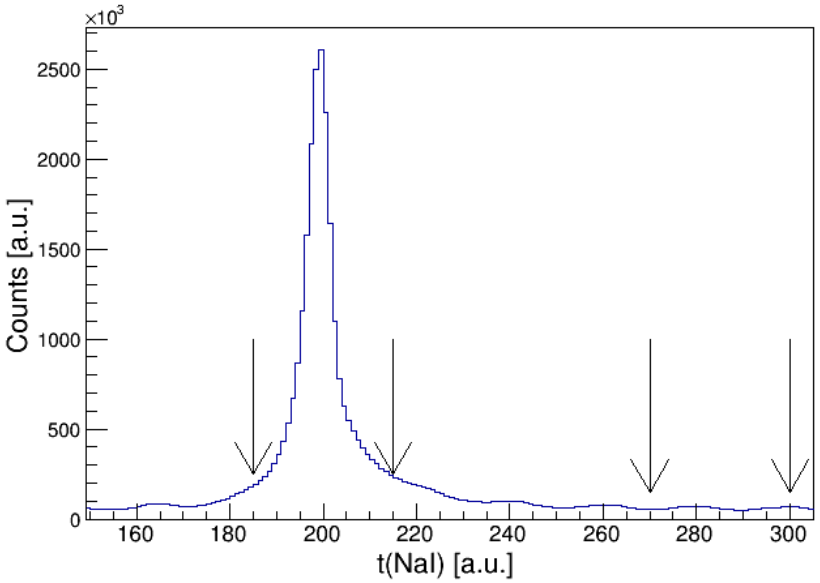

Figure 5.10: Time between γ-particle events after walk correction.

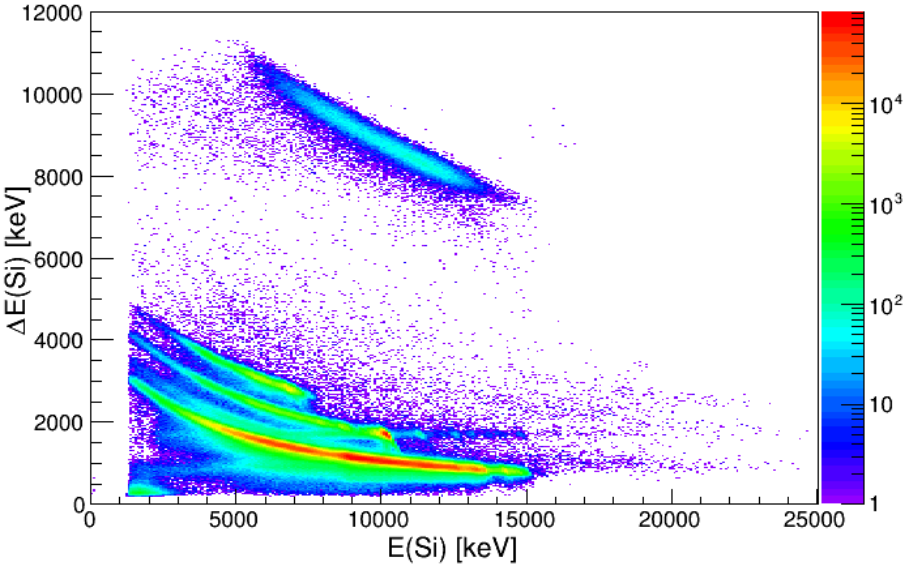

Figure 5.11: This is the E-ΔE graph with the time gate to remove most uncorrelated events.

Chapter 6

Results

6.1 Unfolding and Extracting

Now that all the experimental data have been calibrated and all the gates are set, unfolding and extraction can begin. The extraction procedure for ^{182}Ta and ^{181}Ta is the same, the only difference being the banana gate. For ^{182}Ta the gate is set on the protons from the (d, p) reaction and for ^{181}Ta the gate is set on the deuterons of the (d, d') reaction. The ^{181}Ta data does not reach the neutron separation energy of 7.5 MeV due to reaction kinematics, adding extra uncertainties to the extraction of the NLD and PSF. The excitation energy, γ energy matrix for ^{182}Ta and ^{181}Ta is shown in figures 6.1 and 6.2 respectively.

Two triangular shapes can be seen in figure 6.1. There cannot be a γ-ray with a higher energy than the excitation energy so there is a 45° line originating at the ground states. The 45° line is an indication of an accurate calibration. At an excitation energy of 6.06 MeV the γ-ray energy drops suddenly for ^{182}Ta. This is the neutron separation energy. The neutron separation energy is the energy where the nucleus has enough energy to emit either a γ-ray or a neutron, depending on the spin of the nuclear state and angular momentum barrier effects. When a neutron is emitted the nucleus is no longer ^{182}Ta, but rather ^{181}Ta. Events below 6.06 MeV excitation energy belong to ^{182}Ta and events above 6.06 MeV excitation energy belong predominantly to ^{181}Ta.

Two blobs are also observed around the excitation energy of 8 to 9 MeV in figure 6.1. These are due to the ^{12}C contaminant in the target which undergoes the reaction ^{12}C(d,p)^{13}C. The resultant ^{13}C emits γ-rays of energies 3854 keV and 3089 keV which can be observed as two blobs. At high γ energies the statistics is generally lower because the detector efficiency is lower. At low excitation energies there are gaps in the energy spectrum. This is due to the excitation energy gap between 0.771-1.308 MeV [84].

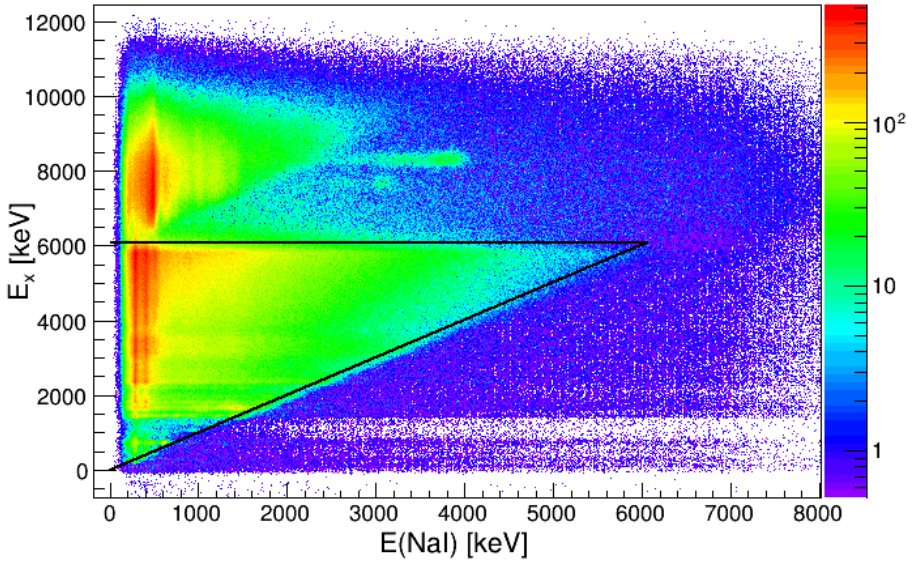

Figure 6.1: The excitation energy versus γ-ray energy matrix of ^{182}Ta before the Oslo method implementation.

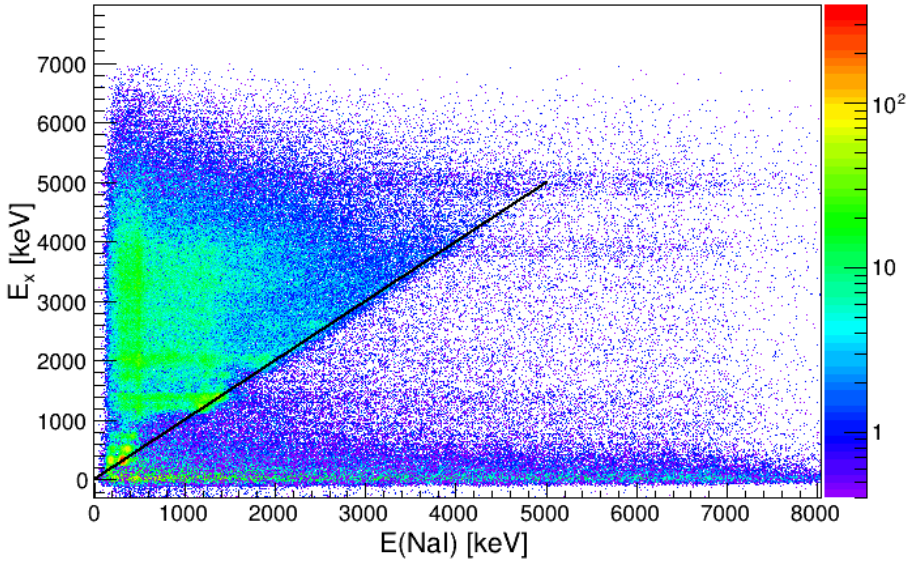

Figure 6.2: The excitation energy versus γ-energy matrix of ^{181}Ta before the Oslo method implementation.

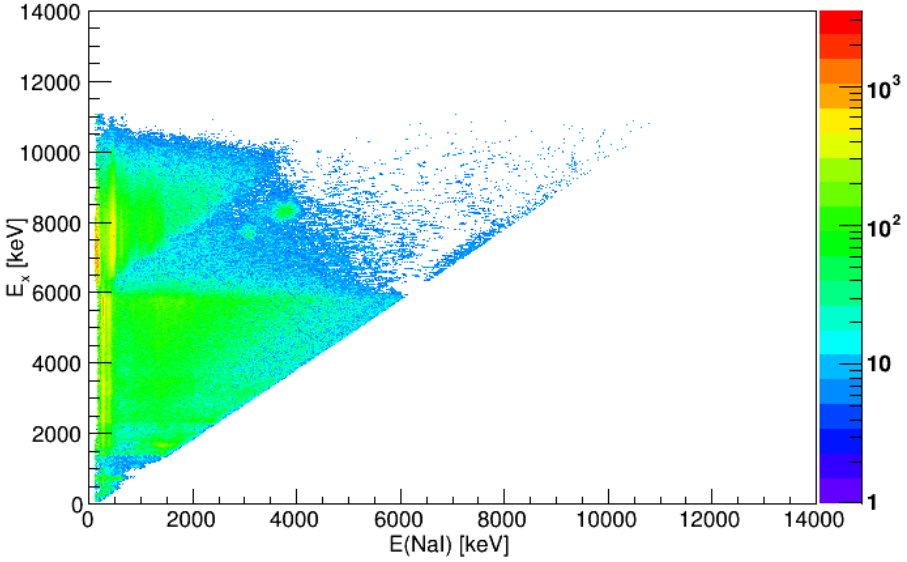

Figure 6.3: The unfolded matrix of ^{182}Ta.

From figure 6.1 the unfolded matrix is calculated using the unfolding method explained in section 3.1.2. During the unfolding a 45° cut is implemented to discard random events with $E_\gamma > E_x$. Various background and escape events are also removed and the unfolded matrix, for ^{182}Ta is shown in figure 6.3.

From the unfolded matrix the first generation E_x vs E_γ matrix is extracted using the first generation method explained in section 3.2. During this method another cut is placed above S_n ($E_x = 6.4$ MeV for ^{182}Ta), excluding the ^{13}C contaminants and all events from ^{181}Ta. The first generation matrices are shown in figure 6.4 for ^{182}Ta and in figure 6.5 for ^{181}Ta.

For the NLD and PSF extraction procedure upper and lower bounds in the excitation energy and a lower bound for the γ-energy are set. The upper excitation energy bound of the excitation energy is set at the S_n-energy resolution, which is 5.9 MeV for ^{182}Ta. For ^{181}Ta the upper excitation energy bound is set to 3.8 MeV due to low statistics. Below 2.5 MeV excitation energy some discrete states can still be observed. The lower band is set at $E_x = 2.5$ MeV for both ^{182}Ta and ^{181}Ta to ensure that only events from the quasi-continuum region are used and that Brink's hypothesis is valid. Due to the systematics some over and under subtraction are observed as vertical lines at low γ energies. The lower bound for the γ-energy is set at 950 keV for ^{182}Ta and 800 keV for ^{181}Ta.

The experimental events of ^{182}Ta, $P(E_x, E_\gamma)$, which are left after all the bounds

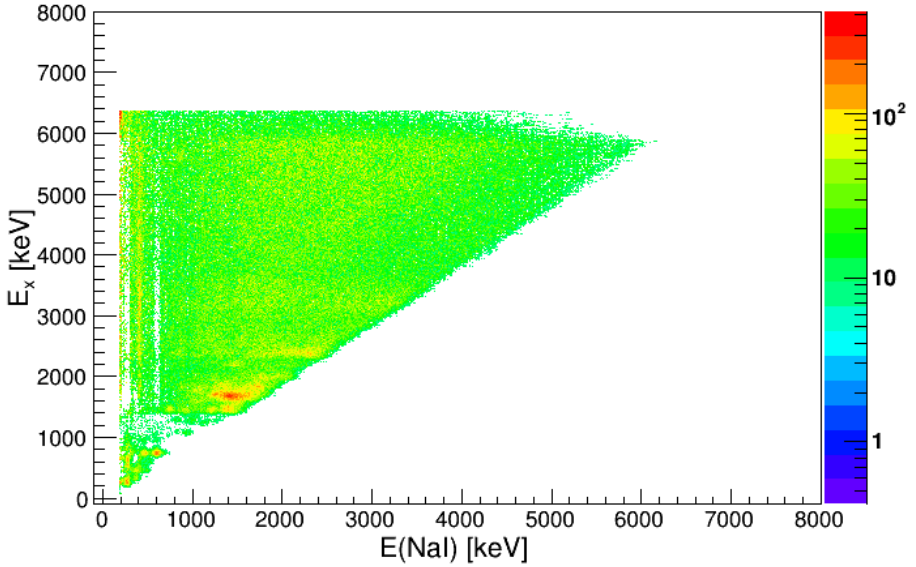

Figure 6.4: The first generation matrix of ^{182}Ta with background and random data removed.

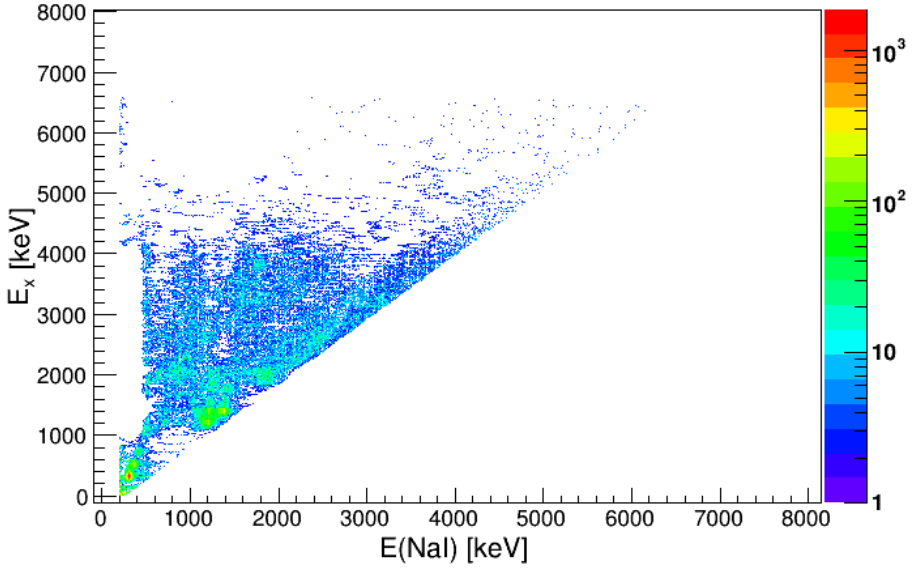

Figure 6.5: The first generation matrix of ^{181}Ta with background and random data removed.

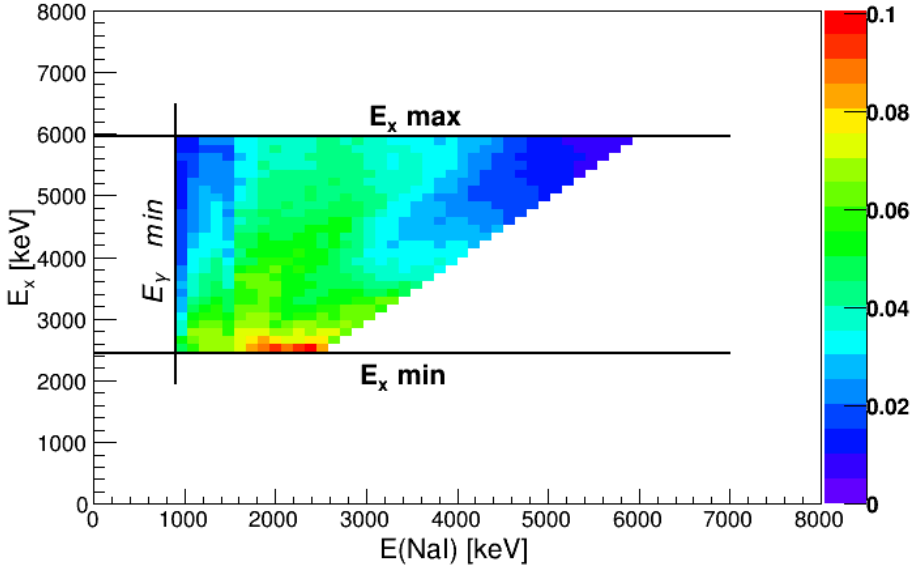

Figure 6.6: Experimental first generation matrix, $P(E_x, E_\gamma)$, of ^{182}Ta.

have been set are shown in figure 6.6. The corresponding theoretical events, $P_{th}(E_x, E_\gamma)$, are shown in figure 6.7. $P(E_x, E_\gamma)$ and $P_{th}(E_x, E_\gamma)$ are used in the χ^2 minimization given by equation 3.22.

In order to test if the extraction was accurate and also to evaluate the statistical and systematical errors made during the extraction, $P(E_x, E_\gamma)$ is compared to $P_{th}(E_x, E_\gamma)$. Experimental γ energies are compared to theoretically calculated γ energies as shown in figure 6.8. The data points are the experimental data and the line is the theoretical data. The theoretical data lie within the error bars of the experimental data, making the extraction accurate.

6.2 Photon strength function and nuclear level density

From Figure 6.4 the photon strength function $f(E_\gamma)$ and nuclear level density $\rho(E_x)$ are extracted. The NLD normalization parameters, D_0 and $< \Gamma_\gamma(S_n) >$ are averaged between references [66] and [85], see table 6.1 for values.

The nuclear level densities for ^{182}Ta and ^{181}Ta are shown in figures 6.9 and 6.10 respectively. The black squares are the experimental $\rho(E_x)$, the solid black line indicates the known levels obtained from [83], the empty square is calculated from neutron resonance data and the dashed line is the interpolated nuclear

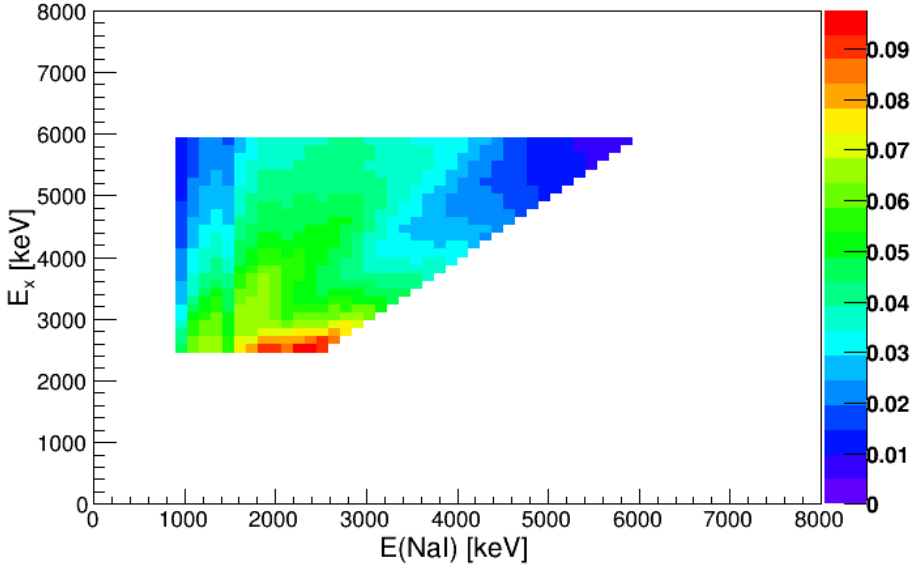

Figure 6.7: Theoretical first generation matrix, $P_{th}(E_x, E_\gamma)$, of ^{182}Ta.

Table 6.1: The parameters, D_0 and $< \Gamma_\gamma(S_n) >$, used in normalizing the NLD are averaged between [66] and [85]. The parameters, σ and $\rho(S_n)$, used in normalizing the PSF are obtained from [15]. See text for details.

Nucleus	D_0 (eV)	$< \Gamma_\gamma(S_n) >$ (meV)	σ	$\rho(S_n)$
^{181}Ta	1.11 ± 0.2	51 ± 3.2	4.88 ± 0.5	$2.02 \times 10^6 \pm 3.02 \times 10^5$
^{182}Ta	4.185 ± 0.3	59 ± 3.7	4.96 ± 0.5	$1.46 \times 10^7 \pm 3.5 \times 10^6$

level density obtained from the constant temperature model. As explained in chapter 2, at low energies normalization is done with known level densities and at high energies normalization is performed with neutron resonance data. The arrows show the areas where the experimental NLD was normalized.

The NLD includes points with negative excitation energy, the reason for this is to account for the Si detector resolution. At high energies the detector resolution and efficiency deteriorates so when the nucleus decays from a high energy state to the ground state ($E_x = 0$), the emitted γ-ray appears to have $E_x < 0$, because the ground state peak is so broad. This effect is artificial, the γ-ray goes to $E_x = 0$. By taking these negative events into account some statistics is recovered. The data points for the NLD of ^{182}Ta and ^{181}Ta are given in tables A.1 and A.2 respectively.

At $E_x = 24A^{-0.5}$ MeV [86] the pair breaking can be observed as a slight increase in the NLD. Above the breaking point the temperature remains constant since all available energy will be used to break nucleon cooper pairs, which can

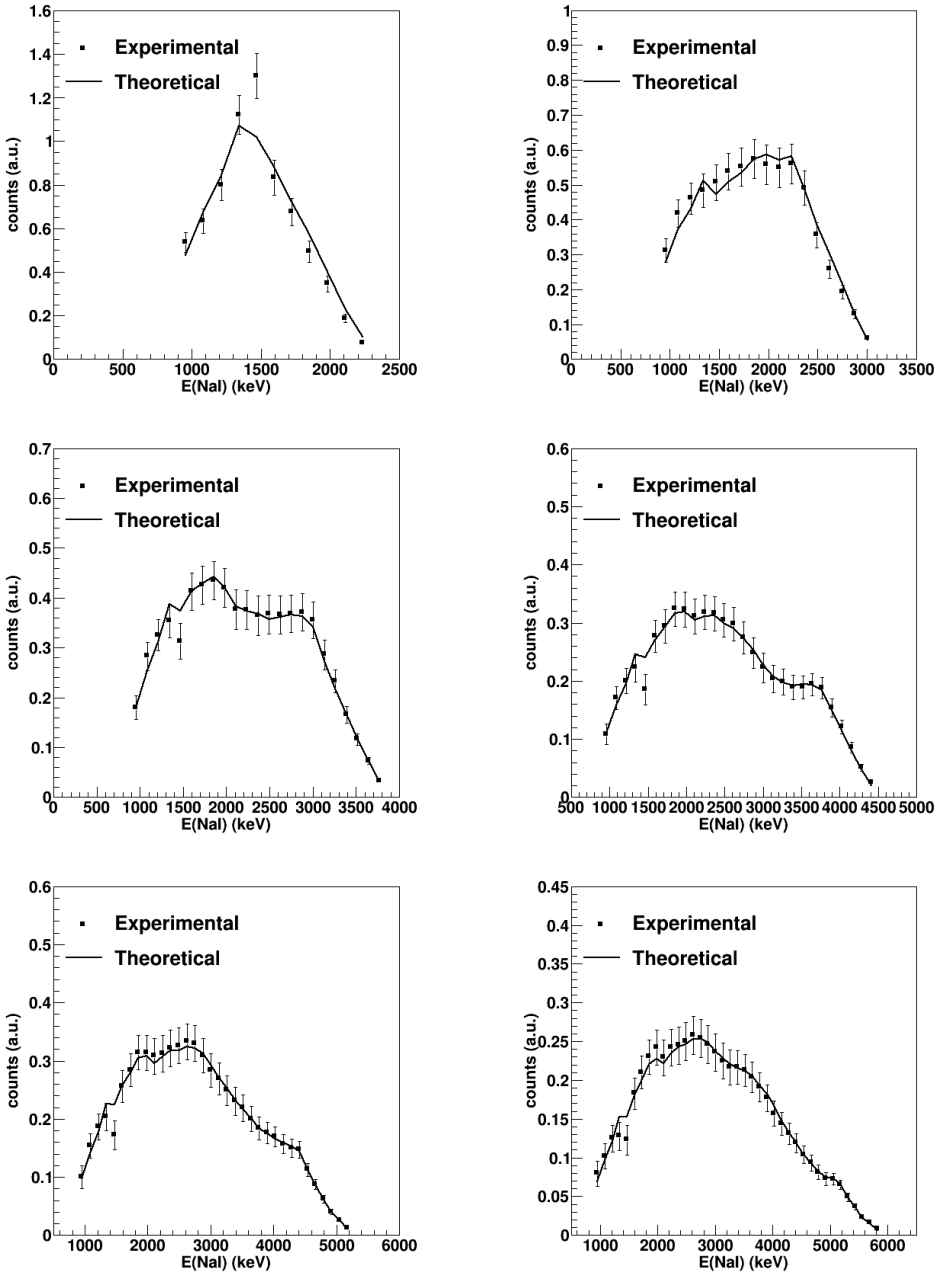

Figure 6.8: The systematical and statistical errors made during the extraction procedure of ^{182}Ta. The points are the experimental data and the line is the theoretical calculations.

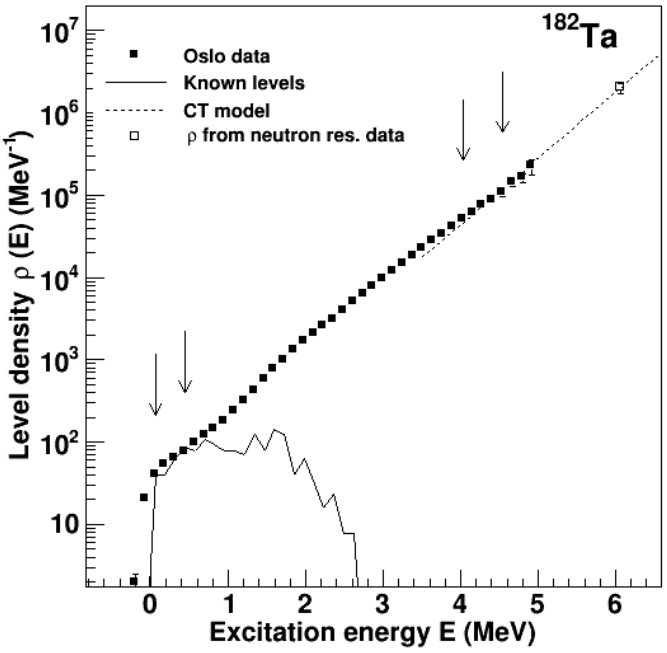

Figure 6.9: The nuclear level density of ^{182}Ta.

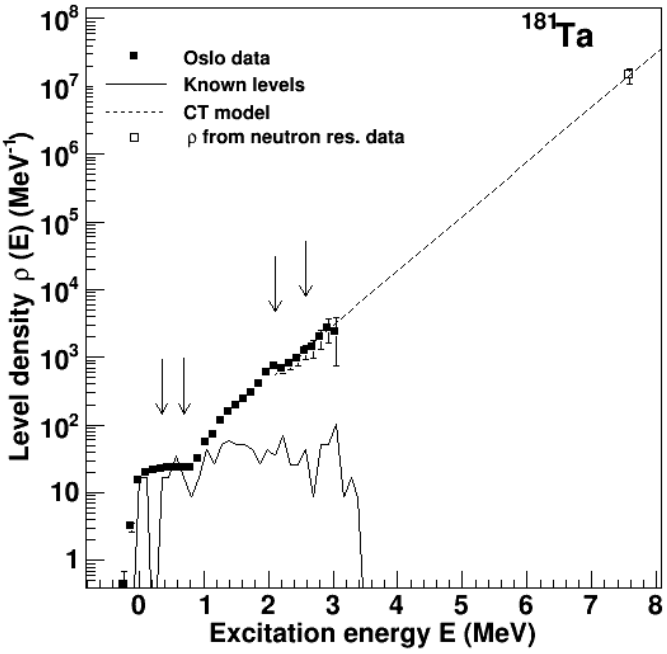

Figure 6.10: The nuclear level density of ^{181}Ta.

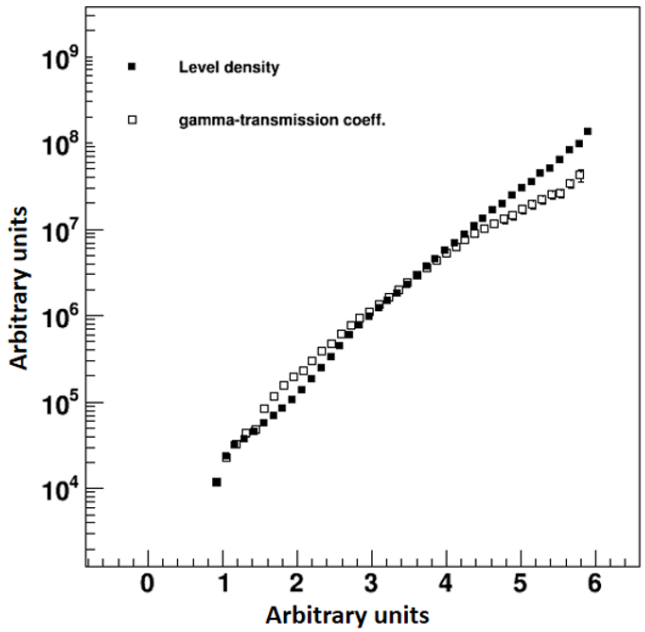

Figure 6.11: The nuclear level density plotted with the gamma transmission coefficient of ^{182}Ta to compare their slopes.

be seen as a first order phase transition. For ^{182}Ta the breaking point is at 1.778 MeV and for ^{181}Ta it is at 1.783 MeV. This is below 2 MeV (not in the quasi-continuum), which is why a constant temperature model can be used above it.

The slope of $\rho(E_x)$ and the gamma transmission coefficient should be the same. In figure 6.11 the $\rho(E_x)$ and gamma transmission coefficient are plotted together, note that the NLD has been multiplied by a constant factor to compare the two figures slopes. It can be seen that the slope of the nuclear level density and gamma transmission coefficient are very similar, suggesting that the slope α is correct.

The normalization parameters for the PSF, σ and $\rho(S_n)$, are calculated from the back-shifted Fermi gas model with parameters taken from [15], see Table 6.1 for values. The PSF for ^{182}Ta with excitation energies between 2.5 MeV and 6 MeV is shown in figure 6.12 and for ^{181}Ta with excitation energies between 2.5 MeV and 4 MeV is shown in figure 6.13. The data points for the PSF of ^{182}Ta and ^{181}Ta are given in tables A.3 and A.4 respectively.

The strength functions look quite similar with no obvious resonances observed. The bumps at low energies, in particular for ^{181}Ta, are most likely due to statistics and not resonances. For ^{182}Ta the error bars are relatively small

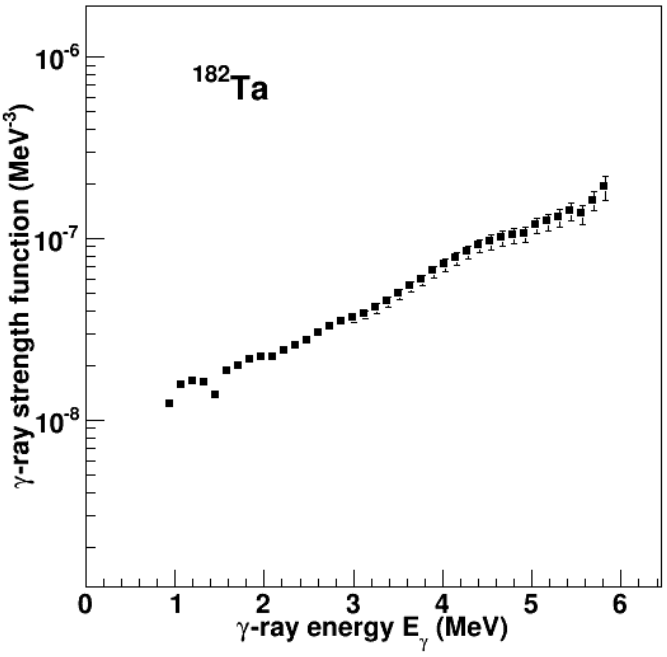

Figure 6.12: The photon strength function of ^{182}Ta.

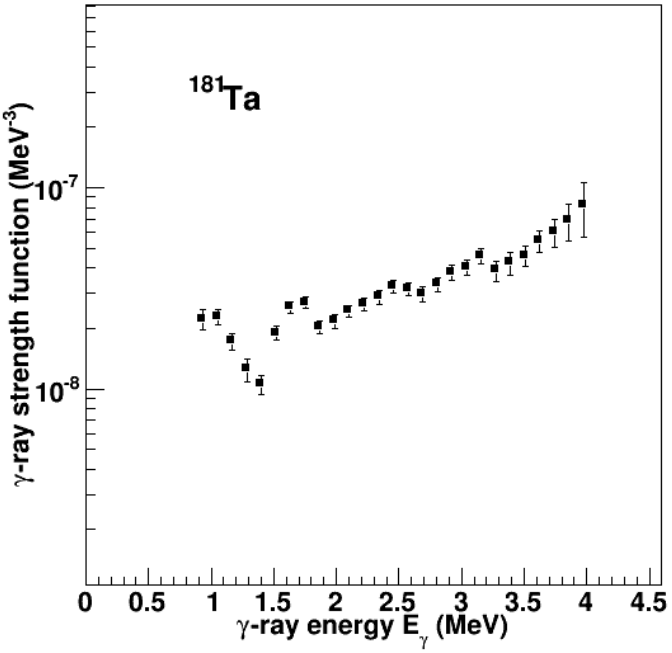

Figure 6.13: The photon strength function of ^{181}Ta.

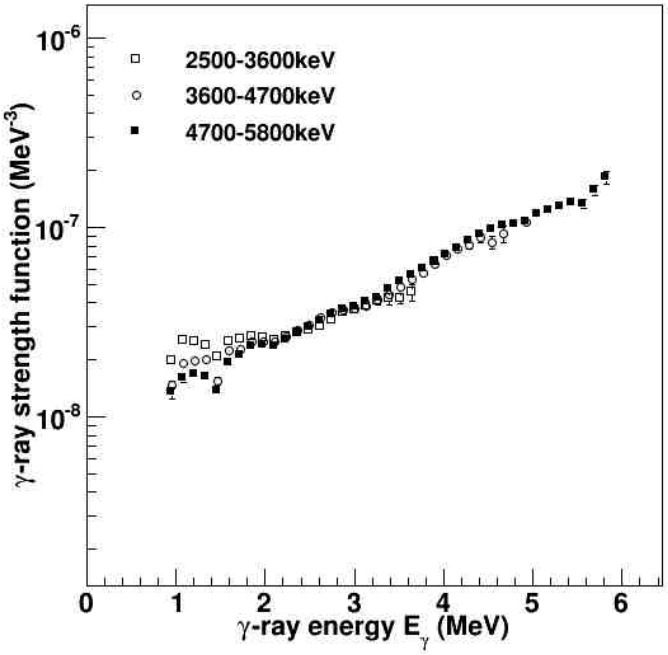

Figure 6.14: Different energy cuts for the photon strength function of ^{182}Ta.

making it unlikely that well localized resonances are present. For ^{181}Ta the error bars are larger, but still small enough to be sensitive to well localized resonances. For the Brink hypothesis to be valid strength functions from different excitation regions of the same nucleus should be similar. In figure 6.14 the strength function of ^{182}Ta for excitation regions 2500-3600 keV, 3600-4700 keV and 4700-5800 keV are plotted. At low γ-ray energy ($E_\gamma < 2$ MeV) some variations are observed but these are most likely due to low energy statistical effects. It can be concluded that the strength functions are similar enough for different excitation energy regions validating Brink's hypothesis.

Figure 6.15 shows the strength functions for ^{181}Ta and ^{182}Ta plotted together. They have the same slope and similar strength which is consistent with observations in other systems also. In figure 6.16 the PSF for ^{181}Ta from two reactions, ^{181}Ta(^{3}He,^{3}He')^{181}Ta [87] and ^{181}Ta(d,d')^{181}Ta, from the present work, are compared. The two PSF's are similar and overlap, not only providing info on the reaction independence of the PSF but also giving confidence to the present analysis.

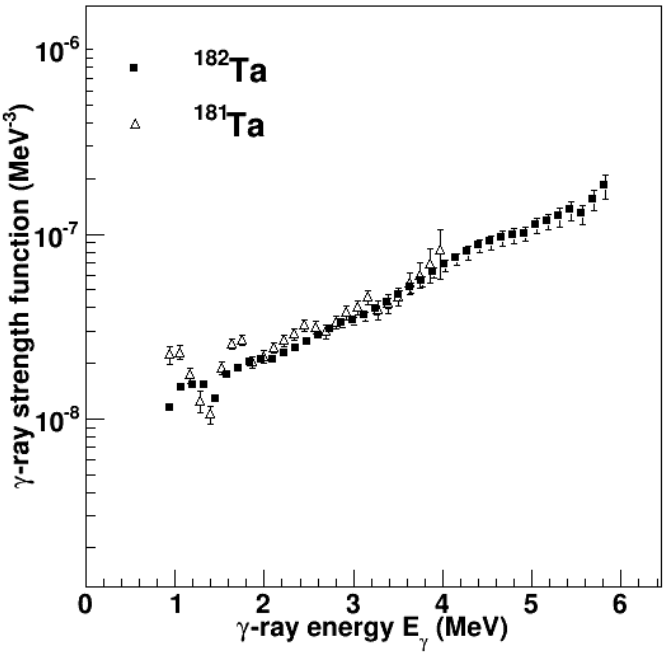

Figure 6.15: The photon strength function of ^{181}Ta and ^{182}Ta.

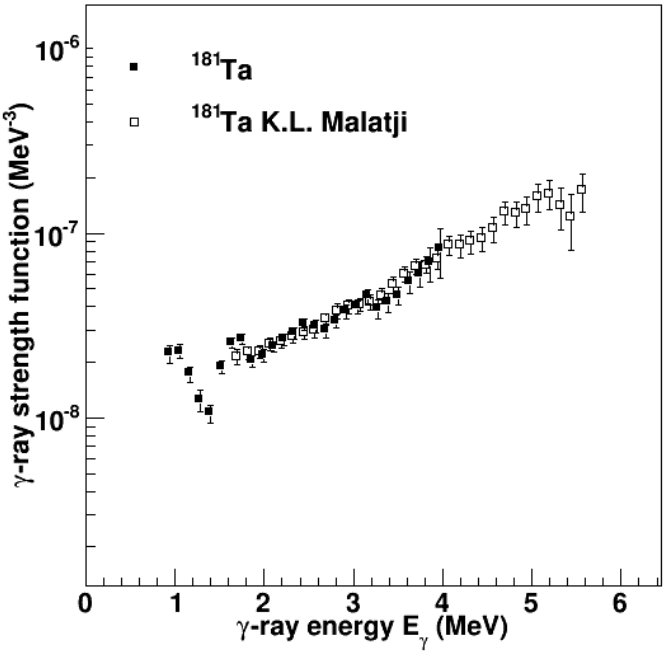

Figure 6.16: The photon strength function of ^{181}Ta extracted using two different reactions, ^{181}Ta(^{3}He,^{3}He')^{181}Ta [87] and ^{181}Ta(d,d')^{181}Ta.

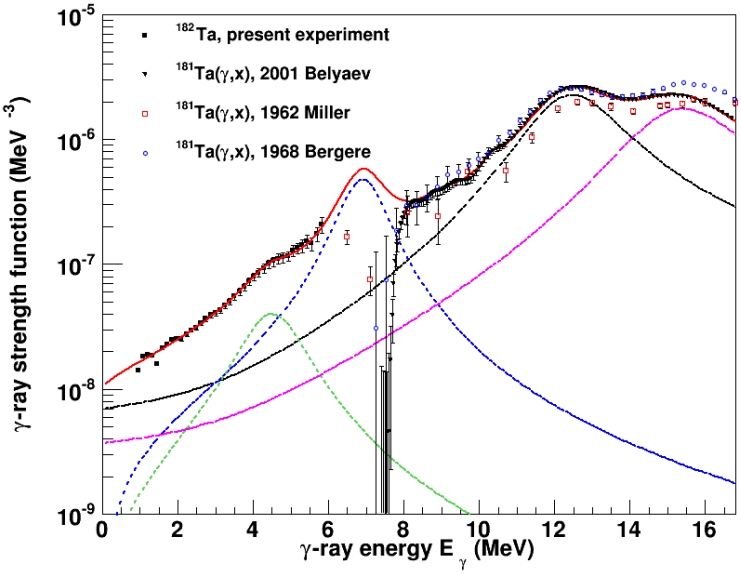

Figure 6.17: ^{182}Ta resonance fits, see text for details.

6.3 Resonance fitting

Possible resonances of ^{182}Ta are fitted with Lorentzian functions in figure 6.17. The green dotted line is a resonance added so that the total fit matches the experimental data, this resonance is fitted with a standard Lorentzian function. The blue dotted line is due to contributions from the overlapping pygmy and spin-flip resonances, this resonance is also fitted with a standard Lorentzian function. The black and purple dotted lines are the GEDR, which is split due to deformation, is fitted with an enhanced generalized Lorentzian function. The black squares in figure 6.17 are the current experimental results. The black triangles, blue and red squares are cross sections converted to PSF from [88], [89] and [90] using equation 3.35. The red line is the sum of all Lorentzian funtions that form a total fit to the data.

The information on the Lorentzian parameters that were used to fit the resonance is given in table 6.2. The GEDR parameters are modified from [66] and the other resonances' parameters σ and Γ_0, for which no theoretical data is available, is adjusted until the total fit match the experimental data. Although the neutron separation energy is at 6.06 MeV, the resonance at 7.05 MeV was identified in the photo absorption cross section for ^{181}Ta where an increase in the cross section at 7.05 MeV was found [91] as shown in figure 6.18. Note that reference [91] only gives information on the centroid (parameter E_0) of this resonance.

Table 6.2: The resonance parameters used in the Lorentzian functions of ^{182}Ta for figure 6.17. The GEDR parameters are modified from [66], see text for more details.

Resonances	E_0 (MeV)	σ (mb)	Γ_0 (MeV)
Res1	4.6	1.6	1.8
Res2	7.05	42	1.33
GEDR1	12.46	345	2.62
GEDR2	15.9	450	3.4

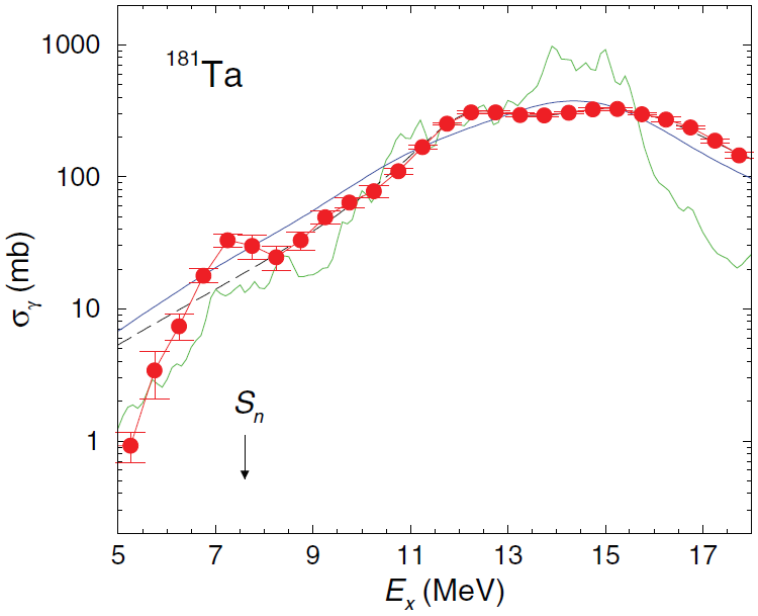

Figure 6.18: Cross section for ^{181}Ta taken from reference [91].

6.4 Talys Results

Using the Talys code [1] the NLD and PSF are used to calculate (n,γ) cross sections. Since the Oslo method only considers statistical and systematical uncertainties any uncertainties due to the parameters, D_0 and $< \Gamma(S_n) >$, need to be estimated. To take all possible errors into account an upper and lower error bands for the PSF are calculated with the uncertainties from references [66] and [85]. The upper error band is defined by:

$$D_0 = D_0 - \delta D_0$$
$$< \Gamma(S_n) > = < \Gamma(S_n) > + < \delta\Gamma(S_n) >$$

.

The lower error band is defined by:

Table 6.3: Table on the error band parameters based on values from reference [66] and [85]

upper band	$D_0 - \delta D_0$ (eV)	$\Gamma + \delta\Gamma$ (meV)
^{181}Ta	0.9	54.2
^{182}Ta	3.9	62.7
lower band	$D_0 + \delta D_0$	$\Gamma - \delta\Gamma$
^{181}Ta	1.3	47.8
^{182}Ta	4.5	55.3

$$D_0 = D_0 + \delta D_0$$

$$< \Gamma(S_n) > = < \Gamma(S_n) > - < \delta\Gamma(S_n) >$$

.
The calculated values are shown in table 6.3. The upper and lower error bands that were used to calculate the cross sections for ^{182}Ta and ^{181}Ta are shown in figures 6.19 and 6.20.

The PSF error bands are given as input for the Talys calculations. Talys uses a constant temperature model to calculate the NLD, however it is in good agreement with the experimental NLD from the present work, see figures 6.21 and 6.22. In figure 6.23 the error bands are plotted along with the Talys calculated error bands for ^{182}Ta. The Talys calculations fits in well for ^{182}Ta, but for ^{181}Ta an extra 20% uncertainty was added due to low statistics, this is shown in figure 6.24.

The Lorentz parameters used for the upper and lower error band resonances are shown in tables A.5 and A.6 for ^{182}Ta and ^{181}Ta respectively. The calculated cross sections for ^{182}Ta are shown in figure 6.25 and for ^{181}Ta they are shown in figure 6.26. The calculated cross section bands are also compared to (n,γ) experimental data from references [92, 93, 94]. There is a good agreement between the calculated cross sections using the PSF and NLD compared to cross sections measured from other experimental work, therefore the NLD and PSF can be used to calculate accurate (n,γ) cross sections.

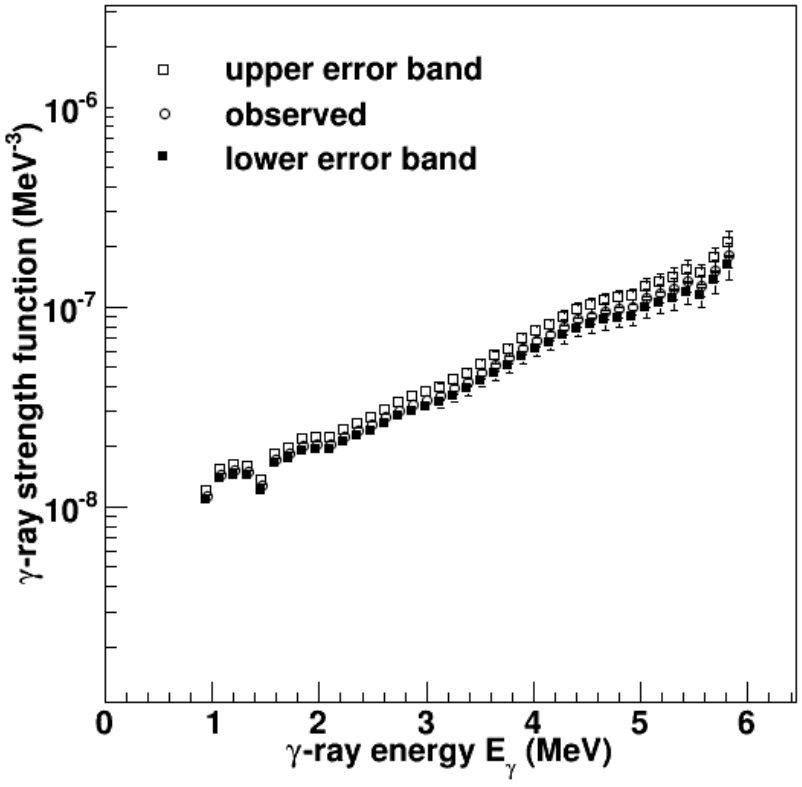

Figure 6.19: ^{182}Ta photon strength function with the upper and lower error bands.

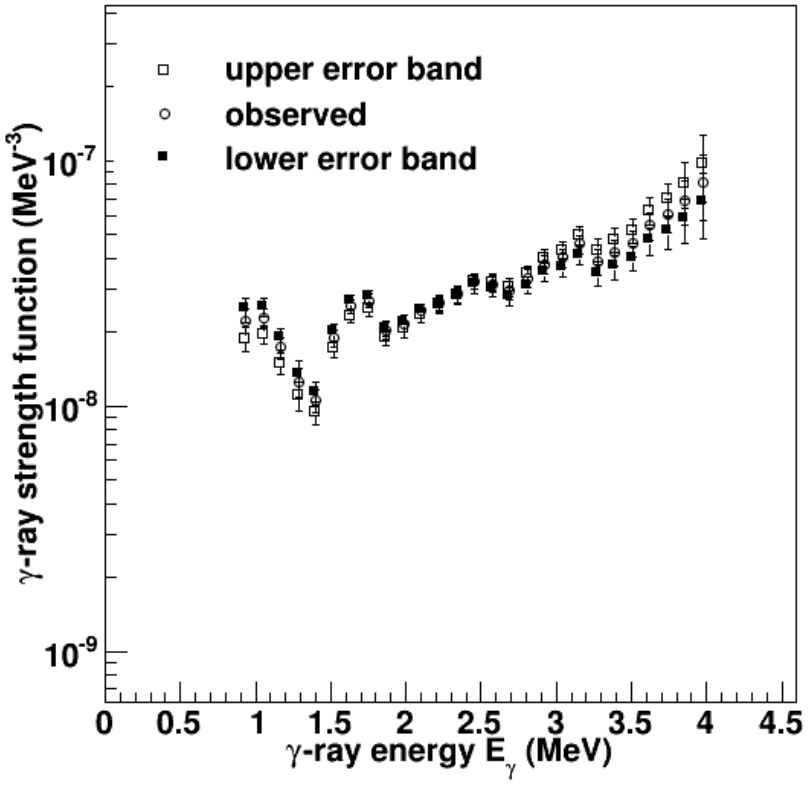

Figure 6.20: ^{181}Ta photon strength function with the upper and lower error bands.

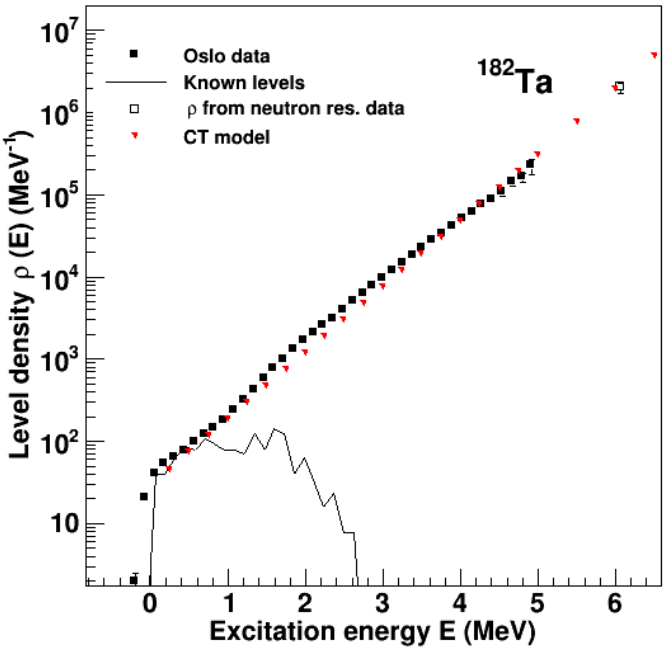

Figure 6.21: ^{182}Ta NLD compared to the constant temperature (CT) model used in Talys calculations.

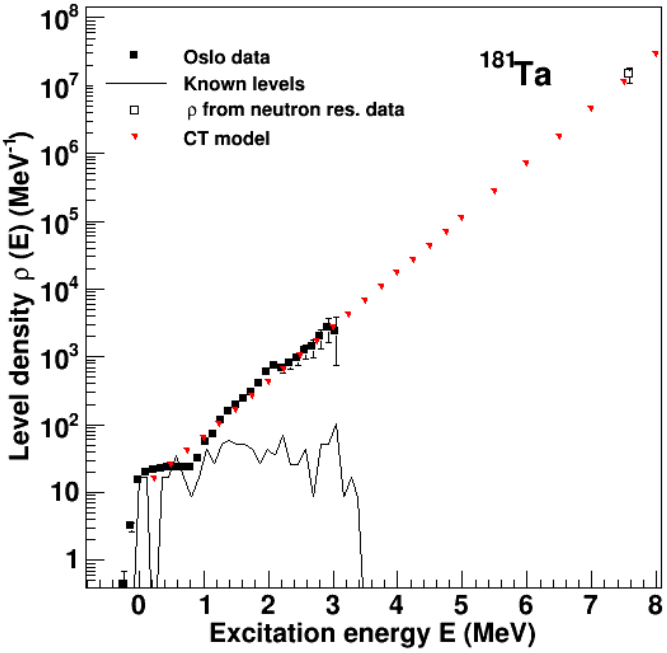

Figure 6.22: ^{181}Ta NLD compared to the constant temperature (CT) model used in Talys calculations.

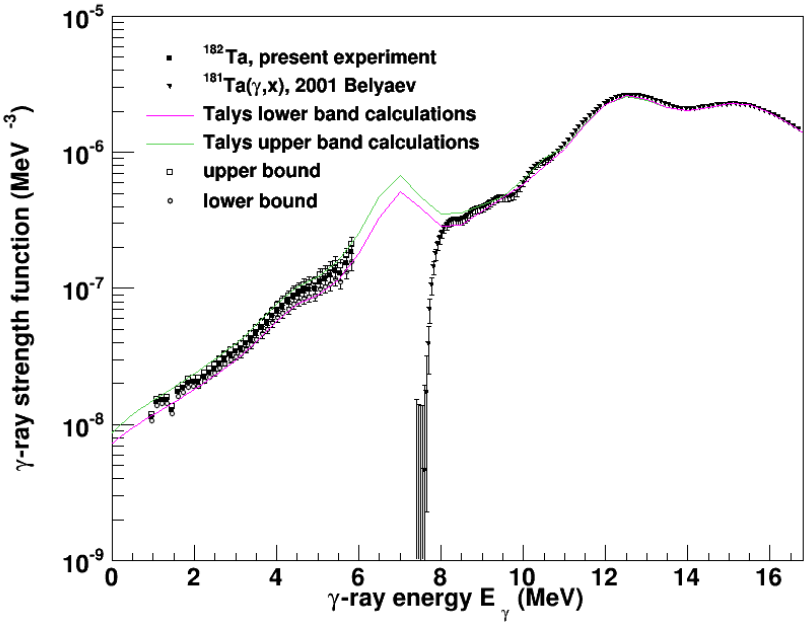

Figure 6.23: ^{182}Ta resonance and Talys calculated PSF band.

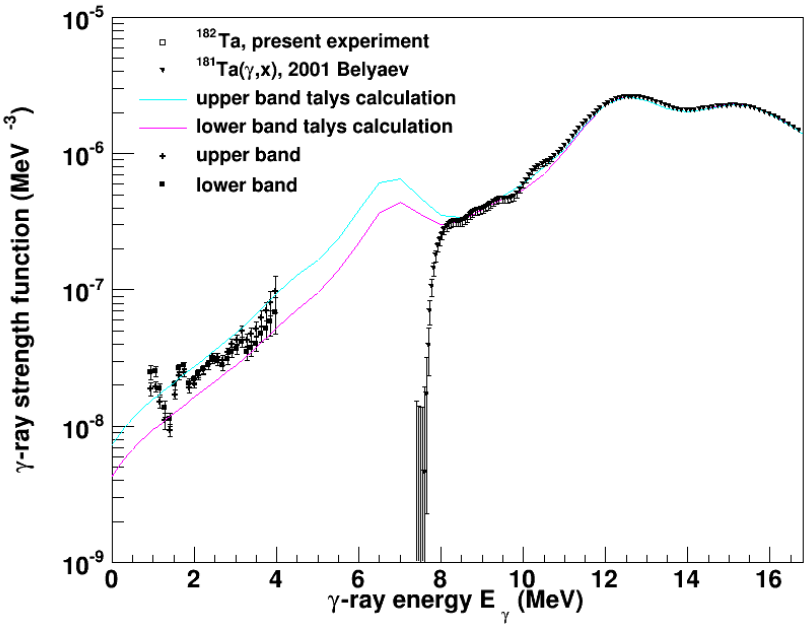

Figure 6.24: ^{181}Ta resonance and Talys calculated PSF band.

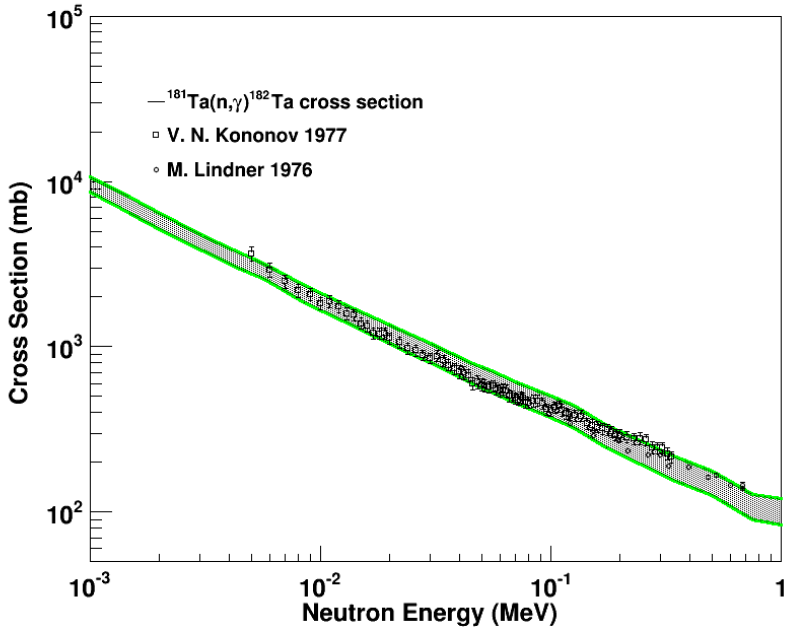

Figure 6.25: ^{182}Ta cross sections. The green band represents the cross sections calculated from the NLD and PSF. The open squares are experimentally measured cross sections from references [92, 93].

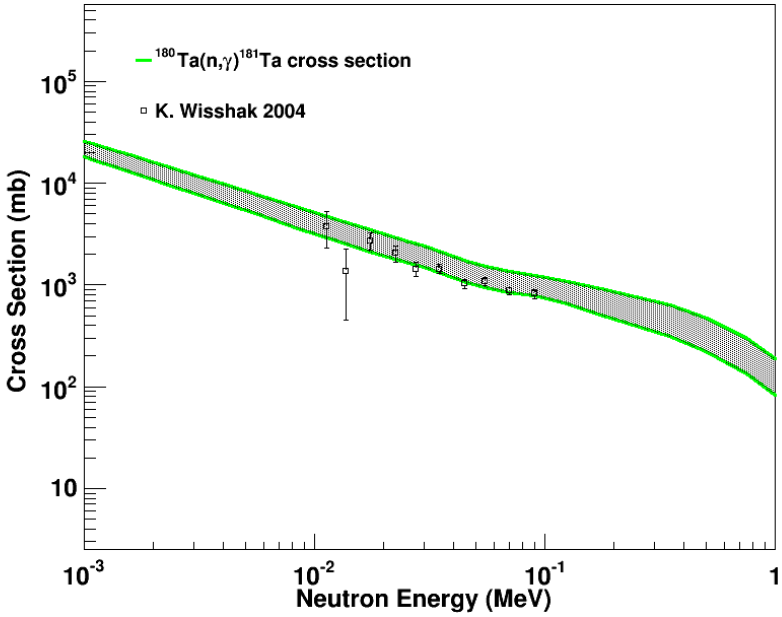

Figure 6.26: ^{181}Ta cross sections. The green band represents the cross sections calculated from the NLD and PSF. The open squares are experimentally measured cross sections from reference [94].

Chapter 7

Discussion

The scissors resonance was first observed in an inelastic electron scattering experiment of ^{156}Gd [5]. The scissors resonance has also been observed in various other well deformed nuclei using nuclear resonance fluorescence (NRF) experiments [6] and through the Oslo method (e.g. nuclei in the actinide [7] and rare earth regions [95]). Generally it is accepted that the total scissors resonance strength is proportional to the square of the deformation parameter: $\sum B(M_1) \approx \delta^2$ [96].

The investigation for the scissors resonance was extended to less deformed nuclei, for example γ-soft, vibrational and transitional nuclei. The scissors resonance was found to be reduced by 25% in γ-soft nuclei compared to other good rotors [36]. Initially, scissors resonance experiments dealt only with even-even nuclei, since it was thought that in odd-even nuclei the scissors resonance strength would be more fragmented. The fragmentation is due the unpaired particle inducing a large fragmentation in the M1 strength distribution [8]. However in figure 7.1 contradictory M1 strength distributions are shown. Note in figure 7.1 the quantity $g\Gamma_0^{red}$ represents the reduced excitation probabilities $B(E1)\uparrow$ or $B(M1)\uparrow$ used to compare dipole strengths. It is the product of the reduced transition probability Γ_0^{red} and the spin factor g.

Some odd-even nuclei, ^{155}Gd, ^{157}Gd, ^{165}Ho, ^{167}Er and ^{169}Tm are characterized by large fragmented M1 strength distributions which may be attributed to the unpaired nucleon. It should be noted that the even-even Gd isotopes have a localized M1 strength as expected. Other odd-even nuclei, ^{161}Dy, ^{159}Tb and ^{163}Dy, however, also show localized M1 strength distributions. Comparing the even-odd summed M1 strengths to even-even M1 strengths in the same mass region, it was concluded that the summed strength is reduced (see bottom part of figure 7.1) [8].

Recently, data from Oslo have shown that the scissors resonance is strongly observable in the actinide region. Unlike in the rare-earth region, the scissors

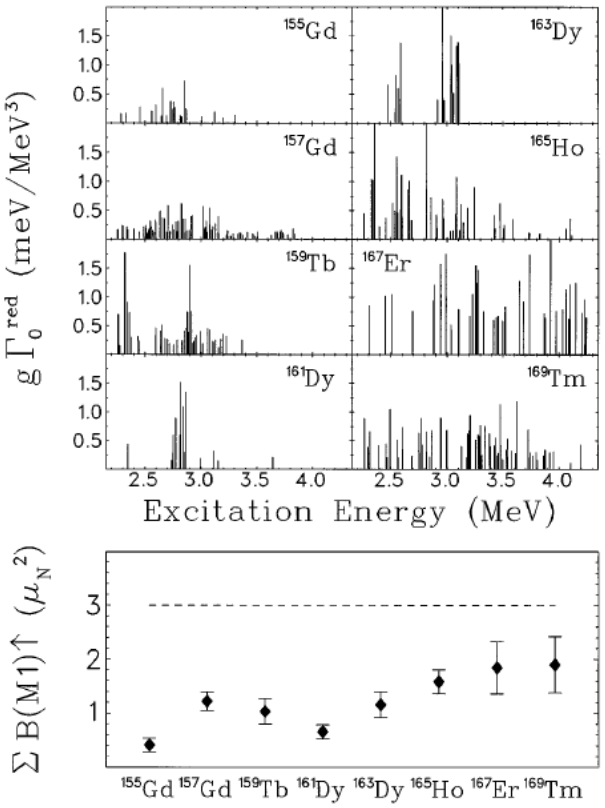

Figure 7.1: Top: Comparing the M1 strength distributions between various even-odd nuclei. Bottom: The dashed line shows the typical average $B(M1)\uparrow$ value for even-mass. The points are the typical average $B(M1)\uparrow$ value for odd-mass nuclei [8].

resonance is not fragmented for odd-odd [34], even-odd [7] or even-even [7] nuclei in the actinide region, but are consistently localized, although some exhibit an unexplained double-humped structure, see figure 7.2 [7].

In reference [97] the unfolded capture γ-ray spectra of various odd-even nuclei are compared, this is shown in figure 7.3. A bump in this spectrum, presumably the scissors resonance, can be seen between energies 1-3 MeV for Pr, Tb, Ho and Lu, but no resonances can be seen in Ta or Au in this energy region. This has recently been confirmed for ^{197,198}Au [67], where no clear scissors resonance is observed. The PSF of ^{197,198}Au is shown in figure 7.4.

In reference [41] the low-lying excitation of ^{181}Ta was investigated using NRF experiments. It was found that the scissors resonance was rather weak and fragmented. The total strength in the energy range $E_x = 1.8 - 4$ MeV of ^{181}Ta is reduced by a factor 3.5 compared to the scissors resonance strength of ^{180}Hf. The M1 strength distribution of ^{180}Hf is surprisingly also fragmented for this even-even nucleus. The low-lying excitations of ^{181}Ta and ^{180}Hf are shown in

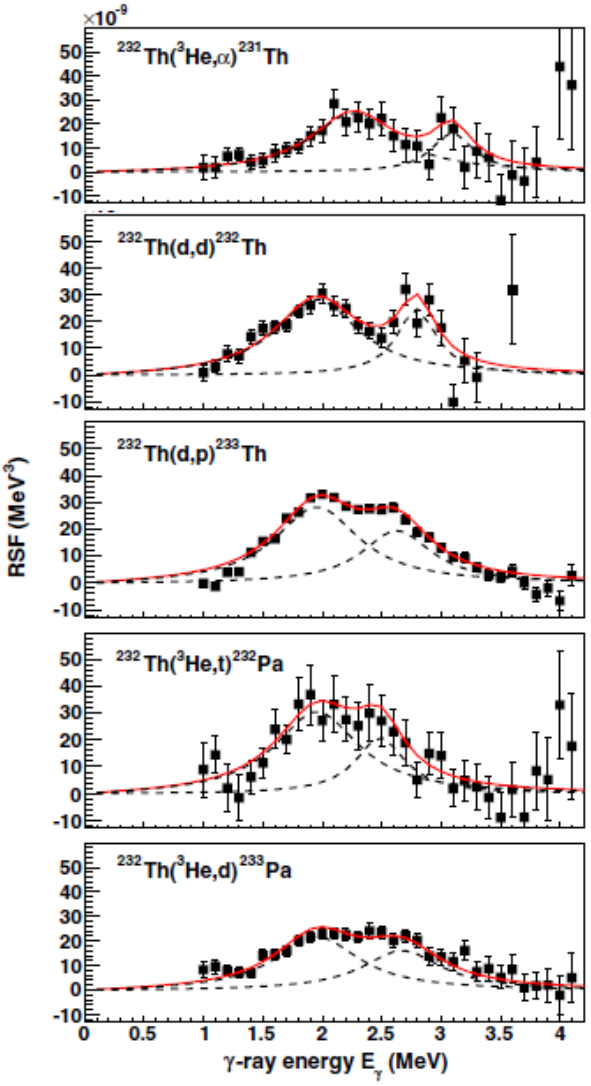

Figure 7.2: The scissors resonance for ^{231}Th, ^{232}Th, ^{232}Th, ^{232}Pa and ^{233}Pa [7]. In all actinide nuclei the scissors resonance exhibits an unexpected double humped structure that is yet to be understood.

figure 7.5.

In reference [9] it is concluded that fragmentation of the scissors resonance is not yet understood. Only 33-50% M1 strength for the odd-mass nuclei could be detected in the energy range 2.5-3.7 MeV in some experiments, due to large fragmentation. Figure 7.6 shows ground state width decays for ^{163}Dy from two experiments. The sensitivity of the latest experiment was greatly improved and a large number of previously undetectable transitions were found. The M1 strength of the latest experiment compares better to close lying even-mass M1 strength and accounts for the lost M1 strength in odd-mass nuclei.

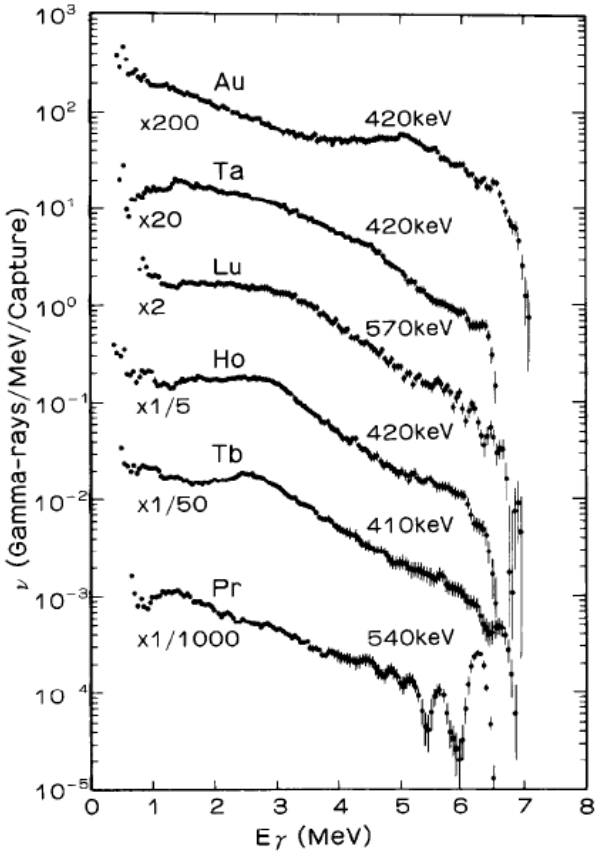

Figure 7.3: The unfolded capture γ-ray spectra various odd-even nuclei: Pr, Tb, Ho, Lu, Ta and Au are compared. Scissor resonances can be seen as small bumps in all nuclei except Ta and Au [97].

From axially symmetric HFB calculations using the Cogny effective nucleon-nucleon interaction the axial deformation parameter β_2 is calculated to be ≈ 0.27 for ^{182}Ta and ≈ 0.28 for ^{181}Ta [10]. The HFB calculations of the deformation parameter for ^{182}Ta is shown in figure 7.7. This is consistent with the measurement of a positive quadrupole deformation of $Q = +2.6(3)$ eb for ^{182}Ta [83]. According to equation 2.18 this gives a δ parameter of ≈ 0.255 for ^{182}Ta and ≈ 0.265 for ^{181}Ta.

According to equation 2.28 the spin-flip resonance should be around $E_x = 7.2$ MeV for both ^{181}Ta and ^{182}Ta, the energy region overlapping with the pygmy resonance. According to equation 2.17 the scissors resonance centroid should be at $E_x = 2.98$ MeV for ^{182}Ta and at $E_x = 3.1$ MeV for ^{181}Ta. The results of this work (figure 6.12) is quite similar to the results of [67], where no significant scissors resonance can be observed. Tantalum-182 is in the transitional region, from prolate to oblate shapes, see figure 1.3. Tantalum-182 also has

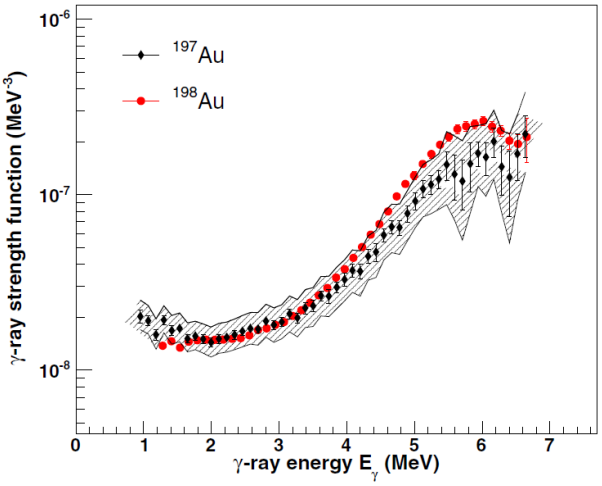

Figure 7.4: The PSF of ^{197}Au and ^{198}Au are shown with the ^{197}Au error band [67].

2 odd particles giving the M1 strength the possibility to couple to both an unpaired proton and neutron spreading the strength apart. This combination may induce a very large fragmentation making the resonance un-observable with the current experimental detection threshold.

Comparing the PSF of ^{181}Ta (figure 6.13) to the M1 strength distribution of [41] a weak scissors resonance may be observable at energies $E_x = 2.5 - 3.5$ MeV. With only 1 odd particle the fragmentation may not be as large as in ^{182}Ta, unfortunately the analyzed data set has relatively large uncertainties and does not extend above $E_x = 4$ MeV. Another ^{181}Ta(d,d')^{181}Ta data set is available with a beam energy of 15 MeV instead of the current 12.5 MeV. This will increase the excitation energy from ≈ 4 MeV to ≈ 6.5 MeV. This data set also has ≈ 3 times more data, reducing the uncertainties. Once this data set has been analyzed, which is beyond the scope of this thesis, a better understanding of a possible scissors resonance in ^{181}Ta will be obtained.

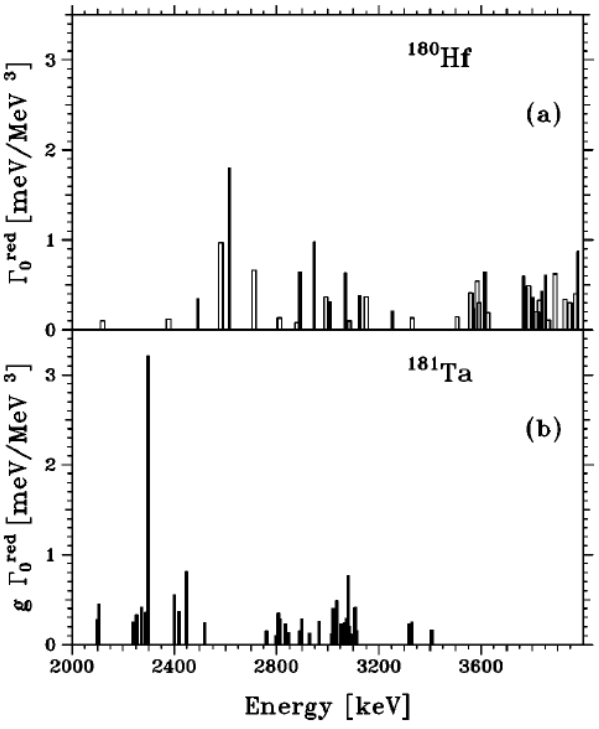

Figure 7.5: Dipole strength comparison between odd-even ^{181}Ta and even-even ^{180}Hf [41].

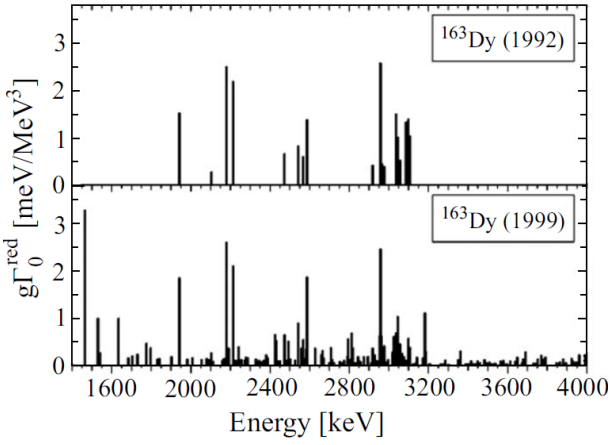

Figure 7.6: M1 strength distributions from two experiments of ^{163}Dy from [98] and [99]. The transitions of both experiments agree, however the second experiment, with better sensitivity, shows previously undetected weak transitions.

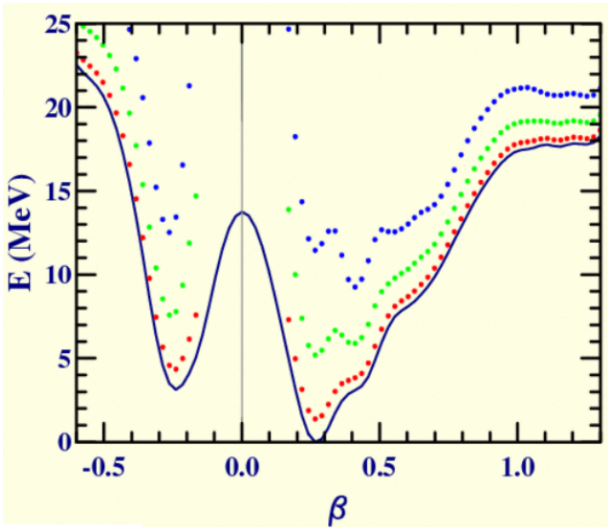

Figure 7.7: HFB calculations of ^{182}Ta from the online database of [10].

Chapter 8

Conclusion

From the ^{181}Ta(d,p)^{182}Ta and ^{181}Ta(d,d')^{181}Ta reactions the PSF and NLD of ^{182}Ta and ^{181}Ta were extracted using the Oslo method. The PSF and NLD were also used to calculate ^{180}Ta(n,γ) and ^{181}Ta(n,γ) cross sections using the Talys reaction code.

No identifiable scissors resonance is observed for ^{182}Ta, in fact, overall the PSF appears quite featureless. A weak scissors resonance may be present for ^{181}Ta at energies $E_x = 2.5 - 3.5$ MeV. This resonance weakness could be due to the fact that Tantalum is in the transitional region, despite being well deformed, from prolate to oblate shapes. The unpaired nucleons, two for ^{182}Ta and one for ^{181}Ta, give the M1 strength the possibility to couple to one or two unpaired nucleons, respectively spreading the strength further apart. Having unpaired nucleons as well as being in a transitional region may induce a very large fragmentation making the resonance un-observable with the current experimental detection threshold of the Oslo method.

The disappearance of the scissors resonance in Ta isotopes requires the investigation of other nuclei in this region, specifically nuclei that are γ-soft and odd-odd in nature. Work has to be done to identify the extent and persistence of the scissors resonance in order to understand the evolution of this resonance which can have a significant impact on astrophysical reaction rates. The Oslo group will soon be performing experiments on isotopes of W and Os, nuclei in the same mass region as Ta, that will further our knowledge of the scissors resonance and its evolution.

Appendices

Appendix A

Tables

Table A.1: The data points of the NLD of ^{182}Ta.

E_x (MeV)	NLD (MeV^{-1})	δNLD (MeV^{-1})
-0.196	1.908	0.613
-0.068	20.190	1.139
0.060	39.650	2.035
0.188	52.215	2.461
0.316	63.032	2.450
0.444	75.278	2.970
0.572	95.545	3.628
0.700	117.842	3.860
0.828	143.209	4.405
0.956	179.177	5.266
1.084	231.394	7.159
1.212	314.064	8.309
1.340	417.082	10.436
1.468	565.510	10.441
1.596	756.483	14.565
1.724	987.341	19.609
1.852	1303.8	21.936
1.980	1635.7	34.766
2.108	2048.6	37.767
2.236	2517.3	54.491
2.364	3089.5	74.359
2.492	3874.4	117.99
2.620	4944.1	140.99
2.748	6250.3	189.96
2.876	7710.6	283.01
3.004	9630.2	372.71
3.132	11783.3	462.78
3.260	14757	674.23
3.388	18101	939.55
3.516	22210	1079
3.644	27850	1535.1
3.772	33370	1884.3
3.900	41370	2532.9
4.028	50480	3253.9
4.156	60450	4262.5
4.284	74960	6291.7
4.412	85140	7619.2
4.540	108400	11141
4.668	151400	15618
4.796	192000	22152
4.924	243500	46162

Table A.2: The data points of the NLD of ^{181}Ta.

E_x (MeV)	NLD (MeV^{-1})	δNLD (MeV^{-1})
-0.235	0.431	0.244
-0.118	3.121	0.450
-0.001	14.569	0.578
0.116	19.059	0.855
0.233	20.511	0.908
0.350	21.724	1.185
0.467	22.375	1.571
0.584	22.779	1.735
0.701	22.267	1.675
0.818	22.232	2.389
0.935	30.358	2.678
1.052	52.801	4.001
1.169	70.943	5.571
1.286	112.21	6.640
1.403	151.02	9.987
1.520	187.14	10.933
1.637	231.08	15.132
1.754	291.12	19.938
1.871	396.00	30.784
1.988	578.92	44.682
2.105	717.43	69.412
2.222	659.01	83.956
2.339	768.81	119.69
2.456	916.40	157.38
2.573	1205.1	283.31
2.690	1390.0	402.76
2.807	1920.5	620.99
2.924	2631.5	1005.3
3.041	2301.3	1547.9

Table A.3: The data points of the PSF of ^{182}Ta. Upper and lower bound represents the difference between the PSF and upper and lower bound.

E_γ (MeV)	PSF (10^{-8} MeV^{-3})	δPSF (10^{-8} MeV^{-3})	upper bound (10^{-8} MeV^{-3})	lower bound (10^{-8} MeV^{-3})
0.956	1.127	0.036	0.0933	-0.089
1.084	1.453	0.036	0.112	-0.107
1.212	1.511	0.033	0.116	-0.111
1.340	1.503	0.035	0.122	-0.116
1.468	1.274	0.039	0.111	-0.105
1.596	1.722	0.048	0.157	-0.147
1.724	1.844	0.051	0.172	-0.161
1.852	2.016	0.057	0.194	-0.181
1.980	2.066	0.057	0.203	-0.189
2.108	2.065	0.070	0.222	-0.205
2.236	2.238	0.076	0.247	-0.228
2.364	2.399	0.079	0.268	-0.246
2.492	2.566	0.098	0.308	-0.282
2.620	2.805	0.122	0.36	-0.327
2.748	3.040	0.130	0.396	-0.359
2.876	3.256	0.152	0.447	-0.403
3.004	3.404	0.168	0.487	-0.437
3.132	3.604	0.197	0.546	-0.487
3.260	3.899	0.207	0.594	-0.529
3.388	4.225	0.244	0.677	-0.6
3.516	4.664	0.285	0.777	-0.686
3.644	5.120	0.355	0.915	- 0.802
3.772	5.552	0.381	1	-0.877
3.900	6.192	0.431	1.14	-0.996
4.028	6.768	0.492	1.29	-1.12
4.156	7.307	0.538	1.42	-1.23
4.284	7.922	0.665	1.65	-1.42
4.412	8.635	0.702	1.8	-1.55
4.520	9.050	0.800	1.99	-1.69
4.668	9.519	0.900	2.18	-1.85
4.796	9.806	0.921	2.27	-1.92
4.924	9.998	0.875	2.7	-1.92
5.052	11.149	1.101	2.71	-1.92
5.180	11.723	1.156	2.88	-2.41
5.308	12.350	1.451	3.33	-2.77
5.436	13.381	1.577	3.66	-3.027
5.564	12.814	1.501	3.53	-2.91
5.692	15.285	1.918	4.4	-3.61
5.820	18.232	2.614	5.68	-4.63

Table A.4: The data points of the PSF of ^{181}Ta. Upper and lower bound represents the difference between the PSF and upper and lower bound.

E_γ (MeV)	PSF (10^{-8} MeV^{-3})	δPSF (10^{-8} MeV^{-3})	upper bound (10^{-8} MeV^{-3})	lower bound (10^{-8} MeV^{-3})
0.935	2.228	0.254	-0.564	0.539
1.052	2.294	0.198	-0.504	0.454
1.169	1.728	0.167	-0.377	0.339
1.286	1.252	0.165	-0.298	0.276
1.403	1.057	0.115	-0.219	0.192
1.520	1.895	0.149	-0.322	0.26
1.637	2.556	0.161	-0.369	0.279
1.754	2.689	0.176	-0.363	0.266
1.871	2.024	0.151	-0.268	0.195
1.988	2.168	0.166	-0.265	0.187
2.105	2.444	0.159	-0.243	0.153
2.222	2.650	0.199	-0.258	0.162
2.339	2.866	0.213	-0.179	0.277
2.456	3.221	0.228	0.236	-0.322
2.573	3.147	0.243	0.296	-0.375
2.690	2.962	0.248	0.342	-0.4
2.807	3.321	0.265	0.42	-0.468
2.924	3.787	0.324	0.559	-0.589
3.041	4.025	0.353	0.665	-0.672
3.158	4.575	0.401	0.828	-0.806
3.275	3.886	0.456	0.892	-0.822
3.392	4.227	0.526	1.072	-0.958
3.509	4.600	0.531	1.198	-1.045
3.626	5.449	0.693	1.586	-1.34
3.743	6.021	0.949	2.07	-1.689
3.860	6.874	1.427	2.89	-2.27
3.977	8.163	2.442	4.479	-3.382

Table A.5: The resonance parameters used in the Lorentzian functions for ^{182}Ta for the Talys cross section calculations. The GEDR parameters are modified from [66] and σ is modified from [15].

Upper error band	E_0(MeV)	σ(mb)	Γ_0(MeV)
Res1	4.6	1.9	1.8
Res2	6.98	46	1.33
GEDR1	12.66	345	2.62
GEDR2	15.65	323	3.4
Lower error band	E_0(MeV)	σ(mb)	Γ_0(MeV)
Res1	4.6	1.4	1.8
Res2	7.05	35	1.33
GEDR1	12.66	345	2.62
GEDR2	15.65	323	3.4

Table A.6: The resonance parameters used in the Lorentzian functions for ^{181}Ta for the Talys cross section calculations. The GEDR parameters are modified from [66] and σ is modified from [15].

Upper error band	E_0(MeV)	σ(mb)	Γ_0(MeV)
Res1	4.6	1.75	1.95
Res2	6.85	47.7	1.73
GEDR1	12.66	345	2.62
GEDR2	15.65	323	3.4
Lower error band	E_0(MeV)	σ(mb)	Γ_0(MeV)
Res1	4.6	0.95	1.95
Res2	6.95	39.5	1.73
GEDR1	12.66	345	2.62
GEDR2	15.65	323	3.4

Bibliography

[1] A. J. Koning *et al.* Nuclear data for science and technology. *EDP sciences; eds O. Bersillon et. al.*, page 211, 2008. see also www.talys.eu.

[2] M. B. Chadwick *et al. Nucl. Data Sheets*, 112:2887, 2011.

[3] M. Thoenessen from S. Goriely. *Phys. Lett. B*, 436:10–18, September 1998.

[4] A. Schiller *et al. Nucl. Instrum. Methods Phys. Res. A*, 447:498, 2000.

[5] D. Bohle *et al. Phys. Lett. B*, 137:27, 1984.

[6] U. Kneissl, H. H. Pitz, and A. Zilges. *Prog. Part. Nucl. Phys.*, 37:349–433, 1996.

[7] M. Guttormsen *et al. Phys. Rev. Lett.*, 109(162503), 2012.

[8] J. Ender *et al. Phys. Rev. Lett.*, 79:2010, 1997.

[9] P. von Neumann-Cosel, K. Heyde, and A. Richter. *Rev. Mod. Phys.*, 82:2365, 2010.

[10] S. Hilaire and M. Girod. The amedee nuclear structure database. *International conference on Nuclear Data for Science and Technology 2007*, page 107, 2007.

[11] M. Guttormsen *et al. Eur. Phys. J.*, A51:12, 2015.

[12] R. Chankova *et al. Phys. Rev. C*, 73:034311, 2006.

[13] H. Bethe. *Phys. Rev.*, 50:332–341, 1936.

[14] A. Gilbert and A.G.W. Cameron. *Can. J. of Phys.*, 43:1446, 1965.

[15] T. von Egidy and D. Bucurescu. *Phys. Rev. C*, 80, 2009.

[16] G. A. Bartholomew *et al. Advances in Nuclear Physics*, pages 229–324, 1973.

[17] Bakken. Wikipedia, 2016.

[18] K. S. Krane. *Introductory Nuclear Physics.* John Wiley and Sons Inc, 1988.

[19] A. Richter. *Elementary Isovector span and orbital magnetic dipole modes reviseted in the shell model.* World Scmntlfic, Singapore, 1989. in Shell model and nuclear structure' where do we stand?

[20] Giant nuclear resonances. http://encyclopedia2.thefreedictionary.com, 2002.

[21] B.V. Kheswa. *Impact of the ^{138,139}La Radiative Strength Functions and Nuclear Level Densities on the Galactic Production of ^{138}La.* PhD thesis, University of Stellenbosch, 2015.

[22] E. Litvinova P. Ring and D. Vretenar. *Phys. Lett. B*, 647:111, 2007.

[23] P. F. Bortignon, D. Sarchi, and G. Colo. *Phys. Lett.*, B601:27, 2004.

[24] A. V. Voinov *et al. Physics of atomic nuclei*, 67:1866–1872, 2005.

[25] Z. W. Bell, L. S. Cardman, and P. Axel. *Phys. Rev. C*, 25:791, 1982.

[26] A. V. Avdeenkov and S. P. Kamerdzhiev. *Physics of atomic nuclei*, 72:1332–1339, 2009.

[27] A. Arima and F. Iachello. *Phys. Lett. B*, 57:39, 1975.

[28] A. Arima and F. Iachello. *Phys. Rev. Lett.*, 35:1069, 1975.

[29] A. Richter. *Nucl. Phys. A*, 507:99c–128c, 1990.

[30] N. Lo Iudice and F. Palumbo. *Phys. Rev. Lett.*, 41:1532, 1978.

[31] F. Iachello. *Nucl. Phys. A*, 358:89–112, 1981.

[32] A. Richter. *Prog. Part. Nucl. Phys.*, 34:261, 1995.

[33] R.B. Firestone and V.S. Shirley. *Table of Isotopes 8th ed.* John Wiley and sons, 8th ed edition, 1996.

[34] T. G. Tornyi *et al. Phys. Rev. C*, 89:044323, 2014.

[35] M. Guttormsen *et al. Phys. Rev. C*, 89:014302, 2014.

[36] P. von Brentano *et al. Phys. Rev. Let.*, 76:2029, 1996.

[37] H. Maser *et al. Phys. Rev. C*, 54:R2129, 1996.

[38] C. Fransen *et al. Phys. Rev. C*, 59:2264, 1999.

[39] C. Fransen *et al. Phys. Lett. B*, 351:82, 1995.

[40] R. Schwengner *et al. Nucl. Phys. A*, 620:277, 1997.

[41] A. Wolpert *et al. Phys. Rev. C*, 58:765, 1998.

[42] C. De Coster and K. Heyde. *Phys. Rev. Lett.*, 66:2456, 1991.

[43] R. R. Hilton, W. Höhenberger, and P. Ring. *Eur. Phys. J. A*, 1:257, 1998.

[44] P. Sarriguren *et al. J. Phys. G*, 19:291, 1993.

[45] A. Richter. *Proceeding of the 4th International Spring Seminar on Nuclear Physics: The building blocks of Nuclear Structure, edited by A. Covello*, page 335, 1994.

[46] D. Frekers *et al. Phys. Lett. B*, 244:178, 1990.

[47] D. Zawischa and J. Speth. *Nucl. Phys. A*, 569:343, 1994.

[48] C. Coster *et al. Nucl. Phys. A*, 542:375, 1992.

[49] J. Kopecky and M. Uhl. *Phys. Rev. C*, 41:1941, 1990.

[50] J. Kopecky *et al. Phys. Rev. C*, 47:312, 1993.

[51] W. R. Hix *et al. J. Phys. G*, 29:2523, 2003.

[52] K. G. Langanke *et al. Phys. Rev. Lett.*, 93:202501, 2004.

[53] A. C. Larsen *et al. Phys. Rev. C*, 83:034315, November 2011.

[54] N. Starfelt and H. W. Koch. *Phys. Rev.*, 1956.

[55] P. C. Fisher and L. B. Engle. *Phys. Rev.*, 134:B796, 1964.

[56] W. Trautmann *et al. Nucl. Phys.*, A 378:141–158, 1982.

[57] R. Koohi-Fayegh *et al. Nucl. Instrum. Methods*, A 329:269–276, 1993.

[58] D. Sam *et al. Nucl. Instrum. Methods*, 64:148–156, 1968.

[59] M. Guttormsen. *Nucl. Instrum. Methods*, 374:371–376, January 1996.

[60] J. Rekstad *et al. Phys. Scr.*, 34:644–650, 1986.

[61] A. C. Larsen. *Statistical properties in the quasi-continuum of atomic nuclei.* PhD thesis, University of Oslo, May 2008. PhD Thesis.

[62] M. Guttormsen *et al. Nucl. Instrum. Methods Phys. Res.*, A 255:518–523, 1987.

[63] J. Rekstad *et al. Phys. Scr.*, T5:45–50, 1983.

[64] E. Fermi. *Nucl. Phys.* University of Chicago Press, 1950.

[65] D. M. Brink. PhD thesis, Oxford University, 1955. PhD Thesis.

[66] R. Capote *et al.* Reference input parameter library, ripl-2 and ripl-3.

[67] F. Giacoppo *et al. Phys. Rev. C*, 91:054327, 2015.

[68] M. Guttormsen *et al. Phys. Rev. C*, 71, 2005.

[69] M. Guttormsen *et al. Phys. Rev. C*, 68, 2003.

[70] U. Agvaanluvsan *et al. Phys. Rev. C*, 70, 2004.

[71] E. Betak. Proceedings of the second international workshop on compound nuclear reactions and related topics. *EPJ Web of Conferences 2*, 2010.

[72] F. Bečvář. *Nucl. Instrum. Methods Phys. Res. A*, 417:434, 1998.

[73] U. Agvaanluvsan *et al. Phys. Rev. Lett.*, 102, 2009.

[74] A. Voinov *et al. Phys. Rev. Lett.*, 93, 2004.

[75] A. C. Larsen *et al. Phys. Rev. C*, C 76, 2007.

[76] T. von Egidy *et al. Phys. Rev. C*, 73, 1988.

[77] Managing editor DoP. Uio department of physics, 2011.

[78] M. Guttormsen *et al. Nucl. Instrum. Methods Phys. Res. A*, page 168, 2011.

[79] M. Guttormsen. *Nucl. Instrum. Methods Phys. Res. A*, 648:168–173, 2011.

[80] M. Guttormsen *et al. Phys. Scr.*, T32:54, 1990.

[81] Siri kinematic calculator, 2015. https://unarydigits.com/jkinz.

[82] W. R. Leo *et al. Techniques for Nuclear and Particle Physics Experiments.* Springer-Verlag, 5 edition, 1994.

[83] Brookhaven National Laboratory. A database of nuclear levels. http://www.nndc.bnl.gov/chart, retrieved 2015.

[84] J. R. Erskine and W. W. Buechner. *Phys. Rev.*, 133:B370, 1964.

[85] S. F. Mughabghab. *Atlas of Neutron Resonance.* Elsevier Science, Amsterdam, 5th ed edition, 2006.

[86] L. G. Moretto *et al. Journal of Physics: Conference Series*, 580:012048, 2015.

[87] K. L. Malatji. Nuclear level density and gamma-ray strength functions in ta isotopes and nucleo-synthesis of ^{180}ta. Master's thesis, University of the Western Cape, 2016.

[88] J. Miller, C. Schuhl, and C. Tzara. *Nucl. Phys.*, 32:236, 1962.

[89] S. N. Belyaev and V. P. Sinichkin. *Workshop on beam dynamics and optimization, Saratov*, page 81, 2001.

[90] H. Beil, R. Bergere, and A. Veyssiere. *Nucl. Phys.*, 121:463, 1968.

[91] A. Makinaga *et al. Phys. Rev. C*, 90:044301, 2014.

[92] M. Lindner *et al. Nuclear Science and Engineering*, 59:381, 1976.

[93] V. N. Kononov *et al. Yadernaya Fizika*, 26:947, 1977.

[94] K. Wisshak *et al. Phys. Rev. C*, 69:055801, 2004.

[95] S. Siem *et al. Phys. Rev. C*, 65:044318, 2002.

[96] W. Ziegler *et al. Phys. Rev. Lett.*, 65:2515, 1990.

[97] M. Igashira *et al. Nucl. Phys. A*, 457:301–316, 1986.

[98] I. Bauske *et al. Phys. Rev. Lett*, 71:975, 1993.

[99] A. Nord *et al. Phys. Rev. C*, 67:034307, 2003.